Spatio-temporal variations of observed and modelled stratospheric trace gases

Dissertation
zur Erlangung des Grades Dr. rer. nat.
am Fachbereich Physik der Universität Bremen

vorgelegt von

M.Sc. Meteo. Evgenia Galytska
Institut für Umweltphysik,
Fachbereich 1, Physik und Elektrotechnik,
Universität Bremen

1. Gutachter	:	Prof. Dr. John P. Burrows
2. Gutachter	:	Prof. Dr. Martyn P. Chipperfield

Tag des Promotionskolloquiums	:	23.07.2019

Abstract

The satellite instrument SCanning Imaging Absorption spectroMeter for Atmospheric CHartographY (SCIAMACHY) was operational for almost 10 years during the period 2002-2012 aboard the Environmental Satellite (Envisat) of the European Space Agency (ESA), measuring a number of important atmospheric trace gases in three different modes. SCIAMACHY measured the spectra of the solar light scattered by the atmosphere (or transmitted through the atmosphere in the occultation mode). These spectra were used to retrieve vertical profiles or total columns of the atmospheric trace gases as well as aerosol and cloud parameters.

The purpose of this study was to investigate the spatio-temporal changes of stratospheric species such as ozone (O_3) and nitrogen dioxide (NO_2) and reveal possible drivers of the observed variations. Taking into account the importance of understanding the changes in the atmospheric composition it was crucial to 1) find an atmospheric model, which adequately describes chemical-dynamical processes in the stratosphere and 2) have an accurate knowledge of trace gases distribution.

At the beginning the SCIAMACHY measurements were compared with data from the Bremen 3-D chemistry-transport model (B3DCTM) and the TOMCAT model. Both models are of identical origin, but result from different development branches. During the investigations the performance of models was assessed; however, only TOMCAT was involved in the further study, because it was found to agree with the SCIAMACHY measurements better.

In order to achieve sufficiently accurate knowledge of trace gases distribution in the stratosphere, the measurements need to be validated by comparing them with data from independent satellite instruments. As NO_2 is a very important parameter in the loss of O_3, the data quality of both should be checked. While global SCIAMACHY limb O_3 profiles had been previously validated, in this thesis the newest

SCIAMACHY NO_2 V4.0 scientific profiles were compared with co-located observations from limb and occultation sounders, namely the Michelson Interferometer for Passive Atmospheric Sounding (MIPAS) and the Stratospheric Aerosol and Gas Experiment (SAGE) II. To account for the pronounced diurnal variations of NO_2, a model-based photochemical correction was applied. To achieve this correction, co-located satellite profiles were scaled to the illumination conditions of SCIAMACHY limb measurements by applying the TOMCAT 3-D and 1-D (column) models.

Based on reliable model results and validated satellite measurements, the analysis of O_3 and NO_2 changes was performed. While recent studies have reported the beginning of a recovery in upper stratospheric O_3 at middle and high latitudes, an unexpected O_3 decline was observed during the first decade of the 21^{st} century in the tropical region of the middle stratosphere at around 30-35 km altitude. SCIAMACHY measurements indicated significant O_3 decline of around 12% per decade during the period 2004-2012, associated with an increase in NO_2 of around 16% per decade. To explain these observed changes, the TOMCAT model simulations with different chemical and dynamical forcings were used. The TOMCAT simulations reproduce the SCIAMACHY-observed O_3 decrease and NO_2 increase in the tropical middle stratosphere. The simulations suggest that the increase in NO_2 (around 7% per decade) is due to similar increase in reactive odd nitrogen (NO_y). The latter increases as a result of a longer residence time of the source gas nitrous oxide (N_2O). The simulated decline of N_2O (around 10% per decade) most likely occurs as a result of variations in the deep branch of the Brewer-Dobson Circulation (BDC).

This thesis performs a detailed investigation of the chemical-dynamical interactions among the Age of Air (AoA) as the metric of BDC, N_2O, NO_2, and O_3 in the tropical middle stratosphere. The analysis of model results show significant seasonal changes in AoA. During the autumn months there are positive AoA changes, that imply slower transport and longer residence time of N_2O allowing larger formation of NO_y which destroys O_3. During winter months there are negative AoA changes, that imply faster N_2O transport and less NO_y production. Although, the AoA variations over a year show a statistically insignificant linear change, non-linearities in the chemistry-transport interactions mean that the net negative N_2O change remains.

Publications and Contributions

Parts of this thesis are based on cited peer-reviewed publications, reports, conference talks, and poster contributions.

Peer-reviewed Publications

Galytska, E., Rozanov, A., Chipperfield, M. P., Hommel, R., and Burrows, J. P.: Validation of SCIAMACHY NO_2 V4.0: accounting for differences in local solar time, in preparation for publication in Atmos. Meas. Tech., 2019.

Galytska, E., Rozanov, A., Chipperfield, M. P., Dhomse, S. S., Weber, M., Arosio, C., Feng, W., and Burrows, J. P.: Dynamically controlled ozone decline in the tropical mid-stratosphere observed by SCIAMACHY, Atmos. Chem. Phys., 19, 767-783, https://doi.org/10.5194/acp-19-767-2019, 2019.

Galytska, E., Danylevsky, V., Hommel, R., and Burrows, J. P.: Increased aerosol content in the atmosphere over Ukraine during summer 2010, Atmos. Meas. Tech., 11, 2101-2118, https://doi.org/10.5194/amt-11-2101-2018, 2018.

Oral Contributions to National and International Conferences

Galytska, E., Rozanov A., Chipperfield M. P., Arosio C., Dhomse S. S., and Burrows J. P.: Ozone decline in the tropical mid-stratosphere observed by SCIAMACHY and its relation to the stratospheric dynamics. IUP/AWI Block Seminar, 04.02.2019, Bremen, Germany. http://carppond.iup.uni-bremen.de:8000/d/ba43c0340a2b4ada8f7e/files/?p=/Galytska_block_190204.pdf

Galytska, E., Rozanov A., Chipperfield M. P., Arosio C., Dhomse S. S., and Burrows J. P.: Ozone decline in the tropical mid-stratosphere observed by SCIAMACHY and its relation to the stratospheric dynamics. ATMOS-2018, 26-29.11.2018, Salzburg, Austria. http://atmos2018.esa.int/files/5_150_Galytska_ATMOS_2018.pdf

Galytska, E., Hommel, R., Burrows, J. P.: 3-D model studies of the transport and chemistry of the stratosphere. Astronomy and Space Physics Conference, 24-

27.05.2016, Kyiv, Ukraine. http://www.observ.univ.kiev.ua/obs/conference-2016/?lang=en

Poster Contributions to National and International Conferences

Galytska, E., Chipperfield, M. P., Rozanov, A., Dhomse, S. S., Burrows, J. P., and Stiller, G.: Understanding decadal NO_2 and O_3 changes in the tropical stratosphere by means of chemistry-transport models. Annual Science Meeting of Institute for Climate and Atmospheric Science, 2.11.2017, Leeds, UK.

Galytska, E., Chipperfield, M. P., Rozanov, A., Dhomse, S. S., Hommel, R., Burrows J. P., Weigel, K., Aschmann, J., Stiller, G., and Zawodny, J. M.: Variability of stratospheric NO_2: CTM evaluation using SCIAMACHY measurements and its further application for photochemical conversion. Chemistry-Climate Model Initiative Science Workshop, 13-15.06.2017, Toulouse, France. http://www.meteo.fr/cic/meetings/2017/CCMI/

Galytska, E., Hommel, R., Rozanov, A., McLinden, C., Lloyd, N., Stiller, G., Degenstein, D., Zawodny J., Burrows, J.P.: Validation of SCIAMACHY limb NO_2 profiles: accounting for differences in the local solar time. ACVE 2016 - Atmospheric Composition Validation and Evolution Workshop, 18-20.10.2016, Frascati, Italy. http://old.esaconferencebureau.com/2016-events/16c16-acve/abstract-book

Galytska, E., Hommel, R., Burrows, J. P.: Mean age of stratospheric air in the Bremen CTM during 1986-2011. DPG 80. Jahrestagung der DPG und DPG-Fruhjahrstagung, 6-11.03.2016, Regensburg, Germany.

Galytska, E., Hommel, R., Guenther, A., Sinnhuber, B.-M., Burrows, J. P.: Reinvestigation of the stratospheric age of air in the Bremen CTM. SPARC workshop SHARP-2016, 16-19.02.2016, Berlin, Germany. http://www.geo.fu-berlin.de/en/met/sharp/SPARC-workshop-on-_SHARP_2016/Poster.html

Galytska, E., Danylevsky, V., Snizhko, S.: Analysis of aerosol optical properties in the atmosphere over Ukraine based on ground (AERONET) and satellite (MODIS, CALIOP) observational data. 8^{th} Atmospheric Limb Workshop, 15-17.09.2015, Gothenburg, Sweden. https://www.chalmers.se/en/conference/limb-workshop-2015/Pages/Programme.aspx

PICO (Presenting Interactive COntent)

Galytska, E., Arosio C., Rozanov A., Chipperfield M. P., Dhomse S. S., Sofieva V., and Burrows, J. P.: Seasonal variability in transport in the tropical mid-stratosphere and its impact on ozone and key trace gases. European Geosciences Union General Assembly 2019, 7-12.04.2019, Vienna, Austria. https://meetingorganizer.copernicus.org/EGU2019/EGU2019-8060.pdf

Galytska, E., Chipperfield, M. P., Rozanov, A., Dhomse, S. S., and Burrows, J. P.: Understanding NO_2 and O_3 changes in tropical mid-stratosphere by means of a chemistry-transport model. European Geosciences Union General Assembly 2018, 8-13.04.2018, Vienna, Austria. https://meetingorganizer.copernicus.org/EGU2018/EGU2018-691.pdf

Reports

Galytska, E., A. Rozanov, M. Weber, R. Hommel, K. Weigel, and J. P. Burrows.: SCIAMACHY V6.01 Nitrogen Dioxide Limb Validation. Version 2, 23.11.2017. ESA SCILOV-15 Project. https://earth.esa.int/web/sppa/mission-performance/esa-missions/envisat/sciamachy/cal/val/validation-activities/

Hommel, R., Burrows, J.P., Rozanov, A., Noël, S., Malinina, E., Brinkhoff, L. A., **Galytska, E.**: Role of stratospheric aerosol in climate and atmospheric science (ROSA), Teilprojektspezifischer Schlussbericht des IUP, Universität Bremen, fur das ROMIC-Verbundvorhaben, FKZ 01LG1212A, Technische Informationsbibliothek (TIB) Hannover, doi: 10.2314/GBV:881360309, 2017.

Awards

The 2018 Outstanding Student Poster and PICO (OSPP) Award from the European Geosciences Union (EGU) General Assembly for the PICO.

Galytska, E., Chipperfield, M. P., Rozanov, A., Dhomse, S. S., and Burrows, J. P.: Understanding NO_2 and O_3 changes in tropical mid-stratosphere by means of a chemistry-transport model. https://www.egu.eu/awards-medals/ospp-award/2018/evgenia-galytska/

Contents

I

Introduction and Fundamentals

I. INTRODUCTION AND FUNDAMENTALS

1

Introduction

1.1 Scientific background

Stratospheric ozone (O_3) is one of the most important atmospheric components. It shields the atmosphere from harmful ultraviolet (UV) solar radiation and plays a crucial role in determining the thermal structure and dynamics of the stratosphere (Jacobson, 2002; Seinfeld and Pandis, 2006). The amount of stratospheric O_3 is controlled by a balance between photochemical production and loss mechanisms. However, atmospheric dynamics play an important role in determining the conditions at which these photochemical and chemical reactions take place. As a result, the O_3 global distribution and inter-annual variability are governed by transport processes, e.g. the Brewer-Dobson Circulation (BDC). Taking into account such complex chemical-dynamical interconnections, any changes of stratospheric O_3 are of significant importance for climate change.

Despite the fact that the formation of O_3 near the surface does not significantly contribute to stratospheric O_3, the emission of long-lived, unreactive molecules near the surface enables O_3 loss mechanisms in the stratosphere through the production of oxides; the source gases are uplifted, destroyed by solar radiation, and the products then react with O_3. This mechanism is observed when the oxides of nitrogen (NO_x), hydrogen (HO_x), chlorine (ClO_x) and bromine (BrO_x) react with O_3. The decline of O_3 is even more pronounced during polar spring with the onset of the heterogeneous chemistry, which occurs on the surface of aerosols or Polar Stratospheric Clouds (PSC) at cold temperatures (e.g. Solomon, 1999). To limit the negative impact of man-made halogenated substances on the stratospheric O_3 layer, the United Nations Vienna Convention for the Protection of the Ozone Layer was signed in 1985. Its Montreal

Protocol and amendments (see WMO, 2014, and references therein) have led to the banning of O_3-depleting species. Moreover, this has had a positive impact on reducing some of the anthropogenic chemicals responsible for global warming.

The recent analysis of O_3 data from various satellite instruments showed that in spite of the recognised recovery in global stratospheric O_3, there is a region in the stratosphere where O_3 concentrations were declining during the first decade of the XXI century. This region is known as the tropical middle stratosphere, where a decrease of O_3 is associated with NO_x increase, which is formed from the nitrous oxide (N_2O) that is transported from the troposphere. The impact of N_2O on both climate change and stratospheric O_3 is significant enough to necessitate further controls on its emissions. However, N_2O is not regulated by the Montreal Protocol. Anthropogenic N_2O is only regulated by the Kyoto Protocol to the United Nations Framework Convention on Climate Change (UNFCCC) and is expected to be the dominant contributor to O_3 depletion in the XXI century (Ravishankara et al., 2009). Due to the long global lifetime of N_2O, which exceeds 100 years (e.g. Portmann et al., 2012), its distribution is affected by changes in BDC. Therefore, such complex chemistry-dynamical interaction raises the attention and fosters scientific activities, which is also a focus of this thesis.

1.2 Motivation

The global composition of the atmosphere has been actively monitored since the 1980s by remote sensing measurements from ground and space. Therefore, the data record of atmospheric trace gases is now long enough to be analyzed and validated.

Significant O_3 changes in the specific area of the atmosphere, tropical middle stratosphere was observed by SCIAMACHY measurements. One of the hypotheses of O_3 changes in the tropical middle stratosphere is associated with variability in the stratospheric dynamics. To test this hypothesis it is important to 1) have an atmospheric model, which adequately describes all relevant aspects of chemical-dynamical processes in the stratosphere, and 2) obtain a sufficiently accurate knowledge of trace gases distribution by means of e.g. satellite measurement techniques. The application of both reliable Chemistry-Transport Model (CTM) and satellite data are the appropriate tools to test the hypothesis of O_3 changes, which will be answered and clarified in this thesis.

Atmospheric modelling helps to interpret and quantify physical and chemical processes in the atmosphere, especially those complex and non-linear chemical interactions that are quite

common (Holloway and Wayne, 2010). Since the beginning of the 2000s, atmospheric modelling has become an important research tool at the Institut für Umweltphysik (IUP), University of Bremen. The stratospheric 3-D CTM TOMCAT was brought from the University of Leeds, U.K. by Dr. Björn-Martin Sinnhuber and was later called the Bremen 3-D Chemistry-Transport Model (B3DCTM). For more than 10 years, the model was developed and improved by a number of young scientists at the IUP, e.g. Aschmann et al. (2009), Kiesewetter et al. (2010), Sinnhuber et al. (2012), Wieters (2013). B3DCTM became an independent development branch, as the TOMCAT model was also further developed in the scientific team of Prof. Martyn P. Chipperfield (for more details see Chipperfield, 2006).

Given the two development branches of the model, it was important to understand how different improvements affected its performance. Thus, the initial step of the research presented in this thesis was the evaluation of the performance of B3DCTM, including its comparison with the SCanning Imaging Absorption spectroMeter for Atmospheric CHartographY (SCIAMACHY) observations, and with the TOMCAT model. The comparison was done for several stratospheric species that were measured by SCIAMACHY, i.e. O_3, nitrogen dioxide (NO_2), and bromine monoxide (BrO). For N_2O and the dynamical tracer Age of Air (AoA), the Michelson Interferometer for Passive Atmospheric Sounding (MIPAS) satellite data was also involved in the comparison. It was found that TOMCAT agrees better with satellite measurements in comparison with B3DCTM, therefore it was actively involved in further study.

In order to obtain a sufficiently accurate knowledge of trace gases distribution, applied data should be compared with independent satellite instruments. As NO_2 plays an important role in the production and loss of O_3, the quality of both data sets should be validated. While global SCIAMACHY limb O_3 data set was previously validated (presented at the Atmospheric Composition Validation and Evolution Workshop 2016 by Dr. Alexey Rozanov), in this thesis SCIAMACHY limb NO_2 data set was compared with co-located observations from various limb and occultation sounders. As further discussed in Chapters 2 and 6, NO_2 has a pronounced diurnal variation; hence it is not directly comparable if the measurements were performed at different illumination conditions. Consequently, NO_2 should be validated taking into account its diurnal change. Such a comparison of SCIAMACHY limb NO_2 V3.1 was performed by Bauer et al. (2012), who used data from occultation satellite instruments and photochemically corrected it to the illumination conditions of the SCIAMACHY limb measurements. To photochemically correct occultation profiles Bauer et al. (2012) applied the look-up tables from the Pratmo photochemical model (Prather, 1992; McLinden et al., 2000). These tables imply

numerous limitations, both in time (the NO_2 diurnal cycle is available for only three days in a month) and in space (only at 2.5° latitude steps). A more sophisticated method was applied 7 years earlier by Bracher et al. (2005), who used a 2-D model to reproduce each measured occultation NO_2 profile, and also a 1-D model to simulate the diurnal change for each of these profiles.

In this thesis, different models and schemes to photochemically correct stratospheric NO_2 were investigated. For example, the Pratmo model from the University of Saskatchewan only runs on Windows machines, which currently makes its application on the Unix/Linux systems at the IUP challenging, as it requires the migration of all data sets. Consequently, there was a clear need for a method that would avoid the spatio-temporal restriction given by the Pratmo look-up tables and the difficulties of data transfer as well. Considering different solutions, it was found that the TOMCAT model, which showed good agreement in stratospheric trace gases distribution compared to satellite measurements, has all the capabilities needed for the validation and photochemical correction of NO_2 profiles. While TOMCAT is sampled for specific satellite measurements at given times and locations, a related 1-D model simulates the diurnal NO_2 change of each measured profile with a time step of one minute. Taking into account the obvious advantages of the TOMCAT 3-D and 1-D (column) models, an improved scheme of NO_2 validation was developed and applied for the first time.

After the validation results for the SCIAMACHY scientific NO_2 product showed good agreement with various satellite instruments that measure at different viewing geometries, the analysis of NO_2 changes in the stratosphere and their impact on O_3 was performed. In particular, while global stratospheric O_3 tends to recover, a small region of O_3 decline was first found by Dr. Claus Gebhardt (first presented at the Quadrennial Ozone Symposium 2012, see also Gebhardt et al., 2014). With the application of SCIAMACHY data, Gebhardt et al. (2014) found that in the tropical stratosphere at around 30-35 km altitude the decrease of O_3 is associated with an increase of NO_2. Since then, several studies have analyzed different data sets, and have shown a decrease in O_3 in the tropical middle stratosphere during a very similar period (Kyrölä et al., 2013; Eckert et al., 2014; Nedoluha et al., 2015b). However, the reasons for this O_3 decline were not clarified, apart from the connection with NO_2 that was given by Gebhardt et al. (2014). The findings of Nedoluha et al. (2015b) were the most relevant in terms of explaining the observed trends in the tropical middle stratosphere. They linked the decrease of O_3 to an assumed slowdown of the tropical upwelling. However, the authors did not show that such a dynamical perturbation in the stratosphere indeed occurred.

In this study, the analysis of the tropical middle stratospheric changes of O_3 and NO_2 was performed based on the SCIAMACHY measurements and the TOMCAT model, which reproduces well observed variability. Additional TOMCAT simulations with different chemical and dynamical forcings were done to diagnose the primary causes of observed changes. This thesis provides a complex interpretation of chemical-dynamical interactions between seasonal variability of stratospheric dynamics (by means of AoA) and its impact on annual mean changes in the chemical composition in the tropical middle stratosphere.

1.3 Outline of the thesis

The primary objective of this thesis is to analyse the spatio-temporal variations of stratospheric O_3 and NO_2 retrieved from the satellite measurements from the SCIAMACHY instrument, and to compare them with 3-D CTMs, B3DCTM and TOMCAT, in order to validate SCIAMACHY NO_2 measurements, and to improve the understanding of the long-term changes of the trace gases in the stratosphere.

This thesis is divided into three parts. Part I "Introduction and Fundamentals" gives a brief overview of the atmospheric chemistry (Chapter 2) and dynamics (Chapter 3). Chapter 2 presents an overview of the main mechanisms of the formation and loss of trace species such as O_3, N_2O, and NO_2, the peculiarities of their photochemical processes, and their changes from diurnal to seasonal scales. Chapter 3 discusses the most important dynamical patterns in the stratosphere, such as BDC, El Niño Southern Oscillation (ENSO), and Quasibiennial oscillation (QBO), which affect the distribution of trace species.

Part II "Methodology and data sources" consists of Chapters 4-7 and is dedicated to a description of the data sources used in this study, including both satellite measurements and model experiments, as well as major diagnostics for the validation and photochemical correction of NO_2 and statistical approaches to better understand changes in the stratospheric composition. Apart from a brief history of satellite measurements, Chapter 4 describes different measurement techniques from space, satellite instruments, and the data used in this study. Chapter 5 gives an overview of atmospheric modelling and reviews the principal differences of various modelling approaches. Chapter 6 reports on the procedure of step-by-step model-based photochemical correction of stratospheric NO_2. Chapter 7 describes multivariate linear regression, applied in the current study to estimate the long-term changes of the trace species in the stratosphere.

Part III "Results" comprises Chapters 8-11 and focuses on the obtained results. Namely, Chapter 8 reports results on the comparison between model simulations, i.e. B3DCTM and TOMCAT, and satellite measurements. Apart from chemical species, i.e. O_3, N_2O, NO_2, BrO, the dynamical tracer AoA was also considered in the analysis. In Chapter 9, the results of the validation of the SCIAMACHY scientific NO_2 profiles are presented, based on the outcome of Chapter 6. Chapter 10 presents the linear changes of observed and modelled O_3 and NO_2, and possible reasons for their occurrence. The final Chapter 11 of this thesis entails a discussion of the achieved results, as well as suggestions for further research.

2

Atmospheric species

2.1 Ozone

2.1.1 Chapman mechanism

O_3 is one of the most important components of the atmosphere, which plays a significant role in its chemistry, even though in terms of abundance it belongs to the atmosphere's minor species. O_3 concentrations are rather variable in the atmosphere and strongly depend on the altitude. Around 90% of all atmospheric O_3 is located in the stratosphere. It absorbs harmful ultraviolet solar radiation and plays a key role in determining the thermal structure and therefore the dynamics of the stratosphere (e.g. Jacobson, 2002; Seinfeld and Pandis, 2006; Weber et al., 2011). The overall abundance of stratospheric O_3 is mainly determined by a balance between the production and loss, controlled by photochemical mechanisms, while its global distribution and inter-annual changes are determined by transport processes in conjunction with their superimposed variability of different origins and periodicity (e.g. BDC, ENSO, QBO). Around 10% of atmospheric O_3 is located in the lower tropospheric layer (below 8 km at the poles and 15-18 km at the equator) and acts as a greenhouse gas and air pollutant.

The commonly used metric for the representation of the observational data, i.e. O_3, NO_2 etc., is the number density (ND); it is determined as the number of molecules per unit volume of air and expressed in units (molecules cm^{-3}). However, due to the compressibility of the atmosphere ND is not conserved following the motion (Andrews et al., 1987). For dynamical research, volume mixing ratio (VMR) is the preferred measure of the concentration (Andrews et al., 1987), which is defined as the number of molecules of e.g. O_3 per molecules of air. Figure 2.1a shows zonally averaged climatological mean O_3 profiles observed by SCIAMACHY

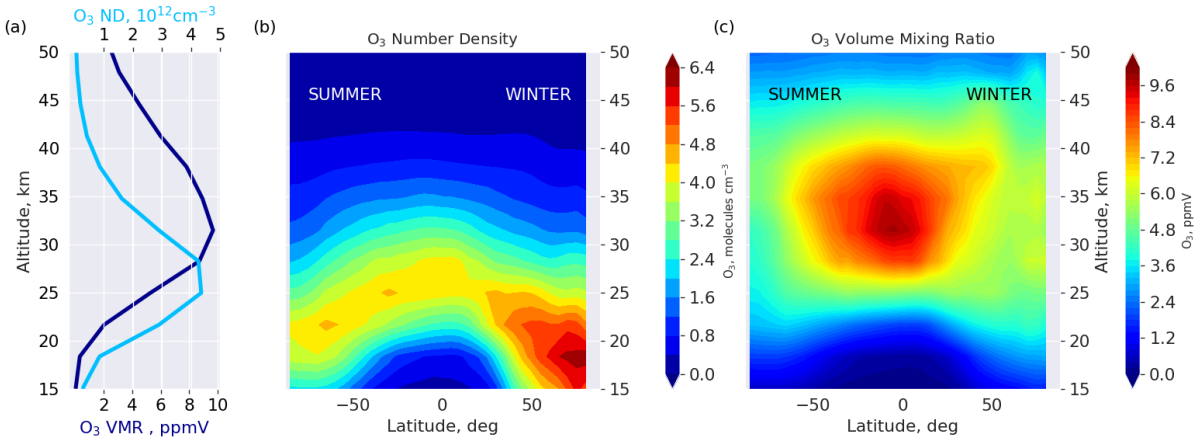

Figure 2.1: SCIAMACHY zonally averaged climatological mean O_3 (a) profiles for the tropical latitudes (10°S-10°N) in both, units of VMR (dark blue) and ND (light blue) during August 2002-April 2012, (b) latitude-altitude distribution in ND and (c) latitude-altitude distribution in VMR during DJFs 2002-2012.

(further described in Sect. 4.3.1) in the period from August 2002 to April 2012 for the tropical region (10°S-10°N), both in units of VMR (dark blue) and ND (light blue). The largest O_3 ND in the tropical region is found between the altitudes of 20-30 km, where peak concentrations exceed 4×10^{12} molecules cm^{-3}. This region is commonly referred to as the stratospheric ozone layer. The peak in mixing ratio of O_3 reaches 10 parts per million by volume (ppmV) and occurs at higher altitudes, between around 30-35 km. A typical distribution of O_3 in the stratosphere is illustrated in Fig. 2.1b-c. It shows zonally-averaged climatological mean O_3 ND (panel b) and VMR (panel c) as a function of latitude and altitude from the SCIAMACHY measurements during boreal winters December-January-February (DJF) 2002-2012. Northern Hemisphere (NH) winter months were chosen to clearly represent the hemispheric asymmetry of the O_3 distributions.

Current research focuses on the stratospheric variability of the chemical species, e.g. O_3. Therefore, to set the scene for the understanding of chemical O_3 changes, the mechanism of O_3 production and its loss is discussed below. Stratospheric O_3 is produced in the areas where the necessary high-energy photons are present in the solar spectrum. Chapman (1930) was the first who proposed the mechanism that explained O_3 formation and loss (commonly referred to as the Chapman cycle).

O_3 is formed in the atmosphere via photodissociation of molecular oxygen (O_2) mostly within the Herzberg continuum (200-242 nm; Nicolet, 1981). Absorption by O_2 occurs at

shorter wavelengths (e.g. Schumann-Runge bands, 175-200 nm) in the upper stratosphere, but far more radiation with λ = 195-242 nm reaches the middle and lower stratosphere. Therefore, in the middle stratosphere the short-wavelength UV radiation from the Sun breaks apart an O_2 molecule and generates two oxygen (O) atoms:

$$O_2 + h\nu \xrightarrow{\lambda < 242\,\text{nm}} O + O \tag{R1}$$

In the lower altitudes, for instance in the upper troposphere at around 10 km altitude, there is not enough short-wave radiation to produce atomic O via Reaction (R1).

Almost all O_3 in the stratosphere is produced by combination of atomic oxygen with O_2:

$$O + O_2 + M \longrightarrow O_3 + M \tag{R2}$$

where M represents a third body, usually N_2 or O_2 (Jacob, 1999), which carry off the excess energy from O_3 formation (Holloway and Wayne, 2010). Reactions (R1) and (R2) occur continually whenever shortwave UV radiation is present in the stratosphere. Consequently, the strongest O_3 production occurs in the tropical middle stratosphere. In the next reaction step, the photolysis of O_3 with lower-energy photons in wavelengths of the Hartley bands (242-310 nm) produces excited singlet oxygen O(^{1}D) or in the Huggins band (310-400 nm) produces ground-state atomic oxygen O(^{3}P):

$$O_3 + h\nu \xrightarrow{242 < \lambda < 310\,\text{nm}} O_2 + O(^1D) \tag{R3a}$$

$$\xrightarrow{310 < \lambda < 400\,\text{nm}} O_2 + O(^3P) \tag{R3b}$$

The photolysis of O_3 via Reaction (R3a) is the major source of excited atomic oxygen O(^{1}D) in the stratosphere, which in turn is rapidly quenched to the electronic ground state by collision with a third-body molecule, i.e. O(^{1}D) + M $\rightarrow$ O + M. The final reaction within the Chapman cycle of O_3 and atomic oxygen via Reaction (R4) is too slow to destroy O_3 in the rate it is produced globally, since O_2 molecule recombines immediately with an O atom and regenerates O_3 via Reaction (R2).

$$O_3 + O \longrightarrow O_2 + O_2 \tag{R4}$$

In the upper stratosphere and mesosphere O_3 shows a diurnal variation with an amplitude of up to 10% of the daily mean (Sakazaki et al., 2013, and references therein), with a pronounced decrease during the daytime and increase at night. Such diurnal variations are explained by partitioning of O and O_3, which is driven by photochemistry (Vaughan, 1982). Brasseur and

Solomon (2005) showed that the photochemical lifetime of odd oxygen ($O_x = O + O_3$) decreases exponentially from a few weeks at 30 km to around 1 day at 40 km, and a few hours at 50-60 km. In the current study the analysis of O_3 is limited to 40 km altitude, therefore diurnal changes were not taken into consideration.

2.1.2 Catalytic ozone destruction cycles

Chapman's photochemical mechanism could explain the formation of the ozone layer, but could not describe the O_3 equilibrium concentrations. While Reaction (R4) is slow to destroy O_3, other chemical cycles can catalyse the removal of O_3. A considerable O_3 loss occurs through reaction with NO_x, HO_x, ClO_x, and BrO_x. The catalytic reactions can be summarised as follows:

$$X + O_3 \longrightarrow XO + O_2 \tag{R5}$$

$$XO + O \longrightarrow X + O_2 \tag{R6}$$

where X stands for a catalyst (OH, H, NO, Cl, and Br, which belong to HO_x, NO_x, ClO_x and BrO_x families), and XO is the intermediate product. Within such catalytic cycle the O_3 molecule is completely lost, while the catalyst X is reformed to destroy another O_3. The net effect of Reactions (R5) and (R6) is the same as of reaction (R4).

The first-identified catalytic O_3-depleting cycle involved hydrogen radicals (see Seinfeld and Pandis, 2006, and references therein). Stratospheric OH, which actively participates in the HO_x catalytic cycle is produced via reaction of H_2O with $O(^1D)$:

$$H_2O + O(^1D) \longrightarrow OH + OH \tag{R7}$$

and via reaction of CH_4 with $O(^1D)$:

$$CH_4 + O(^1D) \longrightarrow OH + CH_3 \tag{R8}$$

Among the two established HO_x catalytic cycles (for more details see Seinfeld and Pandis, 2006), one dominates in the upper stratosphere, above 40 km and the another one in the lower stratosphere, below 20 km. The catalytic NO_x cycle leads to O_3 destruction in the middle stratosphere, below 35 km and will be further described in Sect. 2.2.2. Atmospheric ClO_x and BrO_x following Reactions (R5) and (R6) deplete O_3 in the high and middle latitudes, also causing the so-called "ozone hole" (further explained in Sect. 2.1.3).

2.1.3 Polar ozone chemistry

Significant decrease of stratospheric O_3 columns during the spring months was first observed at Halley Bay station, Antarctica in 1985 by scientists from the British Antarctic Survey (Farman et al., 1985). Measured O_3 profiles showed that the depletion of O_3 occured in the lowest stratosphere between 10 and 20 km, which normally contains most of the total O_3 column in polar spring (Jacob, 1999, Fig. 10.10). The discovered "Antarctic ozone hole" could not be explained by catalytic destruction cycles, discussed in Sect. 2.1.2. Aircraft and satellite missions conducted in the late 1980s showed that O_3 depletion was associated with high ClO content, which lead to a new catalytic cycle involving a self-reaction of ClO to produce ClOOCl dimer:

$$\mathrm{ClO + ClO + M \longrightarrow ClOClO + M} \tag{R9}$$

which is then photolysed into Cl atoms as follows:

$$\mathrm{ClOClO + h\nu \longrightarrow ClOO + Cl} \tag{R10}$$

$$\mathrm{ClOO + M \longrightarrow Cl + O_2} \tag{R11}$$

$$\mathrm{Cl + O_3 \longrightarrow ClO + O_2} \tag{R12}$$

The ClO + ClO catalytic cycle shown in Reactions (R9-R12) is activated in late winter-springtime with the presence of sunlight. During winter the depletion of O_3 is limited due to a lack of solar light to photolyse ClOClO via Reaction (R10). Overall the catalytic cycle of ClO self-reaction accounts for around 70% of total O_3 loss in the Antarctic region. Another 30% involve the catalytic cycle with Br radicals. Produced in Reaction (R12) ClO reacts with BrO and processes three branches:

$$\mathrm{ClO + BrO \longrightarrow Br + Cl + O_2} \tag{R13a}$$

$$\mathrm{\longrightarrow Br + OClO} \tag{R13b}$$

$$\mathrm{\longrightarrow BrCl + O_2} \tag{R13c}$$

Br and Cl atoms produced in Reaction (R13a) react with O_3 and complete a catalytic cycle via Reactions (R12) and (R14).

$$\mathrm{Br + O_3 \longrightarrow BrO + O_2} \tag{R14}$$

Both cycles ClO + ClO and ClO + BrO have the net reaction $2O_3 \rightarrow 3O_2$.

Another important aspect of the Antarctic O_3 depletion is the formation of vortex as a result of cooling and subsequent descent of the air during the winter. A strong westerly circulation is set up (winds of around 100 m/s) as a result of the contrast in heating between the tropics and poles. Such vortex causes the development of very cold air (around -78°C) and therefore forming PSCs via condensation of water and nitric acid (HNO_3) between 15 and 25 km altitude.

Chlorine atoms that were formed by the photodissociation of chlorofluorocarbons (CFCs) are transported via the BDC (see Sect. 3.1) to high latitudes and via reaction with methane (CH_4) or NO_2 form hydrogen chloride (HCl) and chlorine nitrate ($ClONO_2$), respectively.

$$Cl + CH_4 \longrightarrow HCl + CH_3 \tag{R15}$$

$$ClO + NO_2 + M \longrightarrow ClONO_2 + M \tag{R16}$$

PSCs together with aqueous aerosols (e.g. H_2SO_4) provide the surfaces for HCl and $ClONO_2$ to convert to Cl_2:

$$ClONO_2 + HCl \xrightarrow{PSC} Cl_2 + HNO_3 \tag{R17}$$

As a result of Reaction (R17) molecular chlorine is released as a gas, which quickly photolyzes in sunlit air:

$$Cl_2 + h\nu \xrightarrow{\lambda < 450\,nm} Cl + Cl \tag{R18}$$

and forms ClO via Reaction (R12). Produced via Reaction (R17), HNO_3 stays in the ice particles, which can transport HNO_3 outside the vortex down to the troposphere. This and related heterogeneous reactions suppress the abundance of NO_2 by transporting active nitrogen out of the stratosphere in the form of HNO_3, so ClO cannot reform the $ClONO_2$ reservoir (Brasseur and Solomon, 2005; Holloway and Wayne, 2010) via Reaction (R16). Permanent loss of NO_y, known as denitrification, occurs at lower temperatures than the loss of NO_x, denoxification. Low temperatures also cause the reduction of stratospheric $ClONO_2$. Up to 1985 such heterogeneous processes as shown in Reaction (R17) were neglected (Holloway and Wayne, 2010), that is why the O_3 hole in polar regions was not predicted.

In the Arctic stratosphere the mechanism of O_3 depletion is the same, however it is less pronounced. The vortex in the NH is less stable than that in the Southern Hemisphere (SH). As a result there is less PSCs formed and O_3 loss is weaker.

2.2 Nitrogen compounds

2.2.1 Nitrous oxide

N_2O is an important greenhouse gas, produced at the surface and relatively inert in the troposphere (Portmann et al., 2012). N_2O is emitted at the surface by anthropogenic and microbial processes (Trenberth, 1992; Bregmann et al., 2000). The principal atmospheric source of N_2O is denitrification in anaerobic environments. The oceans also significantly contribute as a source of N_2O. Biomass burning, which is the major contributor of anthropogenic origin, belongs to the secondary source of N_2O. Among other anthropogenic sources are the production of fertilisers, industrial processes, and formation in automobile exhaust. Tropical upwelling across the tropopause is the major source of N_2O in the stratosphere. N_2O decomposes in the stratosphere mainly by solar photodissociation, where it affects O_3 concentrations. Around 90% of all N_2O is photolysed by UV radiation between 180-230 nm (McLinden et al., 2003) with the maximum absorption around 180-190 nm (Keller-Rudek et al., 2013). Thus the overall atmospheric lifetime of N_2O is defined by the stratospheric photolysis (Trenberth, 1992):

$$N_2O + h\nu \xrightarrow{\lambda < 230\,\mathrm{nm}} N_2 + O(^1D) \tag{R19}$$

Even if the photolysis of N_2O via Reaction (R19) produces $O(^1D)$, the main source of $O(^1D)$ in the stratosphere is the photolysis of O_3 via Reaction (R3a). The remaining 10% of N_2O is removed by the reaction with $O(^1D)$ that occurs through two channels. One of these (about 5% of overall N_2O loss) contributes to NO production:

$$N_2O + O(^1D) \longrightarrow NO + NO \tag{R20a}$$

$$\longrightarrow N_2 + O_2 \tag{R20b}$$

Figure 2.2 shows N_2O profile (panel a, parts per billion by volume (ppbV)) and N_2O loss (panel b, ppbV per year) in the tropical stratosphere from the TOMCAT model averaged over the period 2004-2012. The description of the TOMCAT CTM is provided below in Sect. 5.3.1. A significant N_2O decrease with altitude is seen in Fig. 2.2a, in particular a decline starting from around 18-20 km altitude. Figure 2.2b shows that the largest ($\sim$90%) N_2O loss is due to the photolysis via Reaction (R19, orange), which becomes important at around 18-20 km

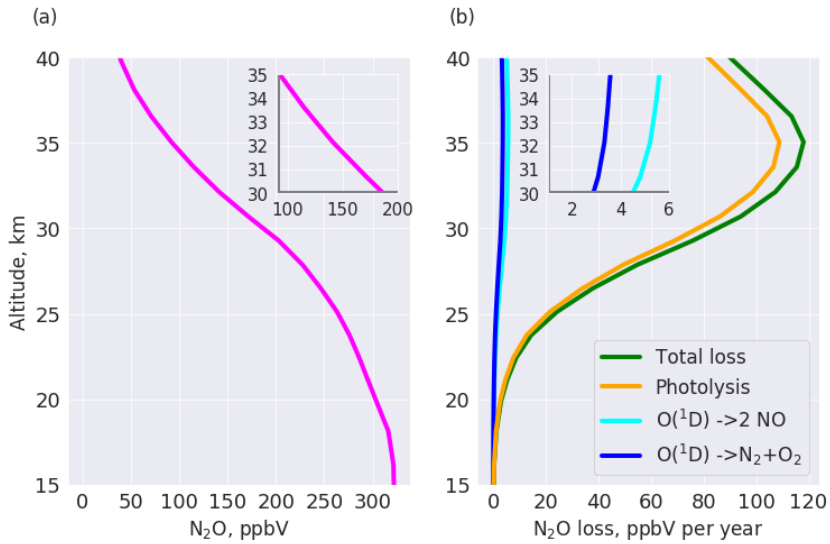

Figure 2.2: Average profiles of (a) N_2O (ppbV) and (b) N_2O loss (ppbV per year) from the TOMCAT model in the tropical region 10°S-10°N for the period 2004-2012. Colour coding in panel (b) indicates the sources of N_2O loss: total loss - green; loss via photolysis, Reaction (R19) - yellow; loss via oxidation with NO_x production, Reaction (R20a) - bright blue; loss via oxidation without NO_x production, Reaction (R20b) - dark blue.

altitude. About 5% of N_2O reacts with $O(^1D)$ above 26 km, where the concentration of $O(^1D)$ starts increasing due to the Reaction (R3a).

Bregmann et al. (2000, and references therein) stated that the local chemical lifetime of N_2O varies significantly: it decreases from more than thousands of years in the troposphere, to the order of 100 years in the lowermost stratosphere, and to weeks in the middle stratosphere. In Fig. 2.3 the average lifetime of N_2O modelled by TOMCAT in the tropics averaged for the period 2004-2012 is calculated as the ratio of mean N_2O concentration (shown in Fig. 2.2a) and its total loss (Fig. 2.2b, green) at each altitude. Calculated N_2O lifetime is also altitude dependent and decreases from around 140 years at 20 km to less than 1 year above 34 km. In particular, between 30-35 km altitudes, the N_2O lifetime decreases by a factor of two (Fig. 2.3).

From a climate point of view, N_2O emissions need to be further controlled. However, N_2O is not included for the regulations in the Montreal Protocol (WMO, 2014). Only the Kyoto Protocol of the UNFCCC regulates anthropogenic N_2O, which is expected to be the dominant anthropogenic contributor to O_3 depletion in the 21^{st} century (Ravishankara et al., 2009).

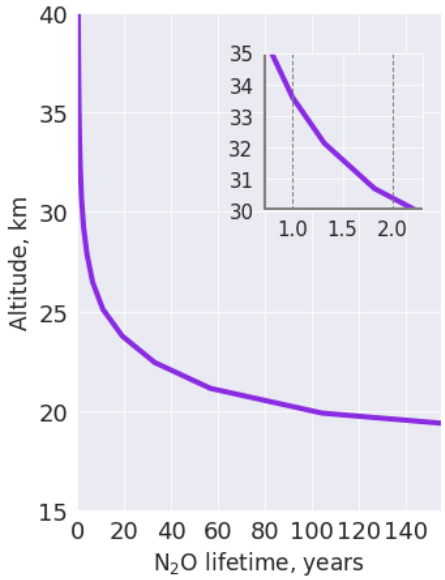

Figure 2.3: Average N_2O lifetime (years) from the TOMCAT model in the tropical region 10°S-10°N for the period 2004-2012.

2.2.2 Nitrogen oxides

Nitrogen oxides (NO_x = NO + NO_2) are very important species in atmospheric chemistry. In the troposphere, human activities, in particular biomass burning and fossil-fuel combustion are the major sources of NO_x (around 50% globally). Among the natural sources of NO_x are microbial processes in the soils, oxidation of biogenic NH_3, and lightnings (Wayne, 2000; Jacobson, 2002). In the stratosphere, the primary source of NO_x is the oxidation of N_2O via Reaction (R20a).

Up to 70% of the stratospheric O_3 loss is caused by NO_x species (see Bauer et al., 2012, and references therein). In particular, Portmann et al. (2012, Fig.2a) showed that the relative mean global O_3 loss in the middle stratosphere is dominated by the NO_x cycle, which is the largest near the O_3 maximum. Between about 25 and 40 km nitric oxide (NO) rapidly reacts with O_3 to produce NO_2, which causes significant O_3 loss, corresponding the catalytic cycle earlier shown via Reactions (R5) and (R6) as follows:

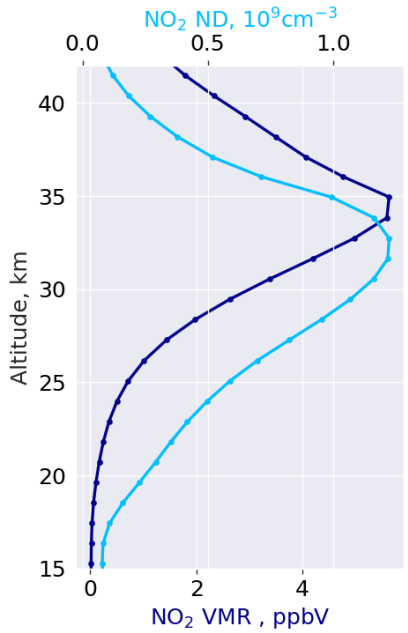

Figure 2.4: SCIAMACHY zonally averaged climatological mean NO_2 profiles for tropical latitudes in both, units of VMR (dark blue) and ND (light blue) during August 2002-April 2012, similar to Fig. 2.1a.

$$NO + O_3 \longrightarrow NO_2 + O_2 \tag{R21}$$

NO_2 molecule quickly reacts with (ground state) oxygen atom to reform NO:

$$NO_2 + O \longrightarrow NO + O_2 \tag{R22}$$

In the middle stratosphere, the exchange time between NO and NO_2 via Reactions (R21) and (R22) is approximately one minute during daytime. The recognition of a NO_x-catalyzed mechanism of O_3 sink was a crucial lead towards identifying the missing O_3 loss in the Chapman mechanism (Jacob, 1999). Apart from being destroyed via Reaction (R22) NO_2 also photolyzes:

$$NO_2 + h\nu \xrightarrow{\lambda < 405\,\text{nm}} NO + O(^3P) \tag{R23}$$

Reactions (R21) and (R23) form a null cycle, which is ineffective as a catalyst and have the net effect of O_3 photolysis via Reaction (R3a) and (R3b). The tropical stratospheric profile of NO_2 is shown in Fig. 2.4, similar to Fig. 2.1a. The largest NO_2 ND in the tropical region is between 30-35 km altitude, where peak reaches around 1.2×10^9 molecules cm^{-3}. The peak of tropical NO_2 VMR exceeds 5 ppbV and is observed at around 35 km altitude.

In the stratosphere, NO_x species show large diurnal variations, as the reactions that govern their production and loss significantly, depend on sunlight and the relative abundance of NO and NO_2 is determined by the position of the Sun. During the day, the NO_x equilibrium is pushed towards NO (see Brohede et al., 2007), as e.g. Reaction (R23) depends on the presence of light. After the sunset the abundance of NO_2 rapidly increases at the cost of NO. Figure 2.5 shows an example of the change of NO_2 VMR within one day simulated by the TOMCAT 1-D model (see Sect. 6.3.1.4) for four altitudes: 25 km, 30 km, 35 km, and 40 km. Vertical pink areas in Fig. 2.5 indicate the periods of sunrise and sunset, which is around 90° solar zenith angle (SZA).

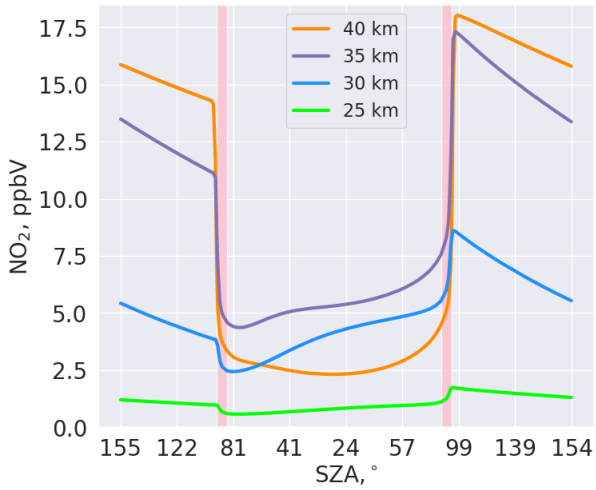

Figure 2.5: Example of NO_2 (ppbV) diurnal variation from the TOMCAT 1-D model. Colour coding depicts the altitude: 25 km - green, 30 km - blue, 35 km - purple, 40 km - orange.

During the night, a slow decrease of NO_2 is observed due to formation of reservoir species, such as NO_3, N_2O_5, HNO_3, which basically converts NO_x species to NO_y. The combination of chemical family NO_x with its reservoirs forms another family $NO_y = NO_x + NO_3 + 2{\times}N_2O_5 + HNO_3$. The reaction of NO_2 with O_3 produces NO_3:

$$NO_2 + O_3 \longrightarrow NO_3 + O_2 \tag{R24}$$

Subsequently NO_3 reacts with NO_2 and forms night-time reservoir N_2O_5:

$$NO_3 + NO_2 + M \longrightarrow N_2O_5 + M \tag{R25}$$

In the stratosphere, N_2O_5 behaves as an unreactive reservoir for NO_x and contains 5-10% of the total NO_x budget (Wayne, 2000). N_2O_5 can be formed only at night, because during the day NO_3 is photolysed within a few seconds:

$$NO_3 + h\nu \xrightarrow{\lambda < 620\,nm} NO + O_2 \quad \text{(R26a)}$$

$$\xrightarrow{\lambda < 620\,nm} NO_2 + O \quad \text{(R26b)}$$

The photolysis of N_2O_5 at stratospheric temperatures is slower in comparison with NO_3, which explains slight positive NO_2 trend during the day in the middle stratosphere (see Fig. 2.5).

$$N_2O_5 + h\nu \xrightarrow{200 < \lambda < 400\,nm} NO_3 + NO_2 \quad \text{(R27)}$$

During the daytime, an additional sink of NO_x occurs via formation of HNO_3 through the three-body reaction:

$$NO_2 + OH + M \longrightarrow HNO_3 + M \quad \text{(R28)}$$

The OH abundance is too low at night to lead the oxidation of NO_x via Reaction (R28). This is because there is no $O(^1D)$, which is formed via Reaction (R3a) to oxidise water vapour via Reaction (R7). In the presence of stratospheric aerosol, HNO_3 can be also formed via the heterogeneous reaction as follows:

$$N_2O_5 + H_2O \longrightarrow HNO_3 + HNO_3 \quad \text{(R29)}$$

The main sinks of HNO_3 are through photolysis and reaction with OH.

$$HNO_3 + h\nu \xrightarrow{200 < \lambda < 315\,nm} NO_2 + OH \quad \text{(R30)}$$

$$HNO_3 + OH \longrightarrow NO_3 + H_2O \quad \text{(R31)}$$

Apart from being photochemically active during the day, NO_2 has also pronounced seasonal changes. Noxon (1975), by analysing ground-based spectra registered at the Fritz Peak Observatory in the Colorado Mountains, USA found that "pronounced winter decrease in stratospheric NO_2 thus exists north of 45°". A few years later Noxon (1979) reported about the existence of a cliff in NO_x, currently known as a Noxon-cliff, in a stable winter stratosphere, i.e. the formation of a relatively abrupt drop in the abundance of NO_2 near 50°N. Moreover, columnar NO_2 increases with latitude in boreal summer, and decreases during boreal winter (Bauer, 2012). Figure 2.6 shows an example of zonally-averaged climatological mean NO_2 in (a) ND and (b) VMR as a function of latitude and altitude observed by SCIAMACHY during boreal

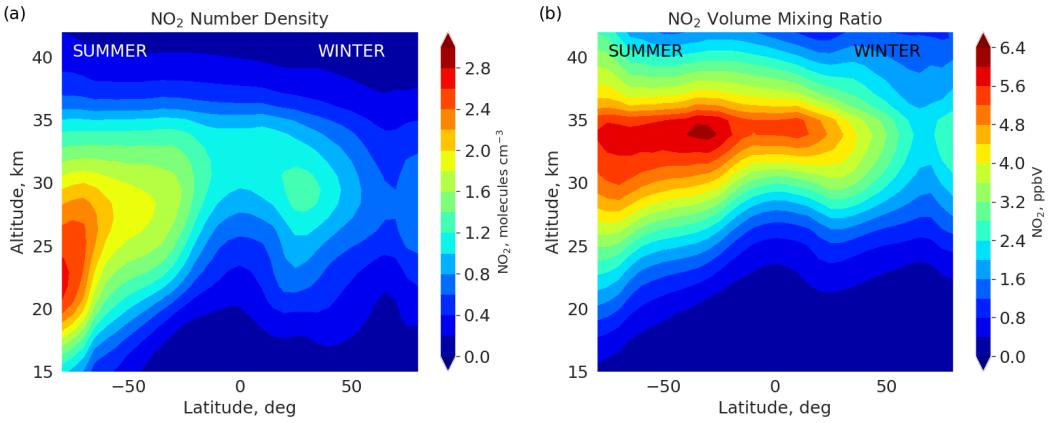

Figure 2.6: SCIAMACHY zonally averaged climatological mean NO_2 latitude-altitude distribution in (a) ND and (b) VMR during DJFs 2002-2012, similar to Fig. 2.1b-c.

winters DJF 2004-2012. A very steep latitudinal NO_2 gradient is seen in both panels of Fig. 2.6. Among the reasons for the pronounced decline of NO_2 during boreal winters are i) longer nights and shorter days, so more N_2O_5 is formed via Reaction (R25) and less is photolysed via Reaction (R27); ii) temperature dependence of Reaction (R27) slows down the formation of NO_2. Consequently, during winter NO_x species are trapped in the reservoirs (Bauer, 2012).

2.3 Bromine compounds

Bromine compounds are also important in O_3 destruction within various catalytic cycles. Among the source gases of bromine compounds are bromoform ($CHBr_3$), methyl bromide (CH_3Br) and halons (bromine-containing halocarbons, used as fire extinguishing agents and fire retardants). However, the most important source, which contributes about half the Br atoms in the stratosphere is CH_3Br. The major sources of CH_3Br in the atmosphere are the oceans, soil fumigation, biomass burning, plant and marsh emissions, automobiles that use leaded gasoline. Wayne (2000) stated that the natural and anthropogenic sources of CH_3Br are roughly comparable. Apart from CH_3Br, there are other H-atom-containing bromine compounds, as CH_2Br_2, $CHBr_3$, CHBr, which release their Br almost immediately on entry into the stratosphere. Halons, $CBrFCl_2$, and $CBrF_3$, release Br slower and at higher altitudes (Seinfeld and Pandis, 2006). The importance of bromine is related to its ability to act as a catalyst for

O_3 destruction. Catalysis takes place through:

$$Br + O_3 \longrightarrow BrO + O_2 \tag{R32}$$

with the main loss of BrO in the upper stratosphere via its reaction with atomic oxygen,

$$BrO + O \longrightarrow Br + O_2 \tag{R33}$$

while in the lower stratosphere BrO is destroyed via photolysis

$$BrO + h\nu \xrightarrow{\lambda < 380\,nm} Br + O \tag{R34}$$

and reaction with NO:

$$BrO + NO \longrightarrow Br + NO_2 \tag{R35}$$

BrO can also be converted to Br via Reactions (R13a), (R13b), (R36) and via reaction with OH, i.e. $Br + OH \rightarrow Br + HO_2$.

Figure 2.7 is similar to Fig. 2.4, but for BrO. The peak of tropical BrO ND is located at 22 km altitude and is around 1.2×10^7 molecules cm^{-3}, which is consistent with Sioris et al. (2006). The peak of tropical BrO VMR is around 12 parts per trillion by volume (pptV) and is located above 25 km.

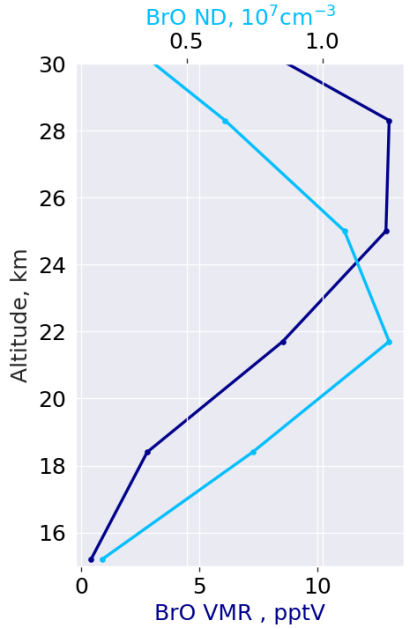

Figure 2.7: Same as Fig. 2.4, but for BrO.

In the troposphere, the concentrations of O atom are way too low to make the cycle of Reactions (R32) and (R33) effective. However, the halogen atom can be regenerated from another reaction that does not require light or atomic oxygen:

$$BrO + BrO \longrightarrow Br + Br + O_2 \tag{R36}$$

Although the concentrations of bromine compounds are much smaller that those of e.g. chlorine, it has very strong O_3 destroying efficiency in different catalytic cycles. The combination of Br- and Cl-catalysed processes is significant, in particular in conditions of polar spring in the Antarctic stratosphere. The coupling reaction of BrO and ClO produces Br and Cl atoms that further react with O_3 (see Sect. 2.1.3 and Reactions (R13a), (R14), and (R12)). As previously mentioned in Sect. 2.1.3, there are two other channels of the interaction of BrO with ClO, which compete with the Reaction (R13a), are Reactions (R13b) and (R13c). Photolysis of OClO, produced via Reaction (R13b), regenerates O, therefore Reaction (R13b) does not cause the loss of odd-oxygen. BrCl from the Reaction (R13c) acts as the temporal reservoir for Br, but it is rapidly photolysed during the daytime.

The concentrations of stratospheric bromine show pronounced diurnal variations. In the absence of PSCs, most of inorganic chlorine is kept in reservoir species HCl and $ClONO_2$. In contrast, HBr is not a major bromine reservoir (Fish et al., 1995, and references therein). BrONO2 is the most abundant inorganic bromine (Br_y = Br + BrO + $BrONO_2$ + HOBr + BrCl + HBr) compound in the stratosphere, apart from BrO (Fish et al., 1995; Brasseur and Solomon, 2005; Wetzel et al., 2017). During sunset $BrONO_2$ is formed via the reaction of BrO and NO_2 as follows:

$$BrO + NO_2 + M \longrightarrow BrONO_2 + M \tag{R37}$$

A small amount of BrO also reacts with ClO (from $ClONO_2$ photolysis) to form BrCl via Reaction (R13c). The nighttime bromine reservoirs do not react, and BrO and BrCl are released at sunrise as both are photolysed.

$$BrONO_2 + h\nu \xrightarrow{\lambda < 390\,\text{nm}} Br + NO_3 \tag{R38a}$$

$$\xrightarrow{\lambda < 390\,\text{nm}} BrO + NO_2 \tag{R38b}$$

$$BrCl + h\nu \xrightarrow{\lambda < 540\,\text{nm}} Br + Cl \tag{R39}$$

Since the NO_3 produced via Reaction (R38a) is readily photolysed and Br atoms react rapidly with O_3 to form BrO via Reaction (R32) at altitudes below 40 km. Consequently,

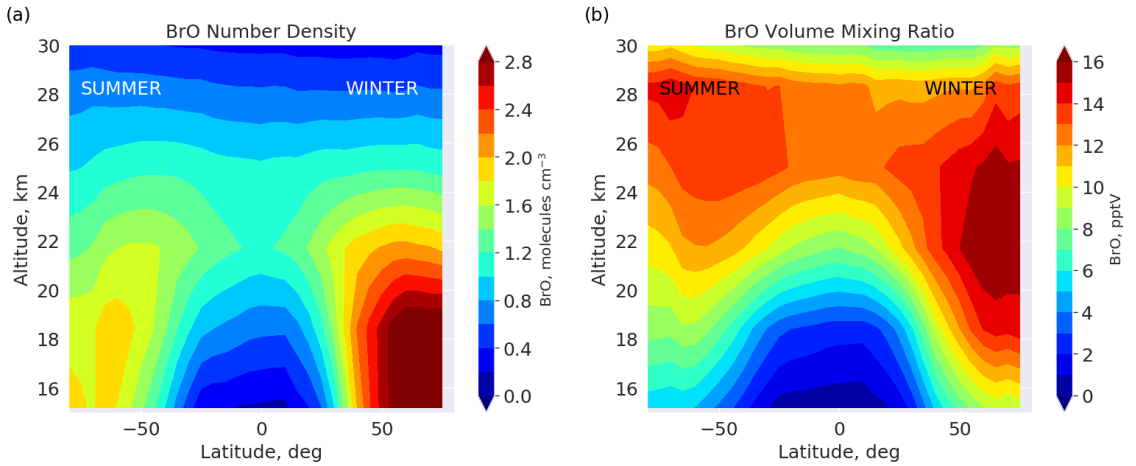

Figure 2.8: Same as Fig. 2.6, but for BrO.

Reactions (R38a) and (R38b) have the same end result. BrO and $BrONO_2$ are then the major bromine species in the stratosphere during the day (Fish et al., 1995).

The seasonal distribution of BrO, measured by SCIAMACHY shows maximum concentration during winter (see Fig. 2.8a,b), which is inversely proportional with that of NO_2 and is in agreement with Richter et al. (1999); Sioris et al. (2006) and Fig. 2.6a-b. Namely, during winter month, NO_2 is kept in reservoir species like N_2O_5 and HNO_3 (see Gebhardt, 2014; Noxon, 1979; Brohede et al., 2007). Note that the altitudes range is different in Fig. 2.6 and Fig. 2.8. A lower concentration of NO_2 results in less formation of $BrONO_2$ via Reaction (R37) and therefore higher BrO abundance (and vice versa during the summer months).

3

Atmospheric dynamics

3.1 Brewer-Dobson Circulation

The BDC is known as the meridional stratospheric circulation that is characterized by the upwelling of the tropospheric air across the tropical tropopause into the stratosphere, which then moves poleward before descending at middle and high latitudes. Such a physical model was proposed by Dobson et al. (1929) and Dobson (1956) while analysing observations of O_3, and by Brewer (1949) while analysing observations of water vapour.

The BDC is characterized by two major processes: 1) the residual mean meridional circulation, i.e. residual circulation and 2) the two-way exchange of air masses, i.e. mixing. Figure 3.1 depicts a scheme of general BDC patterns during boreal NH winter and their consequences for the stratospheric O_3 distribution. The residual circulation is shown by the black arrows, two-way mixing is depicted by yellow, red, and white arrows, which overlay zonally averaged O_3 (ND, molecules cm^{-3}) distribution during boreal winters 2002-2012, measured by the SCIAMACHY satellite instrument.

The crucial driver of the stratospheric BDC is the presence of wave breaking in the stratosphere (see Diallo et al., 2019, and references therein). The wave-driven circulation affects the thermal structure of the stratosphere and, thus, determines the mean stratospheric zonal wind distribution. In the upper troposphere and lower stratosphere (UTLS) synoptic-scale Rossby waves are responsible for driving the circulation poleward throughout the year in both hemispheres (see shaded regions labeled "synoptic" in Fig. 3.1). This is called the "shallow" branch of BDC, which usually occurs at altitudes around 16-22 km (Birner and Bönisch, 2011). A

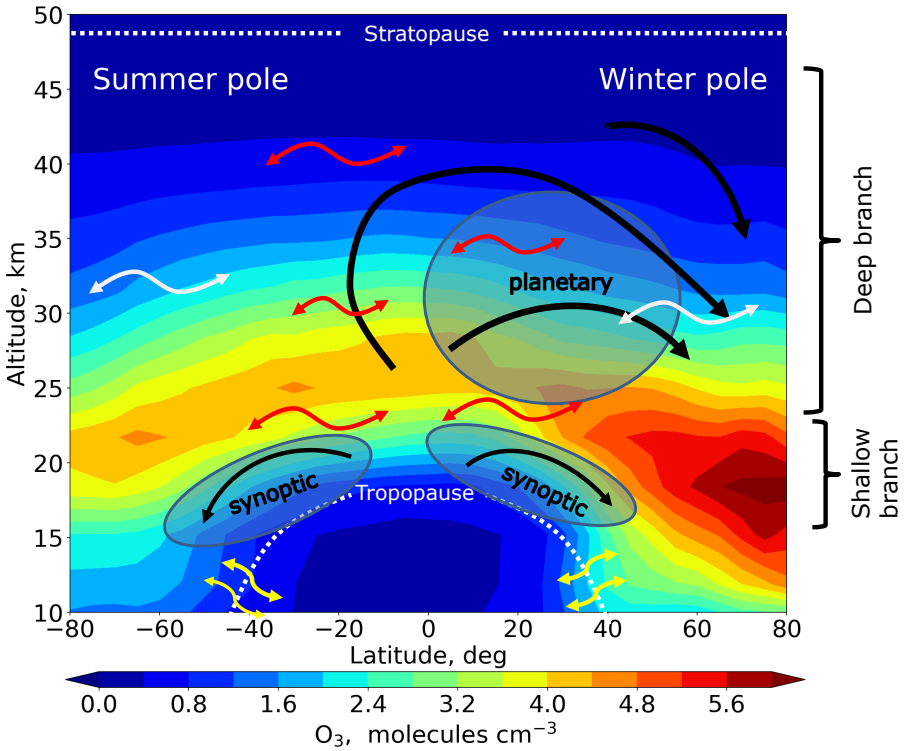

Figure 3.1: The BDC and stratospheric O_3. Residual circulation is shown by the black arrows; two-way mixing between troposphere and stratosphere is shown by yellow arrows, between stratospheric tropical and extratropical regions by red arrows, and within stratospheric extratropical regions by white arrows, which overlay zonally averaged O_3 (molecules/cm^3) distribution during boreal winters 2002-2012, measured by SCIAMACHY. The shaded regions (labeled "synoptic" and "planetary") denote the areas of breaking synoptic-scale and planetary-scale Rossby waves.

recent study by Lin and Fu (2013) separated the shallow branch into the transition (around 16-18.5 km) and the shallow branches (18.5-22 km).

In the middle and upper wintertime stratosphere, large-amplitude planetary-scale Rossby waves dominate, which are propagated from the troposphere (see shaded region labeled "planetary" in Fig. 3.1). In contrast to the NH, the SH is much more quiescent. In the tropical region the circulation extends deep into the tropics and even crosses the equator. The region above 24 km altitude is usually defined as a "deep" branch of the BDC. It is important for the stratospheric chemistry and it processes a small portion of the air that circulates in the stratosphere (Diallo et al., 2012). Strong air mixing is caused by breaking planetary waves, leading to quasi-horizontal mass exchange. Figure 3.1 shows air mixing between the troposphere and the stratosphere with yellow arrows, between the stratospheric tropical and extratropical regions

with red arrows, and within the stratospheric extratropical regions with white arrows. In the mesosphere a strong global circulation from the summer pole to the winter pole dominates. This circulation is believed to be driven by gravity waves (not shown in Fig. 3.1). Figure 3.1 also shows that the residual circulation leads to more intense accumulation of O_3 in the extratropical regions during the NH boreal winters 2002-2012.

Therefore, proper representation of the BDC is needed to account for the dependence of the distribution of chemical species on the transport. As the dynamical measurements in the middle atmosphere are rather limited, the alternative conceptual formulations have been developed to explore and understand those processes. One of the concepts is the AoA, which is defined as the mean transit time of an air parcel in the stratosphere since it crossed the tropopause or bottom boundary of the model (Waugh and Hall, 2002; Diallo et al., 2012; Garny et al., 2014). In a model AoA can be calculated from a so-called "clock tracer", i.e. an inert tracer that has a linear or near-linear increase at the surface or in the troposphere (Diallo et al., 2019). Because AoA is independent of tracer chemistry, it is a suitable metric to compare different models (Diallo et al., 2012). AoA can be derived from measurements of trace chemical species, such as sulfur hexafluoride (SF_6). According to Stiller et al. (2008) the AoA retrieved from MIPAS SF_6 has systematic errors that makes the AoA up to 1 year too old between 25-35 km. In the tropical region MIPAS AoA data are higher at all altitudes in comparison with the in situ measurements. Chemistry-Climate Models (CCMs) predict a decrease of stratospheric AoA of the 21^{st} century, indicating an acceleration of the BDC (e.g. Butchart et al., 2010). However, the increase of tropical upwelling does not necessarily imply the acceleration of entire BDC (Bönisch et al., 2011; Diallo et al., 2012). In contrast to model predictions, the balloon-borne measurements of AoA for the period from 1975 to 2005 do not show any evident trends (e.g. Engel et al., 2009, and Fig. 8.3).

3.2 El Niño Southern Oscillation

The dynamics of the Pacific surface water was recognised by Sir Gilbert Walker and his students (Scorer, 1997) as having a significant impact on weather not only in the SH, but in the entire atmosphere and was termed the Southern Oscillation (SO). ENSO is an important climate phenomena, which is linked to variations in the tropical SST, atmospheric temperature, convection, and circulation (Randel et al., 2009, and references therein). ENSO is a striking example of climate variability, which is associated with coupling between the atmosphere and the

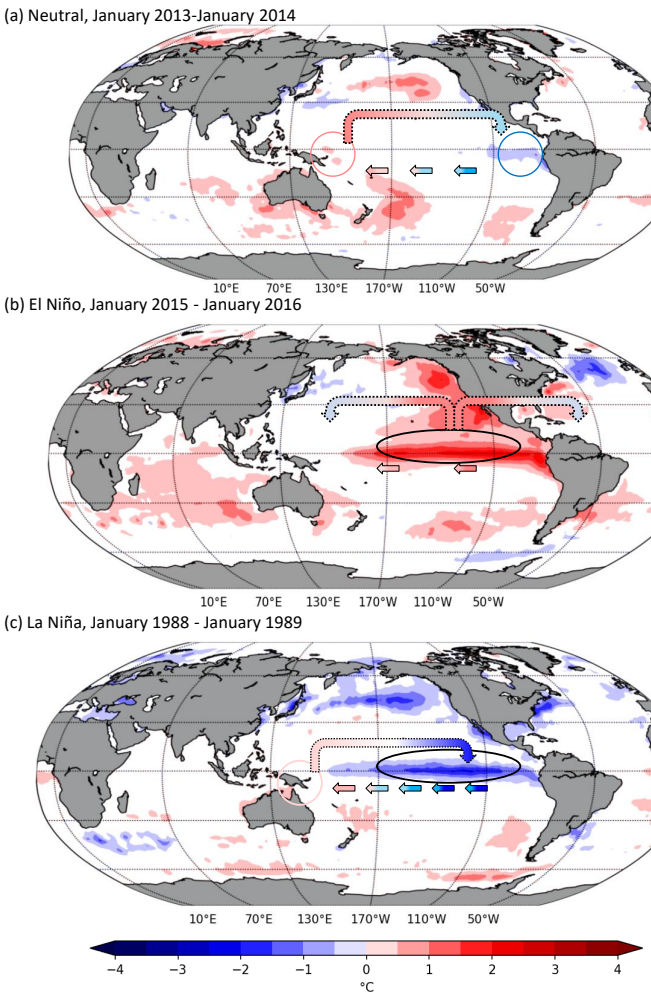

Figure 3.2: The SSTanomalies that indicate three states of the ENSO: a - neutral, b) El Niño, c) La Niña.

ocean (Bjerknes, 1969). An important feature of ENSO is that it occurs at irregular intervals of between 3 and 6 years (see Scorer, 1997).

There are three recognised states of ENSO: neutral, and two opposite El Niño and La Niña. Below, the ENSO mechnanism is illustrated by using the high resolution SST data from the National Oceanic and Atmospheric Administration (NOAA), `https://www.esrl.noaa.gov/psd/data/gridded/data.noaa.oisst.v2.html`. Figure 3.2 shows SST anomalies that correspond to three different states of ENSO: a) neutral, during January 2013-January 2014, b) El Niño, during January 2015-January 2016, and c) La Niña, during January 1988-January 1989.

During neutral ENSO conditions, sea-level pressure is higher on the eastern side of the

Pacific ocean than on the western one, and the easterly surface winds are directed down the pressure gradient along the equator (so-called trade winds, depicted as colourful solid arrows in Fig. 3.2a, see Wallace and Hobbs, 2006). These winds push the warm water near the surface towards the direction of their motion, so it accumulates in the western part of the Pacific (pink circle in Fig. 3.2a). In the eastern Pacific, warm water is replaced by cold water (light blue circle in Fig. 3.2a). Warm water in the western Pacific causes unstable convective weather, i.e. air masses strongly rise, form clouds, and cause precipitation (coloured dotted arrow in Fig. 3.2a) in the west Pacific, and cooler drier air descends in the east Pacific. Such circulation reinforces easterly winds (Wauthy, 1986).

El Niño events are associated with a weakening of the climatological-mean pressure gradient (Wallace and Hobbs, 2006), which leads to the weakening of the easterly trade winds along the equator. The normal temperature differences between the west and east Pacific is then cancelled, as the anomalous ocean warming is observed in the central and eastern Pacific (see Fig. 3.2b). Subsequently, the circulation re-arranges, so the large wind patterns diverge from the central Pacific region towards east and west simultaneously (coloured dotted arrows in Fig. 3.2b). As shown in Fig. 3.2b, an El Niño event during 2015-2016 was one of the strongest on record together with 1982-1983 and 1997-1998 (Blunden and Arndt, 2016), and can be considered as the first extreme El Niño of the 21st century (Santoso et al., 2017).

La Niña events follow El Niño, and are depicted in Fig. 3.2c. In contrast to El Niño, the trade winds are straightening during La Niña (solid arrows in Fig. 3.2c). The warm water (pink circle in 3.2c) is pushed far west and the upwelling of cold waters in the east of the tropical Pacific increases, sometimes approaching central regions of the tropical Pacific.

For this reason, ENSO has a significant impact on the tropospheric circulation in the tropical Pacific. The associated large changes in the tropical lower atmospheric circulation affect water vapor (H_2O), which in turn affects O_3 distribution. The largest changes in O_3 from ENSO are observed near the tropopause, which is a particularly sensitive region of the climate system.

3.3 Quasibiennial oscillation

The QBO is known as an important forcing mechanism of the Earth's climate that largely determines the global dispersion of stratospheric trace constituents (Hommel et al., 2015, and references therein). Although the QBO is a tropical phenomenon, if affects the stratospheric flow from pole to pole by modulating the effects of extratropical waves (Baldwin et al., 2001).

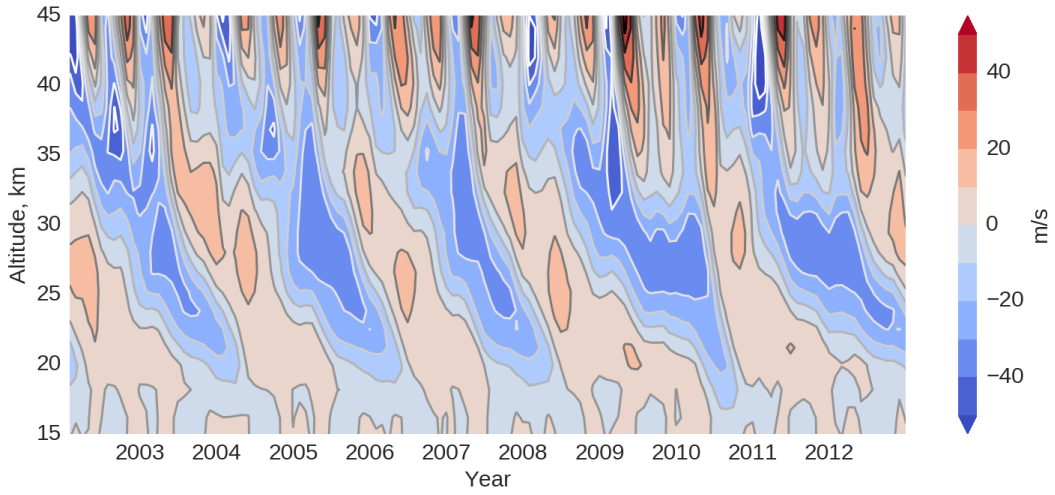

Figure 3.3: Temporal evolution of the monthly mean zonal winds in the equatorial lower and middle stratosphere between 6°S-6°N during 2002-2012 in the TOMCAT model (which is based on ECMWF meteorology). Red represents westerlies, blue represents easterlies.

The QBO is an alternating phenomenon in the lower and middle (below around 35 km altitude) equatorial stratosphere. In a zonal mean framework, zonal winds alternate between easterlies and westerlies with a period ranging from 22 to 34 months and average period of 28 months. The change from easterlies to westerlies (and vice versa) starts in the lower mesosphere and propagates slowly downwards (about 1km/month), where the signature dissipates shortly above the tropopause. Figure 3.3 represents the dynamical aspects of the QBO effect, i.e. the monthly mean zonal winds in the equatorial lower and middle stratosphere between 6°S-6°N during 2002-2012 from the TOMCAT model. Red represents positive (westerly) winds and blue represents negative (easterly) winds. Westerly wind shear zones (i.e. in which westerly winds increase with altitude) descend more regularly and rapidly than easterly wind shear zones. From Fig. 3.3 it is also apparent that the vertical shear is quite strong in the area where one regime is replaced by the other. The amplitude of the QBO signature is nearly the same within altitudes between around 32 and 23 km, and it rapidly decreases below 23 km. The QBO is nearly zonally symmetric phenomenon and causes only very small mean meridional and vertical motions (Andrews et al., 1987; Baldwin et al., 2001; Holton and Hakim, 2012).

There are three major factors that the theoretical model of QBO should explain:

- the approximate biennial periodicity;
- the downward propagation almost without loss of amplitude;

- and the occurrence of zonally symmetric westerlies at the equator.

Among various theories that could cover and explain three factors, mentioned above, only vertical transfer of momentum by equatorial Kelvin waves can explain the origin of QBO (Andrews et al., 1987, and references therein).

There are several reasons for accounting for QBO variations while analysing stratospheric chemical and dynamical processes. Namely, QBO induced meridional circulation modulates the upwelling branch of the BDC. Easterly wind shear is associated with the vertical ascent, enhancing the tropical upwelling. Westerly wind shear is associated with the vertical descent, reducing the tropical upwelling. The QBO affects not only winds and thermal structures, but also the meridional distribution of such chemical compounds as O_3 and NO_2. The NO_2 signal is caused by similar changes in NO_y species, and the O_3 signal corresponds to NO_2 changes, at least in the tropical region of the middle stratosphere (Galytska et al., 2019a).

II

Methodology and data sources

4

Remote-sensing measurements of atmospheric constituents from space

Monitoring of atmospheric constituents, such as O_3, NO_2, BrO, performed by remote sensing instruments on satellite platforms give the potential of near-simultaneous observations at a global scale (Gottwald and Bovensmann, 2010; Holloway and Wayne, 2010). Historically, tropospheric measurements, especially in the boundary layer, relied on localised in-situ methods, while stratospheric composition was predominantly examined by remote sensing techniques. This separation is slowly disappearing nowadays as remote-sensing techniques are further improving and e.g. satellite methods are now adapted to research the tropospheric composition (Holloway and Wayne, 2010). However, satellite measurements of atmospheric composition are tightly linked to ground based observations for validation reasons.

4.1 History of satellite measurements

The number of measurements of atmospheric constituents increased greatly with the development of satellite sensors in the mid-20 century. In particular, July 1957 marked the beginning of the International Geophysical Year (IGY), when scientists from 67 countries from around the world planned to examine different scientific phenomena. The IGY fostered significantly the further development of satellite missions. The first artificial Earth satellite Sputnik 1 was launched in October 1957 by the Union of Soviet Socialist Republics (USSR). A month later, in November 1957 the launch of the second spacecraft Sputnik 2 into the Earth orbit was performed. In February 1958 the United States (US) launched Explorer 1, which made it the third

artificial Earth satellite in the history of space measurements.

Meteorological observations of temperature distribution, winds, and chemical composition of the middle atmosphere began in mid-1960s with the USSR space missions (e.g. Soyuz program) and with the development of National Aeronautics and Space Administration (NASA) Nimbus satellites. The series of Nimbus satellites began with the launch of Nimbus 1 on 28 August 1964. In total there were seven robotic spacecraft launched into near-polar, sun-synchronous orbits over a fourteen-year period. Later, Nimbus 4 was launched carrying the Backscattered Ultraviolet (BUV) instrument to measure global atmospheric O_3 (Heath et al., 1973). Nimbus 7 was carrying an improved and extended version of BUV - Solar Backscatter Ultraviolet (SBUV) instrument and Total Ozone Mapping Spectrometer (TOMS) that provided crucially important information about stratospheric O_3 concentration and its global maps. At that time, NOAA was responsible for SBUV-2 instruments on operational platforms, and NASA operated TOMS instruments on different satellites. The overview of major atmospheric satellite instruments is shown in Fig. 4.1.

Figure 4.1: Atmospheric satellite instruments and missions. Figure taken from: Gottwald and Bovensmann (2010).

Useful occultation measurements (a more detailed technical description is found in Sect. 4.2) began in 1978 with the launch of Stratospheric Aerosol Measurement-II (SAM-II) satellite, followed by Stratospheric Aerosol and Gas Experiment (SAGE) I and II and occultation spectrometer (SFM-2). In 1983 there was the launch of Solar Mesospheric Explorer (SME), aimed to determine O_3 and NO_2 from limb scanning measurements of solar backscattered radiation (see the description of technique in Sect. 4.2). 1991 was another milestone year in atmospheric satellite measurements with the launch of the Upper Atmosphere Research Satellite (UARS, Reber et al., 1993) that carried Microwave Limb Sounder (MLS) and Halogen Occultation Experiment (HALOE) instruments to sound the upper atmosphere and European Remote Sensing satellite (ERS-1), which was the first polar orbiting European Space Agency (ESA) satellite. ERS-1 did not carry any instruments observing chemical constituents of the atmosphere. Therefore in 1995 ESA launched ERS-2, which included Global Ozone Monitoring Experiment (GOME) instrument. GOME measured solar radiation scattered by the Earth's atmosphere and brought Europe much more forward towards measurements of atmospheric composition.

The need for global atmospheric observations is reflected in the number of satellite missions (see Fig. 4.1) that were launched since ERS-2, i.e. NASA's Earth Observing System (EOS) with satellites TERRA, AQUA, and AURA; Japanese Advanced Earth Observing System (ADEOS1/2) and Greenhouse Gases Observing Satellite (GOSAT), the Canadian-Swedish-French collaboration with Odin satellite and the Canadian Space Agency (CSA) SCISAT mission.

In 2002, ESA launched Environmental Satellite (Envisat) with 10 instruments on board, of which SCIAMACHY, MIPAS, and Global Ozone Monitoring by Occultation of Stars (GOMOS) were of major importance in studies of atmospheric composition. SCIAMACHY was a spectrometer that measured in UV-visible-near-infrared (NIR) and required sunlight. MIPAS measured over the complete orbit and operated in the thermal IR range. GOMOS used UV-VIS radiation from the stars in the occultation geometry. Envisat together with European Organisation for the Exploitation of Meteorological Satellites (EUMETSAT) and its series of METOP satellites extended the European data record beyond 2020. In 2006, NASA in collaboration with Centre national d'études spatiales (CNES) of France launched the Cloud-Aerosol Lidar and Infrared Pathfinder Satellite Observations (CALIPSO) satellite, which together with AQUA and AURA belongs to the Afternoon Train (A-Train) satellite constellation.

Nowadays ESA is developing a new family of missions called Sentinels. The most recent, Sentinel-5 Precursor (Sentinel-5P) was launched in October 2017 and is the forerunner of the Sentinel-5 satellite. The aim of Sentinel-5P is to measure atmospheric trace gases and aerosols to reduce data gaps between the Envisat satellite, i.e. SCIAMACHY and Sentinel-5, the launch of which is planned for 2021.

4.2 Satellite measurement techniques

The composition of chemical species in the atmosphere can be derived from satellite instruments, which measure in different viewing geometries. Figure 4.2 shows three different viewing geometries: limb, nadir, and occultation. Within the limb geometry the line of sight (LOS) of the satellite instruments follows a slant path tangentially through the atmosphere and photons originating from the Sun are detected when they are scattered by the atmosphere into the field of view of the instrument (see Fig. 4.2a, so-called limb-scattering). In another, limb emission technique, the concentrations of trace gasses are derived from measurements of the radiation (IR and microwave) emitted by the atmosphere along the line of sight of the instrument (not

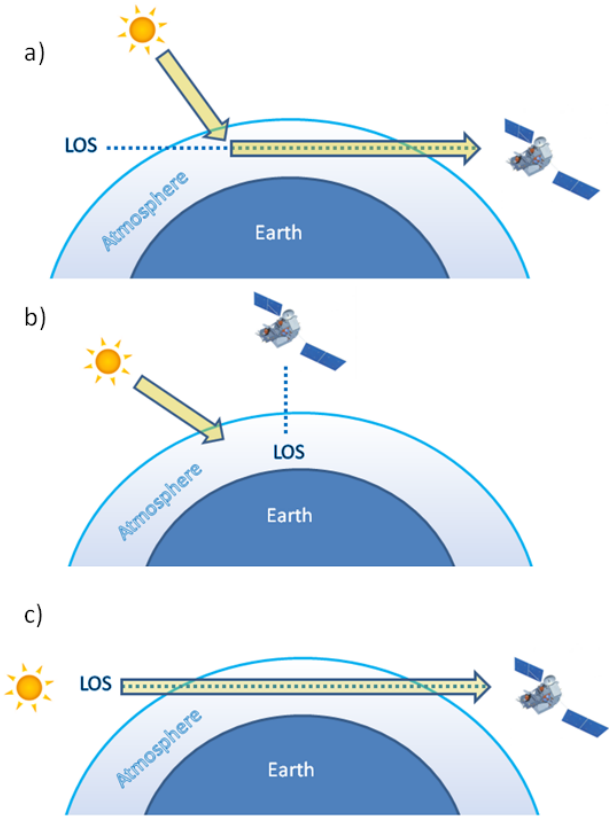

Figure 4.2: The viewing geometries of satellite measurements: (a) limb, (b) nadir, (c) occultation. LOS stands for line of sight of the satellite instrument.

shown here, see Wallace and Hobbs (2006)). Because the Sun is the the major light source, limb measurements are only available during the daytime. Limb measurements have good spatial coverage and are well-established method for the stratospheric research, with the advantage by providing vertically resolved measurements. Among other advantages of limb viewing geometry are 1) the measured signal is not affected by the denser tropospheric signal, 2) the long path of the measured radiation through the atmosphere provides high sensitivity to species with low atmospheric concentrations. As a result, the information on the observed atmospheric state variables can be obtained at a high vertical resolution, while the horizontal resolution is limited.

In the nadir mode (Fig. 4.2b) the LOS of satellite instrument points downwards to the Earth's surface. Such measurements commonly provide the global distribution in form of a vertically integrated quantity, known as "total column". It is also possible to derive limited profile information from nadir measurements (e.g. Singer and Wentworth, 1957; Chance et al.,

1997; Rinsland et al., 2006). Nadir viewing instruments provide full global coverage of the Earth on a daily basis and are also able to observe clouds. In solar occultation mode the instrument points to the Sun, Moon, or stars to measure radiation transmitted through the atmosphere during their rising and/or setting two times per orbit. This limits their temporal and spatial coverage. Figure 4.2c depicts the solar occultation measurement geometry. The Sun is a strong radiance source, which allows highly precise measurements.

In the occultation mode, the altitude-resolved information about atmospheric constituents is obtained by variation of the elevation angle of LOS. The measurement geometry is defined by position of the Sun with respect to that of the satellite instrument.

4.3 Satellite instruments and corresponding data

4.3.1 SCIAMACHY

The SCIAMACHY instrument (Burrows et al., 1995) was launched on board the ESA Envisat satellite, which was operational from March 2002 until April 2012. Envisat was in a near-circular sun-synchronous orbit at an altitude of around 800 km, with the inclination of 98°. SCIAMACHY was a passive imaging spectrometer that comprised eight spectral channels and covered a broad spectral range from 240 to 2400 nm.

SCIAMACHY performed spectroscopic observations of the solar radiation scattered by, and transmitted through, the atmosphere, as well as reflected by the Earth's surface in three viewing geometries: limb, nadir, and occultation. SCIAMACHY scanned the Earth's limb within a tangent height range of about -3 to 92 km (0 to 92 km since October 2010) with about 3.3 km step. The vertical instantaneous field of view of SCIAMACHY was ∼2.6 km, and the horizontal cross-track instantaneous field of view was ∼120 km at the tangent point. The horizontal cross-track resolution was mainly determined by the integration time during the horizontal scan, which was for most of observations 240 km. Global coverage of SCIAMACHY limb measurements was obtained within 6 days at the equator and less elsewhere.

In this research, O_3, NO_2, and BrO data, retrieved from SCIAMACHY measurements, were used. O_3 profiles are scientific retrievals Version 3.5 from IUP Bremen. Monthly mean data of O_3 (Jia et al., 2015) were gridded horizontally into 5° latitude × 15° longitude and vertically into ∼3.3 km altitude bins, in the altitude range from 8.6 to 64.2 km. NO_2 profiles are from both operational and scientific retrievals. NO_2 data from IUP Bremen scientific retrievals are of Version 4.0 and monthly mean NO_2 data (described in Galytska et al., 2019b, manuscript is in preparation for publication in AMT) were gridded similar to O_3 data. NO_2 profiles from ESA operational retrievals are of Version 7.0. BrO profiles are from IUP Bremen scientific retrievals Version 4.2, monthly mean data were gridded similar to both O_3 and NO_2 data.

O_3 and NO_2 data for altitudes 15-40 km, and BrO data for altitudes 18-28 km were used in this research. The zonal monthly mean O_3, NO_2, and BrO values were calculated as arithmetic means, as the errors of single measurements are mostly normally distributed and no additional issues with outliers have been reported. Zonal monthly mean values were typically constructed from hundreds of single measurements. Consequently, it was assumed that the random errors of zonal monthly means could be neglected. The boundaries 60°S-60°N were chosen to circumvent gaps in SCIAMACHY sampling during polar winters.

4.3.2 MIPAS

MIPAS was a high-resolution Fourier Transform Infrared spectrometer that was measuring in the thermal mid-IR region (4.15 μm - 14.6 μm) with the limb-emission observation technique (Carlotti and Magnani, 2009). Measurements performed by MIPAS were separated into two periods. From March 2002 to March 2004 the spectral resolution in MIPAS measurement mode was 0.035 cm^{-1}, which corresponded to an effective spectral resolution of 0.05 cm^{-1} after numerical apodization with the Norton Beer apodization function (e.g. Stiller et al., 2008, and references therein). After the failure of the instrument, i.e. deterioration of the interferometric slides, in March 2004 MIPAS resumed operation in a reduced spectral resolution from 0.025 cm^{-1} and sampling time of 4.5 s to 0.0625 cm^{-1} and reduced sampling time of 1.8s. MIPAS scanned the atmosphere within a tangent height range between 5 km and 160 km with corresponding minimum and maximum steps of 1 and 8 km (Fischer et al., 2008). The vertical field of view of the MIPAS instrument was 3 km deep to achieve a good vertical resolution, but 30 km wide to collect sufficient radiance.

MIPAS O_3 and NO_2 data Version 5R of the scientific retrieval algorithm is a result of the collaboration between Institute of Meteorology and Climate Research at the Karlsruhe Institute of Technology (IMK)-Instituto de Astrofísica de Andalucía (IAA). MIPAS IMK-IAA algorithm is described by von Clarmann et al. (2009) and Funke et al. (2014). MIPAS NO_2 profiles Version 7.03 from operational retrievals from ESA algorithm are described in a documentation available from `https://earth.esa.int/web/sppa/mission-performance/esa-missions/envisat/`. The differences between MIPAS operational and scientific products are described in Wetzel et al. (2007). In our case only the period of January 2005-April 2012 was used in order to avoid additional errors that might have been caused by switching the spectral resolution due to the interferometer mirror slide anomaly. A similar approach was used by Sheese et al. (2016) in the validation of Atmospheric Chemistry Experiment (ACE)-Fourier Transform Spectrometer (FTS) NO_y species.

4.3.3 MLS

MLS is one of the four instruments on board the NASA Aura satellite, which was launched in July 2004. It observes the thermal emission from atmospheric trace gases in the millimetre- and sub-millimetre spectral range, providing their profiles in the upper troposphere, stratosphere, and mesosphere. There is equal numbers of scans in the northern and southern hemisphere,

which are performed continuously. MLS scans the limb of the atmosphere within the tangent height range of about 0 to 95 km. The integration time of the instrument of 1/6s provides radiance measurements every 0.3-0.5 km vertically in the upper troposphere and lower stratosphere (Waters et al., 2006). Every day MLS performs around 3500 measurements over the Earth during day and night (Ziemke et al., 2006). In this study O_3 data Version 4.2 were used (similar to Arosio et al., 2018). Zonal monthly mean values within latitude range 10°S-10°N and the altitude range 30-35 km were used in this study.

4.3.4 SAGE II

The SAGE II instrument (Chu et al., 1989) was an occultation instrument aboard the United States Earth Radiation Budget Satellite (ERBS), launched in 1984. Originally the operation time of the satellite was planned to be two years, however ERBS delivered data until the end of August 2005. SAGE II was a sun-photometer with seven spectral channels (385, 448, 453, 525, 600, 940, and 1020 nm), which vertically scanned the limb of the atmosphere by pointing the Sun during sunrises and sunsets as seen from the spacecraft (fifteen sunrises and fifteen sunsets each day). The measured sunlight was converted into vertical profiles of O_3, NO_2, and aerosols. The SAGE II instrument data covered the whole global longitudinal range and latitudes from 80°N to 80°S. The SAGE II NO_2 profiles Version 7.0 were used in this study. The long operation time of ERBS (21 years) provides an overlap with SCIAMACHY from 2002 to 2005. Table 4.1 summarises all satellite instruments and corresponding data sets used in the study.

Table 4.1: Satellite instruments and corresponding data sets used in this study.

Instrument	Parameter	Retrieval algorithm	Data version	Analysed period
SCIAMACHY	O_3	IUP Bremen	V3.5	2002-2012
	BrO	IUP Bremen	V4.2	
	NO_2	IUP Bremen	V4.0	
		ESA	V7.0	
MIPAS	O_3	IMK-IAA	V5R	2005-2012
	NO_2	IMK-IAA	V5R	2005-2012
		ESA	V7.03	
MLS	O_3	NASA	V 4.2	2004-2012
SAGE II	NO_2	NASA	V7.0	2002-2005

5

Atmospheric models

Atmospheric models are developed to study physical and chemical processes in the global atmosphere and to describe their complex nonlinear interactions and feedbacks (e.g. Trenberth, 1992; Brasseur et al., 1999; Holloway and Wayne, 2010). Primarily these models are used to explain and quantify changes in the atmospheric composition. This is achieved by mathematical formulations of natural laws that apply to atmospheric processes. However, the equations derived from these laws and processes are so complex that they must be solved numerically.

5.1 History of atmospheric modelling

The basic ideas of atmospheric modelling were developed long before computers were constructed, about a century ago (Lynch, 2008). The first steps towards development of numerical models were done in 1901 by American meteorologist Clevend Abbe. He defined the system of mathematical equations that govern the evolution of the atmosphere. Three years later, in 1904 a Norwegian scientist Vilhelm Bjerknes undertook more explicit analysis of the weather forecast. He formulated a simplified hydrodynamical system of equations, which described the simplest moments of fluids motion in the atmosphere. The first prototype of an atmospheric model for weather prediction was introduced by Richardson (1922). He constructed a systematic mathematical method, which involved so many equations that it became impractical to be solved in the pre-computer era. According to Lynch (2008) "Richardson was several decades ahead of his time in what he attempted to do". As clarified by Hack (1992) and Trenberth (1992), the major reasons of Richardson's failure in weather forecast were the lengthy six-hour time step that violated fundamental numerical stability limits, coupled with the general inad-

equacy of observational data in the free atmosphere. However, the methodology proposed by Richardson is essentially that used in weather forecasting nowadays.

During the next 30 years numerous factors fostered the development of atmospheric modelling and science in general. Among those factors were technical progress, in particular development of radiosondes, improvement of observational network, natural and human catastrophes, and socio-political changes (e.g. dependency of military operations on weather forecasts during the Second World War).

Atmospheric modelling received a significant boost with the introduction of the first general-purpose computer, known as Electronic Numerical Integrator and Computer (ENIAC), developed by Hungarian-American scientist John von Neumann. The press proclaimed ENIAC as a "Giant Brain", which fostered the development of weather forecasting.

Further technological development led to more sophisticated modelling approaches, which are currently used for various purposes. Nowadays atmospheric models are used as both, prognostic and diagnostic tools. As prognostic tools, models provide the evaluation of future behaviour and evolution of the atmosphere. However, such simulations should be taken into account only if there is sufficient confidence in the interpretation of their results, which should be analysed with cautioun. As diagnostic tools, models support the information content derived from measurements and help interpret observed variability in the atmosphere.

Among numerous applications of atmospheric models in weather forecasting, climate prediction, they are also used to study transport and chemical mechanisms governing trace gases and aerosols abundances. If numerical treatments of solving chemical processes are incorporated, atmospheric models then simulate the spatial distribution and temporal evolution of chemical compounds in the atmosphere (Brasseur et al., 1999). According to Jacob (1999), the concentrations of chemical compounds in various regions of the atmosphere are controlled by four major processes:

- Emissions. Chemical species are emitted to the atmosphere by two major sources:
  - natural sources of biogenic (e.g. photosynthesis of oxygen) and non-biogenic (e.g. volcanoes, biological decay, forest fires) origin.
  - anthropogenic sources (e.g. industry, fossil fuel combustion, transport, agricultural activities).
- Chemistry. Chemical reactions that lead to production and loss of atmospheric species.

- Transport. Spatial changes in concentrations of chemical species in particular areas of the atmosphere due to the transport by winds.
- Deposition. All material in the atmosphere is eventually deposited back to the Earth's surface. There are two types of deposition:
  - dry deposition, a gravitational sedimentation of atmospheric material, i.e. chemical species during periods without precipitation.
  - wet deposition, a washout of soluble vapour phase and particulate bound chemicals during precipitation.

5.2 Major modelling approaches and model development

There are two major modelling approaches, Lagrangian and Eulerian that have been developed for atmospheric chemistry calculations. In the Lagrangian approach, the model deals with the individual parcel, which follows the atmospheric motion and inside which all the tracers are assumed to be homogeneously mixed. Such models are usually used to study regional pollution, e.g. Hybrid Single Particle Lagrangian Integrated Trajectory Model (HYSPLIT), `https://www.ready.noaa.gov/HYSPLIT.php`. However, sometimes it is more convenient to estimate the changes at a fixed location than for different parcels, which corresponds to the Eulerian approach when the flux of air mass that passes through the fixed location is calculated (Brasseur et al., 1999).

The overall development of atmospheric models is an important process that involves the improvement of a numerical code, validation of modelled results with respect to measurements, and performance of sensitivities studies. Schematic representation of the development and use of an atmospheric model, similar to Goosse (2015) is shown in Fig. 5.1.

5.3 Atmospheric models

Atmospheric models vary greatly in their complexity, requirements of computational power, and applications. One-dimensional (1-D) models are used for interpreting and analysing vertical distributions of chemical species and do not account for horizontal variations (Holloway and Wayne, 2010). Two-dimensional (2-D) latitude-altitude models have often been applied for stratospheric research. The major reason for constructing 2-D models is that on a rotating

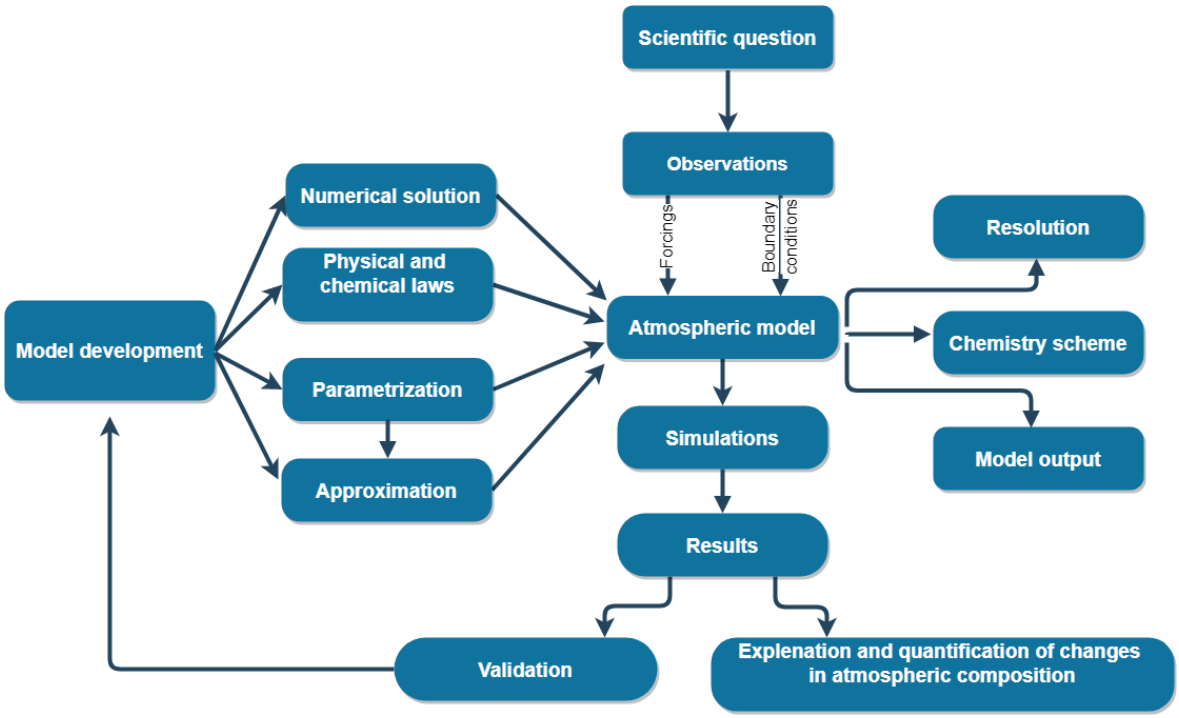

Figure 5.1: Schematic representation of the development and application of an atmospheric model.

planet meteorological compounds are not expected to vary much longitudinally if averaged over several days. Latitudinal gradients in the Earth's atmosphere have a much higher amplitude of variability than longitudinal (Holloway and Wayne, 2010). However, this statement should be taken with caution for lower altitudes, where sources and sinks of trace gases are highly localised and ignoring their longitudinal variations might make models unrealistic. 2-D models are more realistic than 1-D models and are widely used for the research of stratospheric changes. Three-dimensional (3-D) models provide the most realistic representation of the atmosphere, but they are the most computationally expensive. With the application of 3-D models the complete simulation of the radiative-chemical-dynamical behaviour of the atmosphere is achieved the best.

Among all existing 3-D models, the most widely used are:

- General Circulation Models (GCMs). These models were developed to resolve atmospheric dynamics and simulate climate changes. GCMs attempt to account all important properties at the highest affordable resolution. The application of chemistry schemes here becomes unnecessary.

- CTMs. These models represent an offline simulation framework driven by meteorological fields from the reanalysis data (e.g. European Centre for Medium-Range Weather Forecasts (ECMWF) ERA-Interim or ERA-40) or provided by GCMs to force atmospheric transport. These models are applied for the representation of the complex chemical mechanisms.

- CCMs. These models are a result of coupling of GCMs to detailed chemistry schemes and are computationally demanding.

The progress in 3-D modelling is currently rapid because of increase of both programming efficiency and computational power. To further analyse changes in the stratospheric composition two different CTMs (see Sect.5.3.1 and 5.3.2) were applied in this study.

5.3.1 TOMCAT

The TOMCAT model is a global offline 3-D CTM, originally created in 1991/1992 at the Centre National de Recherches Météorologiques (CNRM) in Toulouse, France and first was described by Chipperfield et al. (1993). Early TOMCAT versions used a hybrid σ-p vertical coordinate system. Although the model performed reasonably well, it was not applicable for the stratospheric research. Then Chipperfield et al. (1996) developed new model version and called it SLIMCAT 3-D CTM. SLIMCAT model used isentropic vertical coordinate and the vertical transport was derived from the heating rates. Meanwhile the TOMCAT model was improved for chemistry studies in the troposphere. This way TOMCAT was devoted to tropospheric research and SLIMCAT to stratospheric research. Ongoing technical and scientific developments motivated the original developer of TOMCAT and SLIMCAT models Martyn P. Chipperfield to combine the two CTMs into a single model TOMCAT/SLIMCAT with a flexible vertical coordinate (Chipperfield, 2006), which we used in the current research. For simplicity reason we refer to the model as TOMCAT.

TOMCAT contains a detailed description of the stratospheric chemistry including species in the O_x, HO_x, NO_y, Cl_y and Br_y chemical families. The model includes heterogeneous reactions on sulfate aerosols and polar stratospheric clouds. The model is forced using ECMWF ERA-Interim winds and temperatures (Dee et al., 2011). All simulations were performed at 2.8° $\times$ 2.8° horizontal resolution with 32 σ-p levels ranging from the surface to about 60 km. The surface mixing ratios of long-lived source gases (e.g. CFCs, HCFCs, CH_4, N_2O) were taken from

WMO (2014) scenario A1. The solar cycle was included using time-varying solar flux data (1950-2016, Dhomse et al., 2016) from the Naval Research Laboratory (NRL) solar variability model, referred to as NRLSSI2 (Coddington et al., 2016). Stratospheric sulfate aerosol surface density (SAD) data for 1850-2014 were obtained from `ftp://iacftp.ethz.ch/pub_read/luo/CMIP6/` (Arfeuille et al., 2013; Dhomse et al., 2015).

To help distinguish between the dynamical and chemical effects on stratospheric O_3 and NO_2 (Sect. 10), three different model simulations were performed (see Table 5.1). The control run (CNTL) was spun up from 1977 and integrated until the end of 2012 including all of the processes described above. Sensitivity simulations were initialized from the control run in 2004 and also integrated until the end of 2012. Run fSG was the same as run CNTL but used constant tropospheric mixing ratios of all source gases after 2004. This removes the long-term trends in composition due to source gases changes. Run fDYN was the same as CNTL but used annually repeating meteorology from 2004. All of the simulations included an idealised stratospheric AoA tracer which was forced using a linearly increasing tropospheric boundary condition.

Table 5.1: Details of the TOMCAT simulations performed for the period 2004-2012.

Simulation name	Meteorology	Tropospheric mixing ratios of source gases
CNTL	Varying	Varying
fSG	Varying	Fixed
fDYN	Fixed	Varying

5.3.2 B3DCTM

B3DCTM stands for Bremen 3-D Chemistry-Transport Model. The model is originally based on the TOMCAT model (see Sect. 5.3.1 and Chipperfield, 2006). Since the beginning of the 2000s, it was developed in the IUP, Bremen University, Germany by Sinnhuber et al. (2003). B3DCTM shares numerous similarities with the TOMCAT model, i.e. some physical processes, design, but its development was established separately. B3DCTM was significantly developed and extensively updated by Wieters (2013), who reintegrated a comprehensive chemistry scheme; extended with ion chemistry (Sinnhuber et al., 2012), added a tracer assimilation scheme used for stratospheric O_3 (Kiesewetter et al., 2010). Large improvements were performed by Aschmann et al. (2009, 2011, 2014), who made extensive structural changes to the model,

included convection as additional transport pathway, and documented all provided changes in official manual (Aschmann, 2014). The most recent changes were done by E. Galytska, who updated rate constants and absorption cross-sections in B3DCTM, similar to the TOMCAT model. In collaboration with J. Aschmann and H. Winkler, E. Galytska extended the treatment of the halogen families in the model, i.e. Br_2 and Cl_2, which were unrealistically represented in the absence of illumination.

Similar to TOMCAT, B3DCTM is driven by ECMWF meteorological reanalysis ERA-Interim. All simulations were performed at a spatial resolution of 2.5° lat × 3.75° lon, using 29 isentropic vertical levels, ranging from 335K to 2726K (about 11-55 km). Horizontal transport is calculated from meteorological wind fields, and the vertical transport from ERA-Interim diabatic heating rates based on detrainment rates using the Prather advection scheme (Prather, 1986). All B3DCTM model runs were performed with 15 min time step. In the standard configuration the chemistry scheme of B3DCTM comprises around 59 species and about 180 gas-phase, heterogeneous, and photochemical reactions (see Aschmann, 2014). In current research B3DCTM climatology, similar to Aschmann and Sinnhuber (2013) was applied.

6

Validation of NO_2 profiles

To analyze the spatio-temporal changes of chemical species in the atmosphere, it is crucial to validate the data sets used, i.e. SCIAMACHY scientific products. The new version of aclimb NO_2 V4.0 had not been validated. Therefore, the purpose of this section is to present a detailed methodology of NO_2 profile validation, by comparing SCIAMACHY IUP with retrievals from independent instruments. Namely, NO_2 data sets from limb measurements, i.e. SCIAMACHY ESA V7.0, both MIPAS ESA V7.03 and IMK-IAA V5R profiles, and occultation measurements SAGE II V7.0 were used. The difference of viewing geometries and other technical specifications of the satellite instruments are presented in Table 4.1 in Sect. 4.

At the beginning of the validation procedure, the co-located profiles were identified and additional criteria were applied (further explained in the next section). Thereafter, the co-located profiles were gridded in order to identify regional differences in the compared data sets (see Sect. 6.2). However, if measurements were performed at different local times, i.e. at different SZA, the retrieved NO_2 profiles were first photochemically corrected, i.e. recalculated to similar illumination conditions. The precise description of the photochemical correction of NO_2 profiles is provided in Sect. 6.3. As a final step, the analysis of averaged profiles, their relative difference (RD), and correlation was performed (see Sect. 9)

6.1 Co-location criteria

Within the initial step of SCIAMACHY NO_2 V4.0 validation, the co-located pairs of profiles between SCIAMACHY and other instruments were defined. Those co-locations were found with the software "coincidence_tool" (Dr. Klaus Bramstedt, IUP, Bremen University, per-

sonal communication). It defines co-location pairs using spatio-temporal criteria. The program was applied even for perfect co-locations, i.e. for the comparison of SCIAMACHY IUP and SCIAMACHY ESA NO_2 profiles. In such cases, the co-location radius was set to 60 km and the time difference was 3.6 seconds to find identical profiles. For the comparison of SCIAMACHY IUP and MIPAS (both IMK-IAA and ESA) data the co-location radius was set to 300 km and 3 hours. For SCIAMACHY IUP and SAGE II comparison, the spatial difference was set to 500 km and temporal to 8 hours.

If several SCIAMACHY profiles were co-located with a profile from another instrument (e.g. MIPAS, SAGE II), all profiles were used. In contrast, if several profiles from another instrument were co-located with the same SCIAMACHY profile, only the one with the smallest spatial distance was selected. Furthermore, two co-located profiles can have large natural differences if one profile is inside and the other is outside the polar vortex. Therefore, an additional criterion for co-location was that both profiles have similar potential vorticity (PV) values, and are thus both either inside or outside the polar vortex. The modified potential vorticity (MPV) was calculated from ECMWF ERA-Interim reanalysis data for all profiles which were located polewards of 35° latitude. Profiles, for which MPV was between 30 and 40 potential vorticity units (PVU), were not taken into account for the analysis as these could not clearly be assigned being inside or outside the polar vortex. If the MPV differed by more than 3 PVU between two profiles, they were also excluded to prevent the analysis of different air masses.

6.2 Data gridding

After the identification of co-located pairs, all profiles were gridded to seven latitudinal bands. It was done to identify possible meridional differences in NO_2 profiles between the compared data sets. All co-located profiles were distributed between the following latitudinal bands:

- Tropics (20°S-20°N)
- Middle latitudes I NH (20-40°N)
- Middle latitudes I SH (20-40°S)
- Middle latitudes II NH (40-60°N)
- Middle latitudes II SH (40-60°S)

- High latitudes NH (60-80°N)
- High latitudes SH (60-80°S)

If co-located NO_2 profiles were measured at similar illumination conditions, then several diagnostics were calculated at each altitude, e.g. mean RD, standard deviation (STD) of RD, correlation, and time-series comparison (see Sect. 6.4). If the compared profiles had a relatively large spatio-temporal difference (like between SCIAMACHY and SAGE II), and thus were measured at different illumination conditions, then those profiles had to be photochemically corrected.

6.3 Procedure for the photochemical correction

As discussed in Sect. 2.2.2, NO_2 belongs to photochemically active species and therefore has a pronounced diurnal variation. This makes comparisons of profiles measured at different local times difficult (e.g. Bauer et al., 2012). For the validation, one profile should be scaled to the illumination conditions of the other profile. To perform such a scaling, a photochemical model has to be applied. In this section, different modelling approaches and techniques are compared in order to select the most appropriate method. A detailed description of the photochemical correction is also provided. In this study, NO_2 profiles from occultation measurements, i.e. from SAGE II, were scaled to the SZA of SCIAMACHY measurements. To do so, for each altitude z the scaling factor F is calculated as follows:

$$F = \frac{MOD_{NO_2}(\theta_{limb}, z)}{MOD_{NO_2}(\theta_{occ}, z)} \tag{6.1}$$

Here MOD_{NO_2} is the modelled NO_2 profile, at SZA (θ), where θ_{limb} is the SZA of limb measurements and θ_{occ} is the SZA of occultation measurements, i.e. 90°. NO_2 profiles from occultation measurements were scaled to the SZA of limb measurements by multiplying occultation NO_2 profiles by the model-based correction factor F:

$$NO_2(\theta, z) = NO_2(\theta_{occ}, z) \times F \tag{6.2}$$

In the following subsections the analysis of different methods of NO_2 photochemical correction is provided.

6.3.1 Testing modelling approaches

6.3.1.1 Pratmo model

The photochemical box model Pratmo (Prather, 1992; McLinden et al., 2000) developed at the University of California, is widely used for the validation of limb and occultation measurements (e.g. Sheese et al., 2016). In this research the C++ version of the model was applied, which was developed at the University of Saskatchewan (`http://odin-osiris.usask.ca/`). Two different model experiments were performed to reproduce and investigate NO_2 diurnal variation for selected days: 1) using simplified meteorological fields introduced to the model as look-up tables, and 2) actual profiles of temperature and pressure from ECMWF and of O_3 measured by SCIAMACHY. Figure 6.1 shows the results of the Pratmo simulations. The relative difference between the two approaches varies from -7 to 2% in the altitude range 20-45 km. It is expected that the Pratmo model simulation of NO_2 diurnal variation improves when O_3 data from SCIAMACHY measurements used as input.

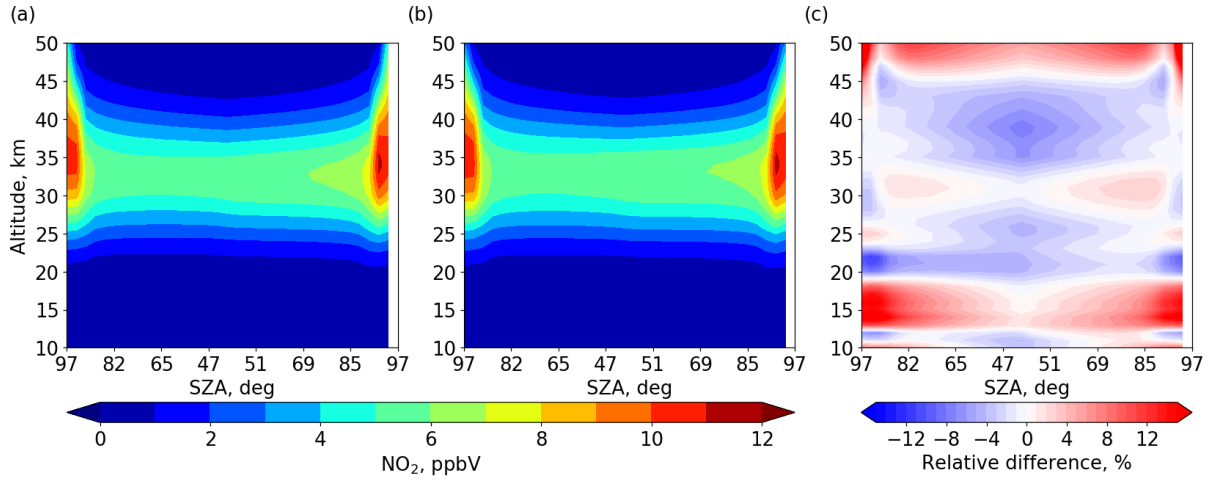

Figure 6.1: Comparison of NO_2 diurnal variation in the Pratmo model (a) with simplified climatology, (b) with ECMWF meteorology and SCIAMACHY O_3 and (c) their relative difference, at middle latitudes NH on 11 July 2004.

Disadvantages. The applied C++ version of the Pratmo model is developed and operated on a Windows system. Application of the model thus requires a transfer of all data sets to Windows machines from the data depository hosted in a Linux cluster, which is time consuming. Another possibility would be to use the original version of the Pratmo model, developed in Fortran, which is currently not available.

6.3.1.2 Pratmo look-up tables

The complete diurnal cycle of NO_2 is modelled for 3 days in each month (1st, 11th and 21st) by the Pratmo model at 2.5° latitude resolution within the altitude range from 8 to 56 km. Modelled information is then collected to look-up tables. The same method was applied by Brohede et al. (2007) for the validation of Odin/OSIRIS NO_2. According to Bracher et al. (2005) and Bauer et al. (2012), the uncertainty of the photochemical correction using look-up tables is approximately 20%. To further reduce the uncertainties introduced by the look-up tables, the application of a more sophisticated method is required.

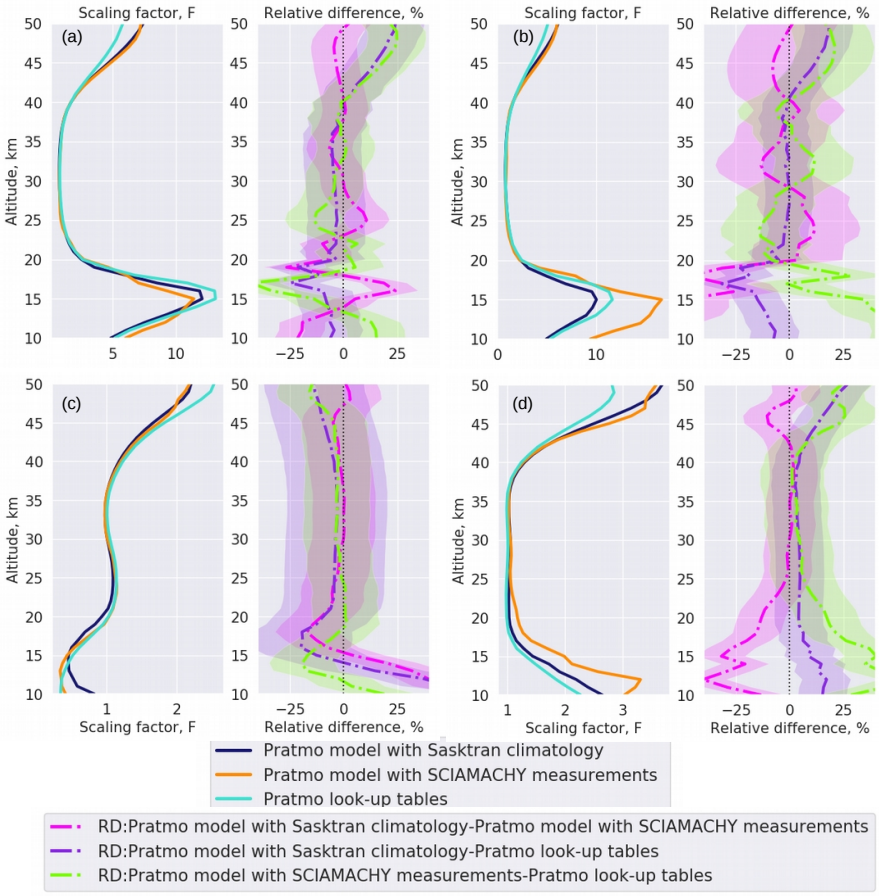

Figure 6.2: Comparison of scaling factors and their relative differences for NO_2 with the Pratmo model driven by simplified climatology (blue), by meteorology from ECMWF and SCIAMACHY O_3 (yellow) and look-up tables (turquoise) for (a) 11 January 2004, (b) 11 April 2004, (c) 11 July 2004, (d) 11 October 2004.

Figure 6.2 shows NO_2 correction factors, calculated via Eq. (6.1), from simulations with the Pratmo model driven by simplified climatology, i.e. look-up tables of temperature and pressure distribution (blue), with the Pratmo model driven by meteorology from ECMWF and SCIAMACHY O_3 (orange), and from look-up tables (turquoise). The relative differences and their standard deviations (see Sect. 6.4) are provided as dash-dotted lines. The comparison was performed for 4 different dates at different locations: (a) 11 January 2004, tropics, scaling from 90° to 35° SZA, (b) 11 April 2004, tropics, scaling from 90° to 45° SZA, (c) 11 July 2004, SH middle latitudes, scaling from 90° to 84° SZA, and (d) 11 October 2004, NH middle latitudes, scaling from 90° to 70° SZA. The largest differences in correction factors from different approaches occur mostly below 20 km and above 45 km. Between 20-25 km the relative difference reduces significantly, from ± 25% to ± 5%. And between 25 and 40 km the agreement between different approaches is very good, as the RD does not exceed ± 5%.

Disadvantages. The rather coarse temporal resolution of provided NO_2 conversion profiles (3 days per month) introduce additional uncertainties. Also, the latitudinal resolution of 2.5° is rather low to match measurements and model data.

6.3.1.3 B3DCTM

To test the performance of B3DCTM for the NO_2 photochemical correction, the model runs for specific days with 15-minute output were done. To improve the photolysis in B3DCTM for a better estimation of NO_2 variations at sunrise and sunset, the original scheme of Meier et al. (1982) was replaced by SCIATRAN radiative transfer model (RTM) actinic fluxes. More details of SCIATRAN RTM can be found at: `http://iup.uni-beremen.de/sciatran` and in Rozanov et al. (2014). Figure 6.3 presents the comparison of NO_2 diurnal variations from the Pratmo model with SCIAMACHY O_3 fields (yellow), from B3DCTM with standard Meier scheme (purple) and with implemented SCIATRAN actinic fluxes (light blue) for 11 January 2004, SH middle latitudes, at 35 km altitude. There are significant differences around times of local sunrise and sunset, especially between B3DCTM with standard Meier scheme and the Pratmo model. Such differences can be explained by the rather coarse temporal resolution of B3DCTM during sunrise and sunset. However, the diurnal variation of NO_2 from B3DCTM with SCIATRAN actinic fluxes is in good agreement with the Pratmo model, but B3DCTM shows a higher night-time content of NO_2 than Pratmo. A further improvement of B3DCTM is needed by reducing the time sampling. A higher temporal sampling can be achieved by also using a 1-D model.

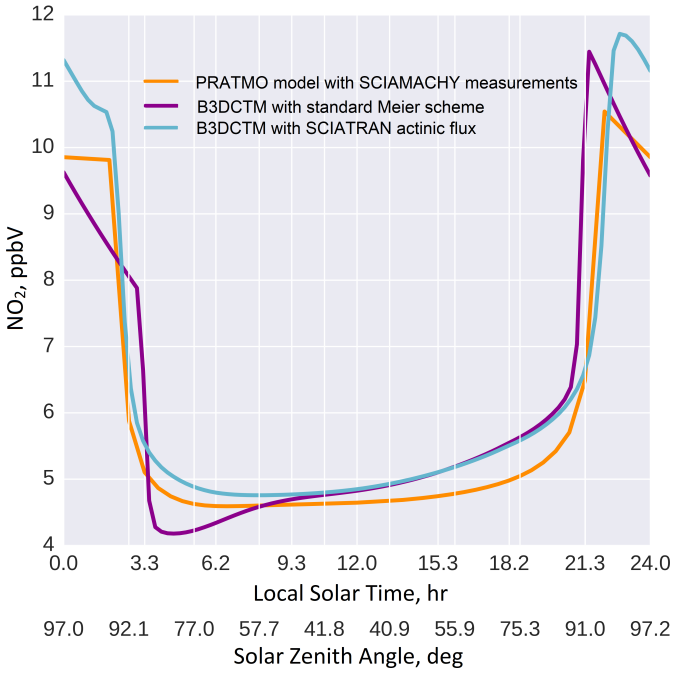

Figure 6.3: NO_2 diurnal variations from the PRATMO model (orange), from B3DCTM with standard Meier scheme (purple) and from B3DCTM with SCIATRAN actinic fluxes (blue) for 11 January 2004, SH middle latitudes at 35 km altitude.

Disadvantages. The coarse time sampling in B3DCTM during sunrise and sunset reduces the accuracy of the correction factor.

6.3.1.4 TOMCAT 3-D and 1-D models

To scale NO_2 profiles measured at local sunrise or sunset to the SZA of limb measurements and to compare co-located occultation-limb profiles the TOMCAT and related to it 1-D stratospheric model were tested. TOMCAT 3-D model is run for all available occultation measurements. The output of TOMCAT is then used to initialise the 1-D model, which reproduces NO_2 diurnal cycle with the time step of 1 minute. This is one of the advantages of TOMCAT application in contrast to previously described methods. The example of NO_2 diurnal variation from TOMCAT and related 1-D model was previously shown in Fig. 2.5 in Sect. 2.2.2 for 1 January 2005 at four different altitudes.

Bracher et al. (2005) has noted that photochemical correction models are expected to run for several days, due to the spin-up effect. The main purpose of model spin-up is to reduce

the impact of initial conditions on the model's output (Athanasopoulou et al., 2013). For this case, the spin-up effect was explicitly investigated in the 1-D model. The drift between NO_2 profiles was analysed for 1 January 2005 from the first to the second day and is shown in Fig. 6.4. Solid lines in Fig. 6.4 show first simulated day, dotted lines - second simulated day. It is apparent that the differences between profiles are negligible. Therefore, it is sufficient to run the 1-D model for one day only.

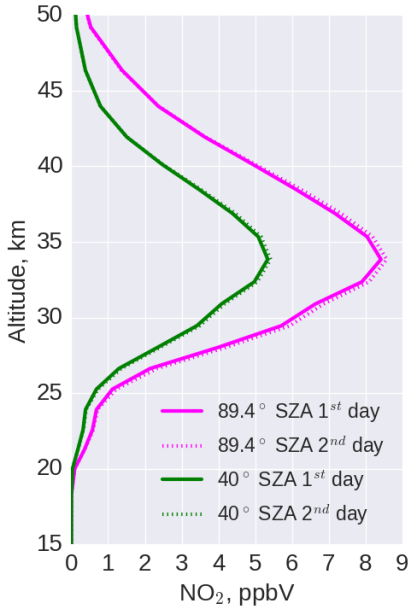

Figure 6.4: NO_2 profiles for 0.5° S, 156.4° E from the TOMCAT-related 1-D model simulated for 1 January 2005 at 89.4° SZA and at 40° SZA.

It can be concluded that the application of TOMCAT and related 1-D model is a preferred choice for the validation of limb NO_2 profiles. Clear advantage of suggested method is based on possibility of calculating scaling factor for time of each particular co-located profile, which is not provided by e.g. Pratmo look-up tables. The results of this method are further shown in Section 9.2.

6.3.2 Schematic representation of photochemical correction

The schematic representation of the photochemical correction of SAGE II NO_2 profiles to the illumination conditions of SCIAMACHY limb measurements is shown in Fig. 6.5. After co-location pairs between SAGE II and SCIAMACHY NO_2 profiles are defined, the 3-D TOMCAT model is sampled for all available SAGE II measurements. Namely, for the period September

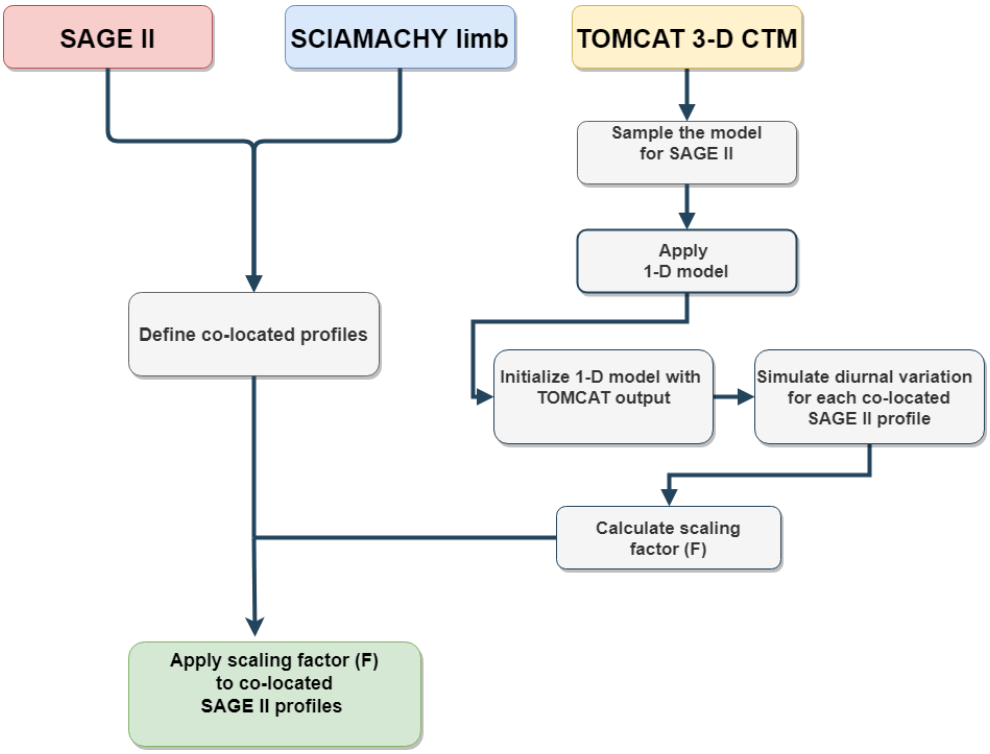

Figure 6.5: Schematic representation of the photochemical correction scheme for NO_2 profiles.

2002-September 2005 there are 13418 SAGE II measurements. In the next step, the 1-D model is initialised with the output from TOMCAT CTM and is run to reproduce NO_2 diurnal variation for each occultation measurement with the time step of 1 minute. The scaling factor F is then calculated by Eq. (6.1). Within the last step, factor F is applied to co-located SAGE II measurements to scale them to the illumination conditions, i.e. to SZA of SCIAMACHY limb measurements by Eq. (6.2).

6.4 Applied diagnostics for NO_2 validation

To compare co-located NO_2 profiles from different instruments, monthly mean NO_2 number densities were calculated. All co-located profiles were linearly interpolated to SCIAMACHY IUP vertical grid. For both cases, when photochemical correction was applied for NO_2 profiles, i.e. SCIAMACHY limb vs. SAGE II or not, e.g. SCIAMACHY vs. MIPAS, several diagnostics were calculated at each altitude: mean NO_2 profiles and their STDs, RDs and STD of RDs, correlation. The RD and STD of RD were calculated as described in Dupuy et al. (2009) and

Bauer et al. (2012). The correlation was calculated as described in Sheese et al. (2016). Also, seasonal changes were evaluated by analysing monthly mean time series and their RD. For four selected altitudes (22, 28, 34, and 38 km) the comparison was done for the available co-located times (2002-2012 for SCIAMACHY IUP - SCIAMACHY ESA, 2005-2012 for SCIAMACHY IUP - MIPAS IMK-IAA, SCIAMACHY IUP - MIPAS ESA, and 2002-2005 SCIAMACHY IUP - SAGE II) and results are shown as line plots. See Section 9 for details and results.

7

Multivariate linear regression

To assess the temporal evolution of stratospheric chemical compounds in this research the multiple linear regression (MLR) model was applied to SCIAMACHY and TOMCAT time series for the period January 2004-April 2012. The MLR was performed by ordinary least squares (OLS), which takes into account the autocorrelation of the noise, which is needed to transform the noise from correlated to uncorrelated (white). After such transformation, the OLS is applied to the final results, similar to Tiao et al. (1990); Weatherhead et al. (1998). Equation (7.1) represents the MLR model:

$$X_t = Linear(t) + Seasonal(t) + QBO(t) + ENSO(t) + SC(t), \tag{7.1}$$

where X_t is a general term for the analysed time series. Monthly mean time series with the time step of 1 month are considered in the following analysis. t stands for the time in months, which varies from 1 to 100, where 1 corresponds to January 2004 and 100 to April 2012. The time series X_t is approximated by MLR. Apart from linear terms $Linear(t)$, the MLR accounts for periodic variations, i.e. annual and semi-annual oscillations $Seasonal(t)$, QBO equatorial winds $QBO(t)$, ENSO - $ENSO(t)$, and solar cycle $SC(t)$. The 1σ value, which is defined by a covariance matrix of the regression coefficients, was used as the approximated uncertainty of the observed changes. The significance of the observed changes at the 95% confidence level is met if the absolute ratio between the trend and its uncertainty is larger than 2. The remaining part of time series X_t, which is not approximated by variables in MLR model, can be accounted for as noise.

The linear term $Linear(t)$ of MLR is given by:

$$Linear(t) = \mu + \omega t, \tag{7.2}$$

where μ is intercept of a linear fit of regression analysis and ω is its gradient. The gradient value stands for estimated linear change or trend. Considering monthly time series, ω represents the slope per month. Similar to Gebhardt (2014) the percentage slope per decade ($120 \times \omega$) is calculated relative to the mean value of the whole time series. Below, linear changes of chemical species are provided in the relative units of % per decade. Changes of AoA are shown in absolute values, i.e. years per decade.

Seasonal variations $Seasonal(t)$ represent harmonics with annual and semi-annual periods (j=1 and j=2 accordingly) as follows:

$$Seasonal(t) = \sum_{j=1}^{2} (\beta_{1j} sin(\frac{2\pi jt}{12}) + \beta_{2j} cos(\frac{2\pi jt}{12})), \tag{7.3}$$

where $\beta_{11}...\beta_{22}$ are the fitting parameters. The combination of sin and cos modulations adjusts the model to any phase of the annual and semi-annual variations. In the high latitudes of 50-60°N between 15-26 km the seasonal term is replaced by the cumulative eddy heat flux. ERA-Interim eddy heat flux at 50 hPa integrated from 45°N to 75°N with the time lag of 2 months was used in this study. The eddy heat flux was used as a proxy for the transport of stratospheric species due to variations in planetary wave forcing (Dhomse et al., 2006; Weber et al., 2011).

QBO represents quasi-periodic oscillations in equatorial zonal wind, alternating between easterlies and westerlies in the stratosphere every 2-3 years (for more details see Sect. 3.3). To fit the QBO signature into the MLR model, the 10 and 30 hPa equatorial winds were taken into account:

$$QBO(t) = aQBO_{10}(t) + bQBO_{30}(t), \tag{7.4}$$

where a and b stand for the fitting parameters, $QBO_{10}(t)$ and $QBO_{30}(t)$ are the equatorial winds at 10 and 30 hPa respectively (`http://www.geo.fu-berlin.de/en/met/ag/strat/produkte/qbo/index.html`). Monthly time series of $QBO_{10}(t)$ and $QBO_{30}(t)$ were smoothed by a 4-month running average.

ENSO is a climate phenomena, which is associated with the coupling between the atmosphere and the ocean (see Sect. 3.2), which affects the atmospheric circulation, and therefore its chemical composition. In the current research the anomalies of the Nino 3.4 index serve as the ENSO proxy for the MLR model. These anomalies are available from `http:`

//www.cpc.ncep.noaa.gov/data/indices/.

$$ENSO(t) = cN_{3.4}(t), \tag{7.5}$$

where c is a fitting parameter, $N_{3.4}$ - Nino 3.4 index. In the regression model ENSO is accounted for within the latitude band 20°S-20°N and between 15-25 km altitude with a time lag of 2 months.

The solar cycle of 11 years leads to pronounced variations of the solar radiation in the UV spectral range, therefore the impact on stratospheric species, i.e. O_3 is also expected (e.g. Gray et al., 2010). The solar cycle term is represented by the multi-instrument monthly mean Mg II index from GOME, SCIAMACHY, and GOME-2 (available from `http://www.iup.uni-bremen.de/gome/solar/MgII_composite.dat` Weber et al., 2013).

$$SC(t) = dMgII(t), \tag{7.6}$$

where d is a fitting parameter. The results of MLR with and without the solar cycle term are very similar. Therefore, results from MLR without a solar cycle term are shown in the current research.

III

Results

8

Comparison of the model data and measurements from satellite instruments

8.1 Age of Air

The representation of variability in stratospheric transport, i.e. the BDC, is described in the models by using Age of Air (AoA), which is defined as the mean elapsed time for an air parcel since it entered the stratosphere (e.g. Waugh and Hall, 2002; Diallo et al., 2012, 2019, and Sect. 3.1). AoA is not influenced by chemistry, that is why its distribution as a function of latitude and altitude is commonly used to visualize the strength, variability, and temporal changes of the BDC. However, another important application of AoA is to compare and evaluate various models (Eyring et al., 2006). AoA can be estimated from measurements of chemical species, which are well-mixed in the troposphere, nearly passive in the stratosphere, and trends of which are well-understood. Recent investigations have focused on retrieving AoA from carbon dioxide (CO_2) and SF_6. They are measured during aircraft campaigns, or derived from balloon-borne and satellite measurements. Retrieved data are usually used to compare modelled and observed AoA (e.g. Diallo et al., 2012). In the models, e.g. TOMCAT and B3DCTM, AoA is often calculated as the response to linearly increasing tropospheric boundary conditions. According to Waugh and Hall (2002) "in steady state the whole atmosphere is increasing at the same rate, and the mean age is the lag time at stratospheric points from the troposphere". In the following, model simulations were performed for the period 1989-2012 and the 8-year spin-up period was

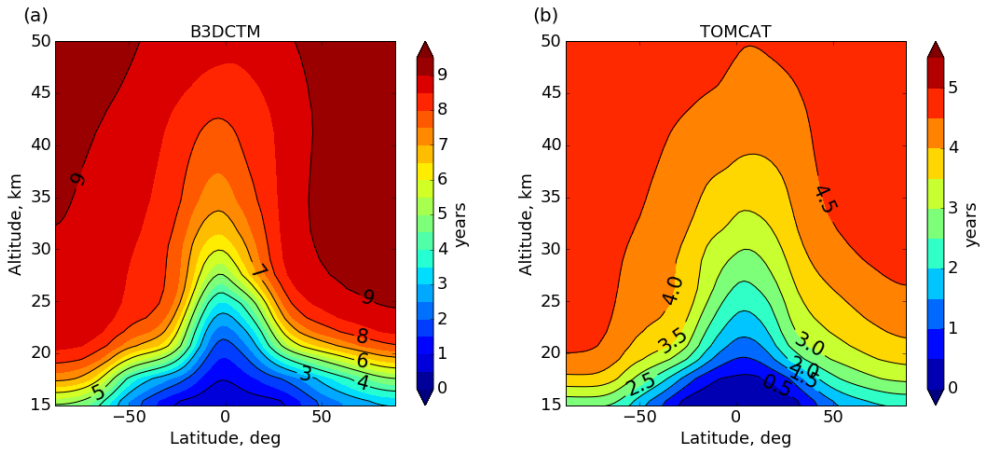

Figure 8.1: Latitude-altitude zonally averaged AoA from (a) B3DCTM and (b) TOMCAT during the period January 2004-April 2012. Note different colour scale.

considered in the analysis. As mentioned in Sect. 6.3.1.4, the spin-up of the model is performed to minimise the impact of the initial conditions (Athanasopoulou et al., 2013), which were set in the model experiment. Within the spin-up period the model reaches a state of statistical equilibrium under the applied initial and boundary conditions. For example, Feng et al. (2005) allowed for a 10-year spin-up period for the TOMCAT model while analysing Arctic ozone loss.

Figure 8.1 shows zonally averaged AoA as a function of latitude and altitude for the period January 2004-April 2012 from the (a) B3DCTM and (b) TOMCAT models. AoA is lowest in the tropical UTLS region and increases with altitude and latitude. This distribution of AoA is determined by the BDC. The smallest values of AoA indicate the regions of intense tropical upwelling. In contrast, the largest AoA values refer to a longer residence time in the atmosphere, hence indicating slow transport, mainly occurring in the polar stratospheric regions. Although both models in Fig. 8.1 agree on the shape of latitudinal-altitudinal AoA distribution, the B3DCTM model (panel a) produces much higher values of the AoA in comparison with the TOMCAT model (panel b). In NH polar regions B3DCTM shows much older (almost double) AoA, compared to TOMCAT. As described in Sect. 3.1, at this time of year the SH is much more quiescent in comparison with the NH; therefore higher AoA values are expected in the high latitudes of the SH, as seen in the TOMCAT model (panel b). To further improve the understanding of CTM-simulated AoA, in the following the model results are compared to the satellite observations.

The zonal mean AoA for the period 2002-2012 from measurements and model simulations

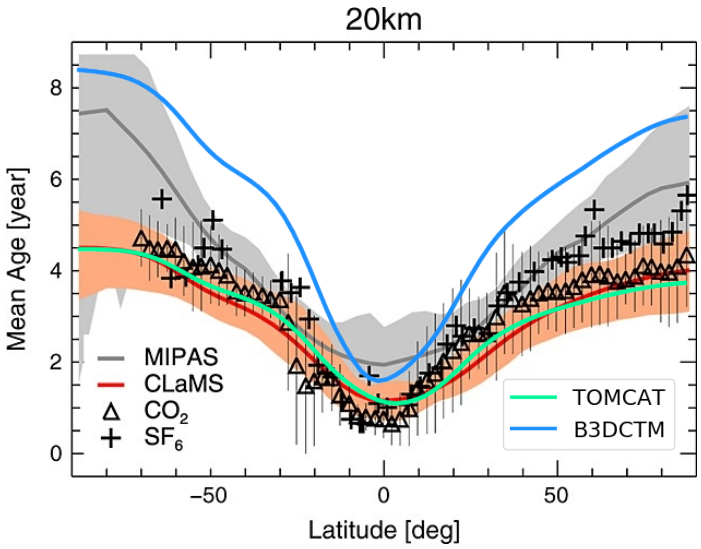

Figure 8.2: Zonal mean AoA for 2002-2012 at 20 km from the CLaMS model (red), MIPAS (gray), and the in situ observations of CO_2 and SF_6 (symbols), taken from: Ploeger et al. (2015, Fig. A1). B3DCTM (blue) and TOMCAT (green) are overlaid for the identical time period and altitude.

at an altitude of around 20 km is shown in Fig. 8.2. It was taken from Ploeger et al. (2015, Fig. A1), where the red line indicates the Chemical Lagrangian Model of the Stratosphere (CLaMS) model, the gray line indicates the MIPAS measurements, and the shaded areas of corresponding colours depict the monthly mean values. The symbols depict the in situ observations of CO_2 and SF_6, and the corresponding error bars indicate the range between minimum and maximum in situ observations. The agreement of the CLaMS model and the in situ measurements is very good. The MIPAS observations of AoA, which are based on SF_6, show much higher values in comparison with the in situ measurements and the CLaMS model, most likely due to the mesospheric loss of SF_6 (Haenel et al., 2015; Kovács et al., 2017). At middle latitudes, in particular in the NH, both the in situ and the satellite measurements are in good agreement. In the tropical region, MIPAS shows larger AoA in comparison with in the situ measurements and the CLaMS model. In addition, the zonal mean AoA for the identical period for an altitude of 20 km from the B3DCTM (blue) and TOMCAT (green) models were overplotted on the original figure A1 Ploeger et al. (2015). TOMCAT agrees well with the in situ measurements and the CLaMS model. B3DCTM corresponds better to the MIPAS satellite measurements; however, the model still significantly overestimates AoA at high latitudes.

8. COMPARISON OF THE MODEL DATA AND MEASUREMENTS FROM SATELLITE INSTRUMENTS

To further test the performance of the applied CTMs, the evolution of AoA was compared with measurements performed by Engel et al. (2009). They derived AoA from balloon-borne measurements of SF_6 and CO_2 mixing ratios over a 30-year period (from 1975 to 2005) at NH mid-latitudes between 32-51°N. Figure 8.3 shows AoA as a function of time based on measurements (panel a, taken from Engel et al. (2009)) and models (panel b - B3DCTM, panel c - TOMCAT). Engel et al. (2009) concluded that at the 2σ confidence level the AoA trend is not statistically different from zero, although at 1σ the long-term positive trend is significant. From corresponding model estimates for the shorter period 2002-2012 of the SCIAMACHY lifetime (Fig. 8.3b and c), B3DCTM shows a more pronounced positive trend whereas TOMCAT agrees better with Engel et al. (2009) (Fig. 8.3a).

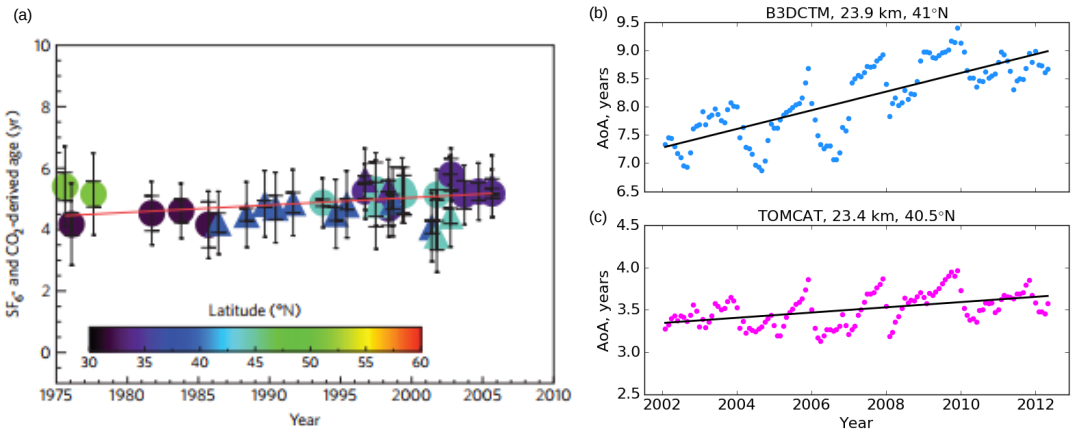

Figure 8.3: Evolution of AoA a) derived from the SF_6 (circles) and CO_2 (triangles) measurements during 1975-2007. Figure taken from: (Engel et al., 2009); b) from B3DCTM and c) TOMCAT models during 2002-2012 at around 24 km altitude and 40°N.

The intercomparison of CTMs and measurements has shown that 1) B3DCTM overestimates AoA in comparison with the TOMCAT model, however it agrees well with retrieved AoA from MIPAS SF_6 measurements; 2) due to uncertainty in the mesospheric loss of SF_6, AoA retrieved from MIPAS shows much older air than in situ observations; 3) AoA from TOMCAT model agrees well with results of the in situ observations (Engel et al., 2009) and the CLaMS model (Ploeger et al., 2015).

8.2 Trace species comparison between models

The comparison of climatologies produced by the B3DCTM and TOMCAT models was performed to investigate whether technical changes in the source code of the B3DCTM for the last 15 years (see Sect. 5.3.2) affected its performance in simulating the global-scale tracer transport. This was done by analysing O_3, NO_2, and N_2O distributions in the stratosphere, which are the focus of the current research.

Figure 8.4 shows zonally averaged distributions of O_3 (a-c), NO_2 (d-f), and N_2O (g-i) in the stratosphere as functions of latitude and altitude from the B3DCTM and TOMCAT models and their RD during the 22-year period 1990-2011. The RD between two models was calculated as follows:

$$RD = \frac{X_{vmr}B3DCTM - X_{vmr}TOMCAT}{X_{ref}} \times 100, \tag{8.1}$$

where X stands for the trace gas, i.e. O_3, NO_2, or N_2O and X_{ref} was calculated as:

$$X_{ref} = (X_{vmr}B3DCTM + X_{vmr}TOMCAT) \times 0.5 \tag{8.2}$$

The distribution of O_3 (Fig. 8.4a-c) between B3DCTM and TOMCAT agrees well in the tropics above 10 hPa (around 30 km altitude) with a RD of below $\pm$ 5%. At high and middle latitudes of both hemispheres B3DCTM produces higher values of O_3 by around 10-20% in comparison to the TOMCAT model. In the tropical and subtropical regions at around 100 hPa ($\sim$16 km), B3DCTM shows significantly smaller amounts of O_3. The comparison of NO_2 (Fig. 8.4d-f) between models shows lower values from B3DCTM in the tropical and at middle latitudes at 10 hPa (10-20%) and higher values of around 30% at 100 hPa at high latitudes of both hemispheres. The amount of stratospheric N_2O is significantly lower in B3DCTM than in the TOMCAT model (see Fig. 8.4g-i). At higher altitudes of around 1 hPa (above 45 km) B3DCTM shows around 15% higher N_2O content in comparison with TOMCAT model. Only in the tropical lower stratosphere are both models in agreement.

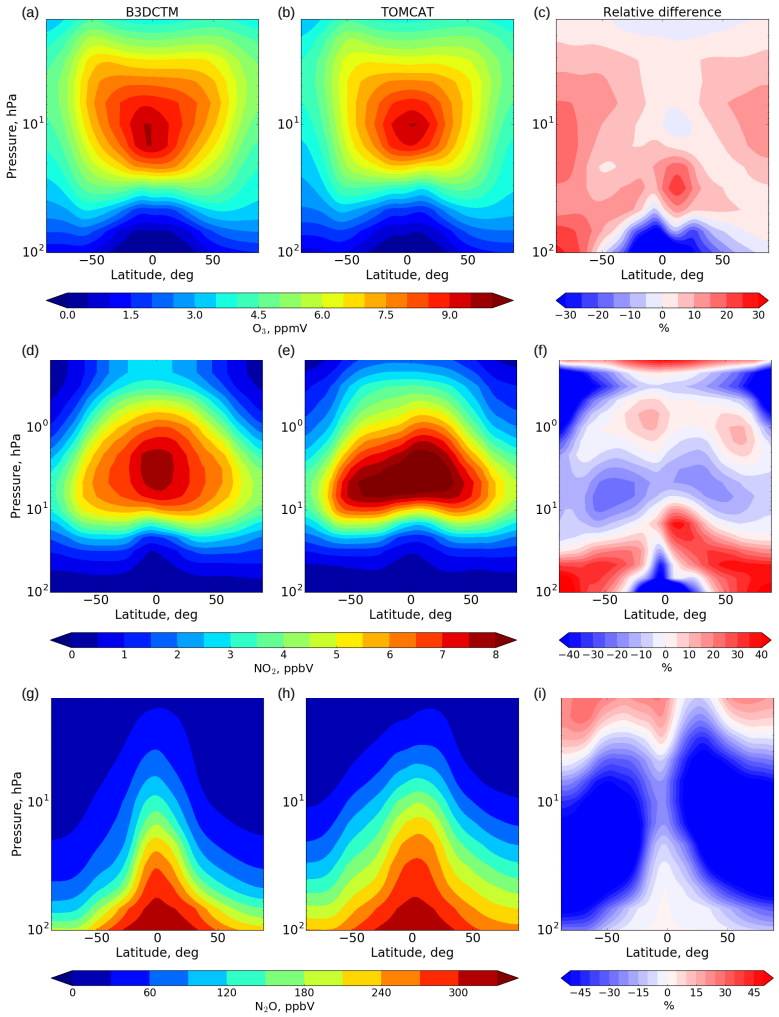

Figure 8.4: Latitude-altitude zonally averaged (a-c) O_3, (d-f) NO_2, and (g-i) N_2O in the stratosphere from B3DCTM (left column) and TOMCAT (middle column) and their relative difference (right column) for the period 1990-2011.

The comparison of BrO between the models is shown in Fig. 8.5. B3DCTM (panel a) and TOMCAT (panel b) agree well in the amount of stratospheric BrO, and the RD (panel c) mostly does not exceed ± 10% in the stratosphere. Significant difference between the model simulations is seen at high latitudes of both hemispheres above 1 hPa, where B3DCTM shows up to 40% lower BrO content. At high latitudes NH at around 100 hPa B3DCTM shows around 15-20% less BrO in comparison with the TOMCAT model.

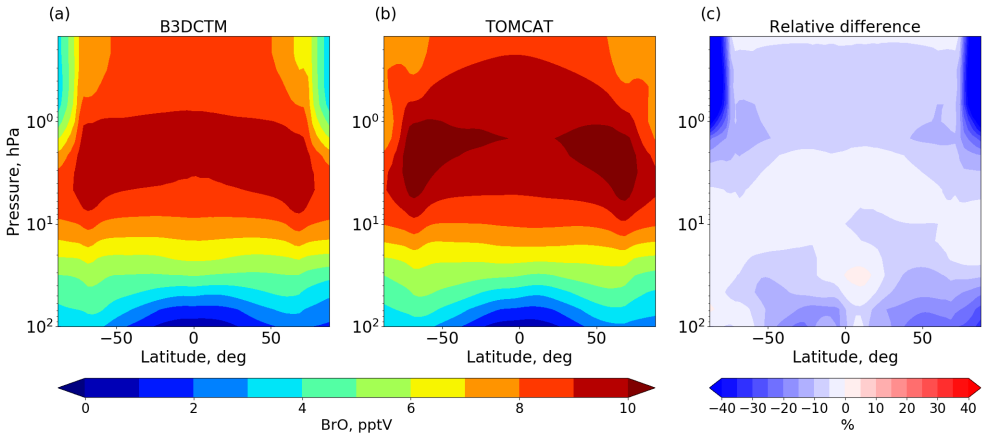

Figure 8.5: Same as Fig. 8.4, but for BrO.

As mentioned in Chapter 5, since both the B3DCTM and TOMCAT models are driven by ECMWF reanalyses, the meteorological temperature may impact the modelled distribution of chemical constituents. To verify whether the temperature from the models has an impact on the differences in O_3, NO_2, and N_2O, Fig. 8.6 shows temperature profiles from B3DCTM (blue) and TOMCAT (magenta) in the top row, and their RD in the bottom row. The analysis was done for 3 different latitude bands: 10°S-10°N (a,d) representing the tropical region, 35°N-60°N (b,e) standing for the high latitudes NH, and 35°S-60°S (c,f) standing for the high latitudes SH. In the tropical region above 100 hPa TOMCAT shows higher temperatures up to 1 K in comparison with B3DCTM, lower temperatures at 10 hPa by 1-1.5 K, and at 1 hPa (∼47 km) around 2 K higher temperatures. At middle latitudes of both hemispheres the agreement between models is very good between 100 and 10 hPa. Similar to the tropical region, at 10 hPa, TOMCAT temperatures are around 1 K lower in comparison with B3DCTM. Development of the TOMCAT model to improve the method for averaging the analysed temperatures onto the model grid has caused these differences with B3DCTM. It should be borne in mind that there could be similar differences in the processing of wind fields.

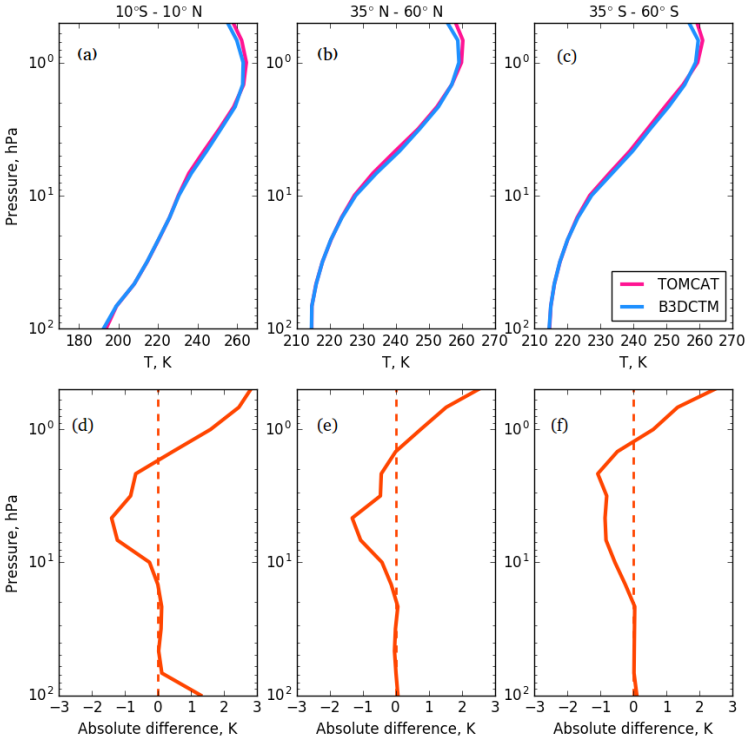

Figure 8.6: Zonally averaged temperature (T) profiles from the B3DCTM (blue) and TOMCAT (magenta) models and their absolute differences for 3 latitude bands: (a,d) tropics, (b,e) middle latitudes NH, and (c,f) middle latitudes SH. Both models use ECMWF ERA-Interim data as the input temperature data set.

8.3 Comparisons between models and satellite measurements

To further estimate the performance of both models, we compared their results with satellite measurements from SCIAMACHY and MIPAS. Figure 8.7 shows zonally averaged O_3 profiles at three different latitudinal bands: (a) tropics, (b) middle latitudes NH, and (c) middle latitudes SH, comparable to Fig. 8.6, for the period 2005-2011. Colour coding stands for data source: TOMCAT - magenta, B3DCTM - blue, SCIAMACHY - green, MIPAS - black. Shaded areas stand for 1σ standard deviation of satellite measurements.

In most cases both models simulate O_3 VMR within the measurement uncertainties. In the tropics (Fig. 8.7a) B3DCTM overestimates the amount of O_3 between around 23-27 km in comparison with the TOMCAT model and satellite measurements. The TOMCAT O_3 profile within this altitude range is in-between SCIAMACHY and MIPAS measurements. Above 27 km both models underestimate the amount of O_3 in comparison with SCIAMACHY and MIPAS.

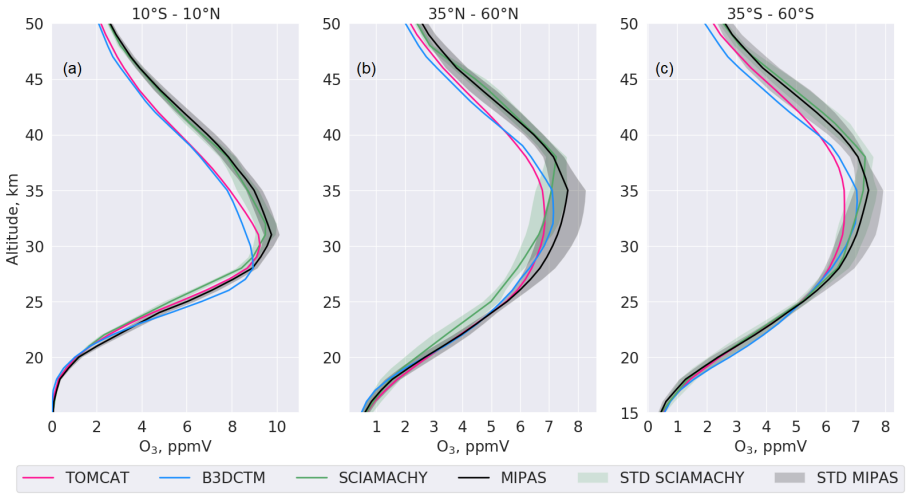

Figure 8.7: Zonally averaged O_3 profiles over 3 latitude bands, similar to Fig. 8.6 for the period 2005-2011. Colour coding stands for data source: TOMCAT -magenta, B3DCTM - blue, SCIAMACHY - green, MIPAS - black. Shaded areas stand for 1σ standard deviation.

At middle latitudes NH (Fig. 8.7b) both models are in agreement with MIPAS measurements below 25 km. Between 25-35 km B3DCTM and TOMCAT simulate O_3 within either the SCIAMACHY or MIPAS measurement uncertainties. However, SCIAMACHY measurements between around 19-38 km altitude show less O_3 in comparison with MIPAS measurements. At SH middle latitudes (Fig. 8.7c) both satellite measurements are in good agreement and the models underestimate O_3 above around 26 km. In particular, TOMCAT simulates less O_3 within the altitude range 27-40 km and more above 40 km in comparison with B3DCTM.

To better illustrate the modelled seasonal variations of O_3 and their agreement with satellite measurements, Fig. 8.8 shows O_3 time series at 22, 28, and 34 km altitude from 2005 to 2011. In the tropical region at 34 km altitude (panel a) both satellite instruments agree well in O_3 content and its variability; B3DCTM and TOMCAT show less O_3 than measurements; at 28 km (panel d) TOMCAT agrees well with MIPAS satellite measurements, in contrast to B3DCTM, whose results have higher variability; at 22 km (panel g) SCIAMACHY shows less O_3 than MIPAS measurements, and both models show higher O_3 variability in comparison with satellite measurements. At NH middle latitudes (panels b,e,h) both models and satellite measurements agree rather well, with the exception of MIPAS measurements, which at 34 and 28 km altitudes show higher O_3 content than both models and SCIAMACHY. In turn, SCIAMACHY measurements show lower O_3 content at 28 km and below (see also panels e,h). At SH middle latitudes (Fig. 8.8c,f,i) at all analysed altitudes satellite measurements agree

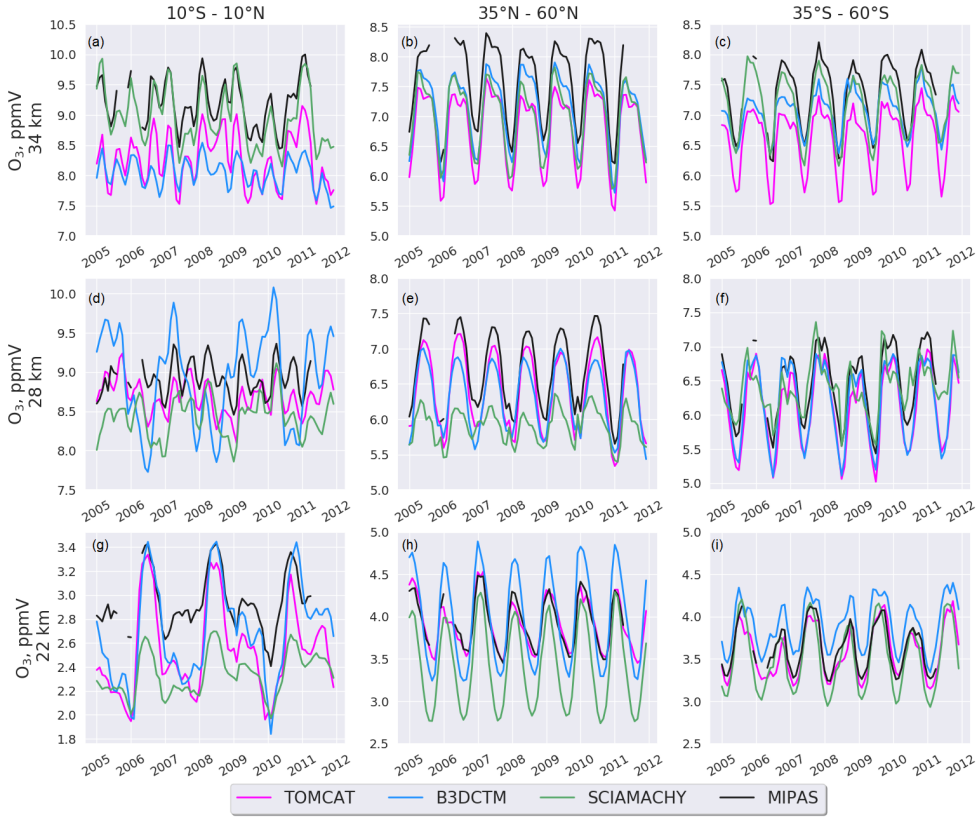

Figure 8.8: O_3 time series at 22, 28, and 34 km altitude from 2005 to 2011. Colour coding and latitudinal bands are similar to Fig. 8.7.

rather well. At 34 km (panel c) TOMCAT shows lower O_3 values in comparison with B3DCTM and measurements. At 22 km (panel i) B3DCTM shows higher O_3 content, while TOMCAT agrees well with MIPAS and SCIAMACHY measurements.

The comparisons of NO_2 both for profiles and time series was performed in the similar manner as for O_3. Both models, B3DCTM and TOMCAT were sampled at the same time as the satellite measurements to account for the illumination conditions, which significantly impact NO_2 diurnal variability (see Sect. 2.2.2). This analysis was considered as NO_2, while belonging to NO_x family, actively impacts stratospheric O_3 chemistry (see Sect. 2.2.2). Figure 8.9 shows zonally averaged NO_2 profiles at three different latitudinal bands, similar to Fig. 8.7. In the tropical stratosphere (Fig. 8.9a) both satellite instruments and TOMCAT are in good agreement to up to 32 km altitude. Above 32 km altitude TOMCAT shows higher NO_2 content in comparison with MIPAS and SCIAMACHY. In turn, B3DCTM shows significantly higher amount of NO_2 between around 24 and 33 km altitude, but agrees well with TOMCAT

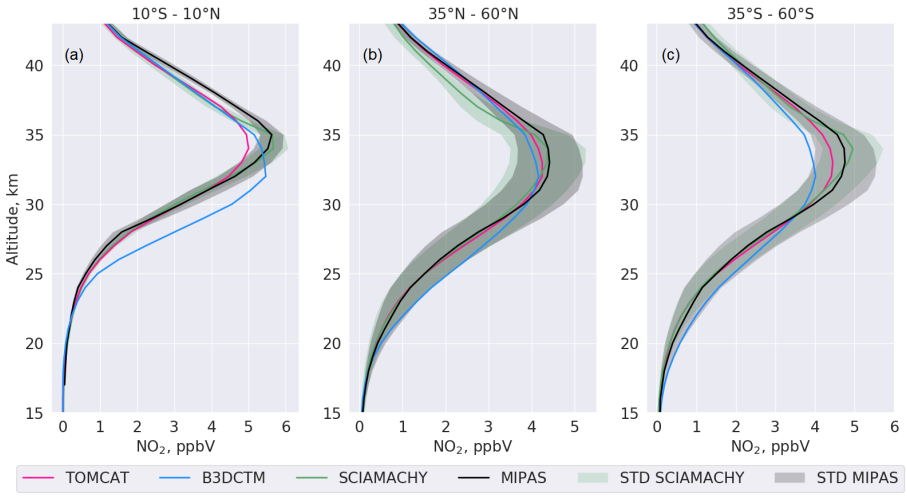

Figure 8.9: Same as Fig. 8.7, but for NO_2.

above 36 km. SCIAMACHY, in contrast to MIPAS, shows less NO_2 above 35 km, which makes its agreement with both models very good at higher altitudes. At the high latitudes of both hemispheres (see panels b and c) the TOMCAT model agrees much better with satellite measurements than B3DCTM, which shows higher NO_2 content below 29 km in SH (panel c) and between 20-30 km in the NH (panel b) and lower NO_2 content between 30-38 km in the SH (panel c).

The time series of NO_2 (see Fig. 8.10) show that in the tropical region at 34 km (panel a) both satellite instruments agree well on NO_2 content. TOMCAT shows lower amounts of NO_2 in comparison with measurements and B3DCTM. At 28 km (panel d) MIPAS shows much less NO_2 in comparison with SCIAMACHY and TOMCAT, which agree well between each other. B3DCTM at this altitude significantly overestimates NO_2 content. At 22 km altitude (panel g) SCIAMACHY agrees with both models. At the middle latitudes of the NH and SH (Fig. 8.10b-c, e-f, and h-i) the agreement between measurements and models is good, except for 34 km altitude in the SH (panel c), where B3DCTM shows lower NO_2 content, and 22 km of both hemispheres (panels h and i), where B3DCTM shows higher NO_2 content in comparison with the TOMCAT model and satellite measurements.

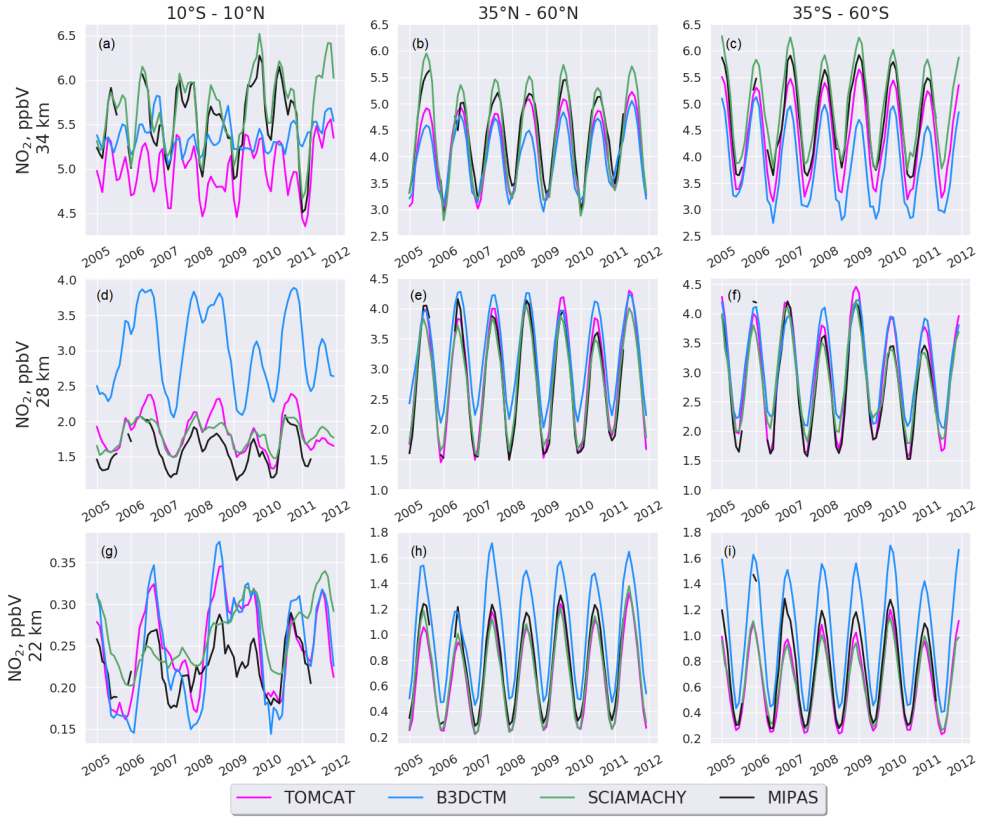

Figure 8.10: Same as Fig. 8.8, but for NO_2.

As mentioned in Sect. 2.2.1, in the stratosphere N_2O affects O_3 concentrations mainly via the NO_x cycle, but, as a long-lived source gas, it is also a tracer of the stratospheric circulation. Therefore, similar to NO_2 comparisons, modelled N_2O was also evaluated. Figure 8.11 is similar to Fig. 8.9, with the exception for SCIAMACHY measurements as it does not measure N_2O. In all latitude bands N_2O simulated by the TOMCAT model agrees well with the MIPAS satellite measurements above 20 km altitude and is within its measurements' uncertainties. B3DCTM in nearly all latitude bands and at nearly all altitudes underestimates the amount of N_2O, apart from the tropical lower stratosphere (panel a, around 20-24 km), where the agreement between models and the MIPAS measurements is good. The possible reasons for the N_2O underestimation by B3DCTM in comparison with the TOMCAT model and the MIPAS measurements are discussed below.

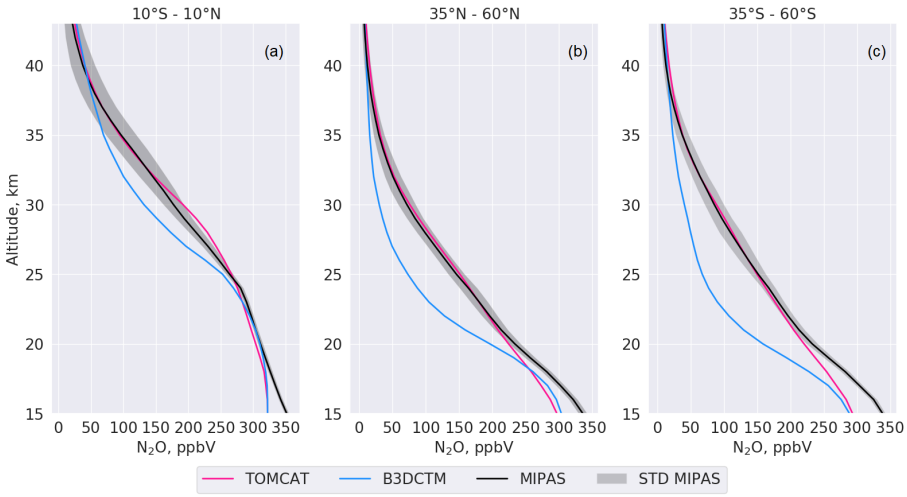

Figure 8.11: Same as Fig. 8.9, but for N_2O. Only MIPAS satellite data are included.

The time series of N_2O are shown in Fig. 8.12. TOMCAT agrees well with the MIPAS satellite measurements in most analysed cases, except for the tropical region, where at 26 km (panel d) TOMCAT shows higher and at 22 km (panel g) shows lower N_2O content in comparison with MIPAS. B3DCTM underestimates amount of N_2O in comparison with the MIPAS measurements and the TOMCAT model in all analysed cases, except for the tropical region at 22 km altitude (see panel g). The underestimation of N_2O in B3DCTM can be directly linked to the higher AoA values in comparison with the TOMCAT results, shown in Fig. 8.1a,b. The major source of the stratospheric N_2O is its transport from the lower altitudes (see Sect. 2.2.1). Slower transport in B3DCTM (which is shown in Fig. 8.1a) indicates that a) less N_2O is transported from the bottom boundary layer of the model, b) a longer residence time of N_2O in the stratosphere, and c) larger N_2O photochemical destruction via Reaction (R19), which is around 95% of the total N_2O loss and Reactions (R20a-R20b), which is around 5% of the total N_2O loss (see also Fig. 2.2b). However, as seen from Fig. 8.11a, in the tropical lower stratosphere the amount of N_2O in both models is very similar, around 320 ppbV. In B3DCTM longer residence time of N_2O also leads to higher NO_x production via Reaction (R20a) and therefore higher NO_2 content in the tropical stratosphere between 24 and 33 km in comparison with TOMCAT model (see Fig. 8.9a and Fig. 8.10d). In the tropical middle stratosphere NO_2, as part of the NO_x family, is responsible for the majority of O_3 loss (see Sect. 2.2.2 and Reactions (R21) and (R22)). Therefore, there is less O_3 between around 30-35 km in the tropics in B3DCTM in comparison with TOMCAT (see Fig. 8.7a and 8.8a).

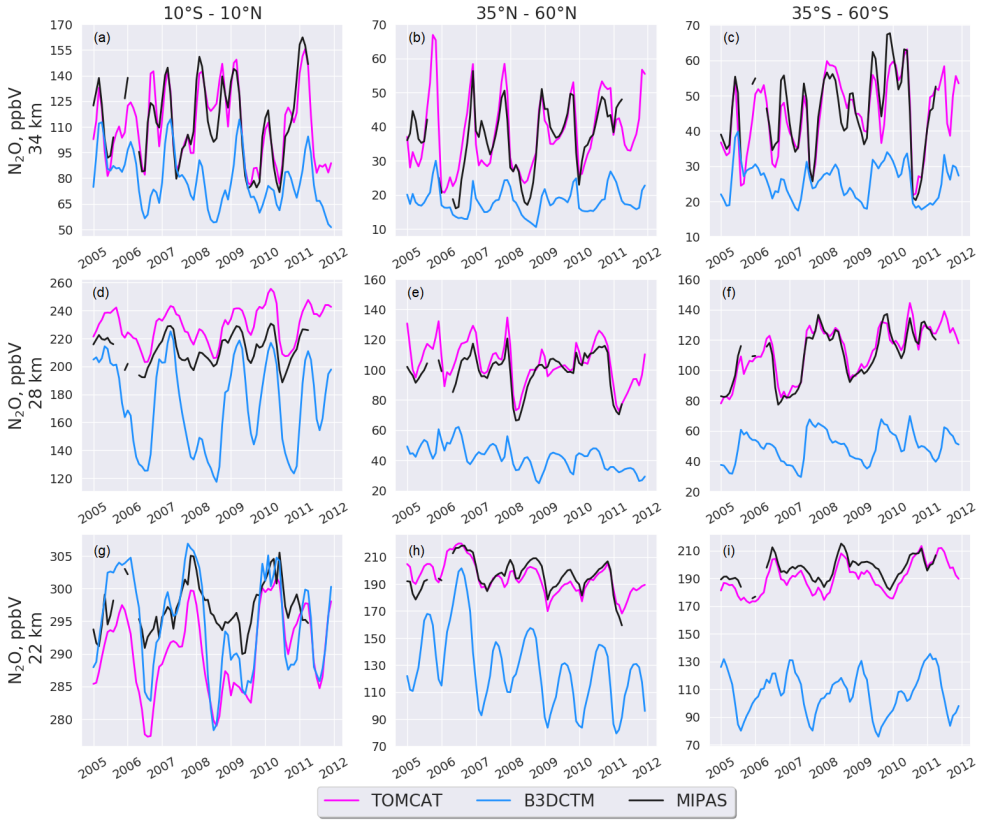

Figure 8.12: Same as Fig. 8.10, but for N_2O. Only MIPAS satellite data are included.

The comparison of BrO distribution in both models and satellite measurements was also performed similar to O_3, NO_2, and N_2O. Figure 8.13a-c shows zonally averaged BrO profiles at three different latitudinal bands in the altitude range between 18 and 30 km. For satellite measurements only SCIAMACHY data were involved. Both models, B3DCTM and TOMCAT were sampled at the same time as the SCIAMACHY measurements to account for the illumination conditions. From Fig. 8.13 it is seen that B3DCTM shows lower content of stratospheric BrO up to 28 km altitude in the tropics and at middle latitudes NH (panels a and b), and up to 29 km at the middle latitudes SH (panel c) in comparison with both the SCIAMACHY measurements and the TOMCAT model. In the tropical region (panel a) TOMCAT agrees well with SCIAMACHY up to around 26 km altitude. TOMCAT calculates lower amounts of BrO between 15 and 26 km at the middle latitudes NH (panel b) and between 15 and 28 km at the middle latitudes SH (panel c). However, it should be noted that SCIAMACHY BrO retrieval suffers from a loss of sensitivity above 28 km altitude.

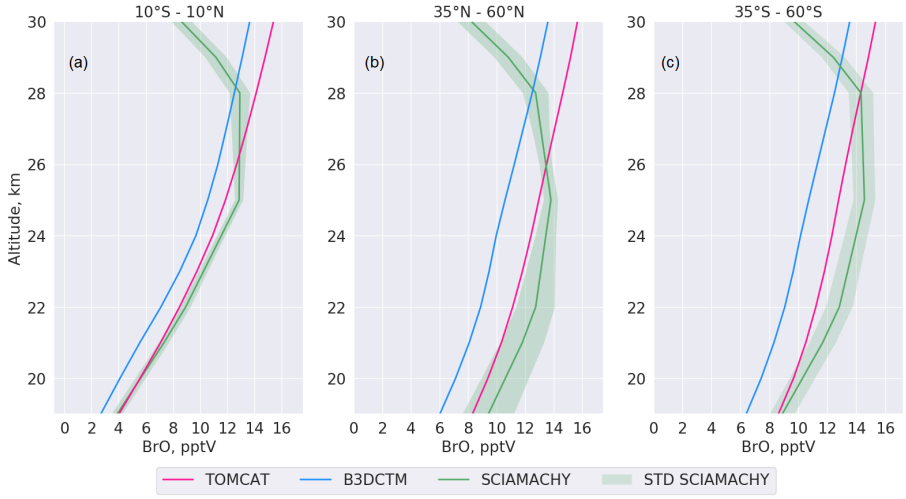

Figure 8.13: Same as Fig. 8.9, but for BrO. Only SCIAMACHY satellite data are included.

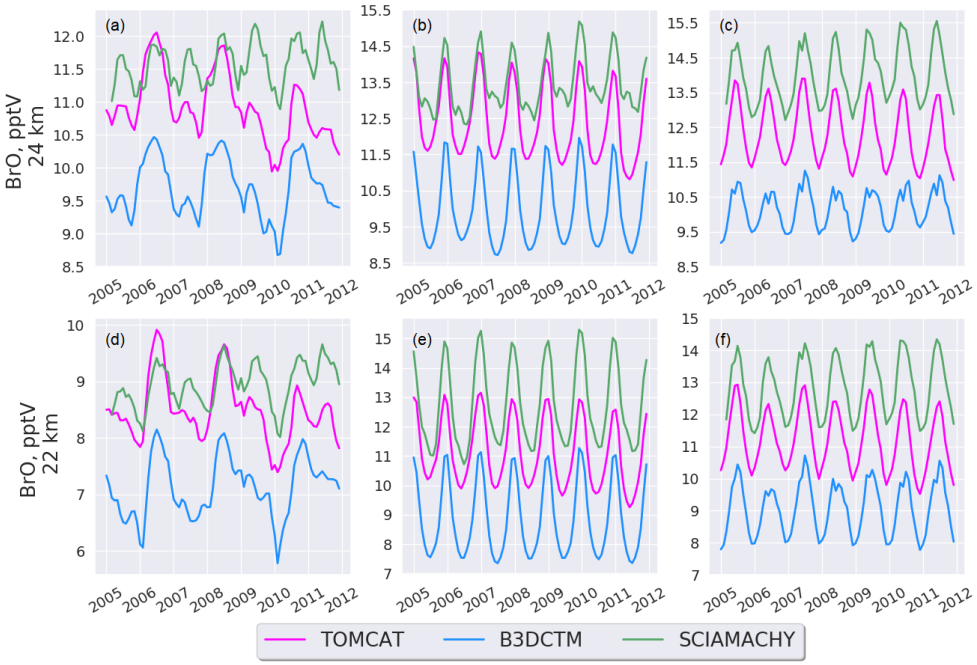

Figure 8.14: Same as Fig. 8.10, but for BrO. Only SCIAMACHY satellite data are included.

The time series of BrO are shown in Fig. 8.14a-f. Only altitudes of 24 (panels a-c) and 22 km (panels d-f) were considered in the analysis. Similar to Fig. 8.13, B3DCTM shows lower BrO content at the analysed latitudes and altitudes (all panels). Although the TOMCAT model also shows less BrO in comparison with measurements, its agreement with SCIAMACHY

is much better, than that of B3DCTM.

The analysis and comparison of trace gases (O_3, NO_2, N_2O, and BrO) from the B3DCTM and TOMCAT models and the satellite measurements from SCIAMACHY and MIPAS provided a basis to validate models results. In most cases the agreement of the TOMCAT model with satellite measurements was much better than for B3DCTM. However, TOMCAT in general shows lower O_3 and NO_2 concentrations compared to the SCIAMACHY measurements in the middle stratosphere. The reason for these differences between model and measurements could not be identified so far. As an increase of NO_2 in the tropical middle stratosphere decreases the amount of O_3 (Fig. 8.7a), it is unlikely that the transport can cause the observed negative bias in both species. Rather, there is likely a photochemical reason. Either the model underestimates the production of O_3 from O_2 photolysis in this region (R1), or there are deficits in the model NO_x chemistry reducing the impact of NO_2 on O_3. The latter would then be associated with the reactions NO + O_3 (R21), O + NO_2 (R22), or NO_2 photolysis (R23).

9

Validation of SCIAMACHY NO_2 scientific retrieval V4.0

The investigation of the performance of the SCIAMACHY NO_2 scientific retrieval V4.0 developed at the IUP, University of Bremen is performed by comparing it with different limb and occultation satellite data sets. The description of co-location criteria, applied filters and diagnostics etc. is provided in Sect. 6. The validation of SCIAMACHY NO_2 scientific retrieval V4.0 was done at seven latitudinal bands: tropics (20°S-20°N), middle latitudes I NH (20-40°N), middle latitudes I SH (20-40°S), middle latitudes II NH (40-60°N), middle latitudes II SH (40-60°S), high latitudes NH (60-80°N), and high latitudes SH (60-80°S). These latitude bands were defined in order to identify possible meridional differences in NO_2 profiles between the compared data sets (see also Sect. 6.2).

First, Sect. 9.1 shows the results from the comparison of SCIAMACHY IUP V4.0 data without photochemical correction, namely with SCIAMACHY IUP V3.1 (older version), SCIAMACHY ESA V7.00, MIPAS ESA V7.03, and MIPAS IMK-IAA V5R NO_2 data sets. Afterwards, Sect. 9.2 shows the comparison of SCIAMACHY IUP V4.0 with the SAGE II V7.0 data set including the application of the photochemical correction (described in Sect. 6.3.1.4 and 6.3.2) to the latter dataset. Each subsection comprises the analysis of averaged profiles, their RDs, and the correlation profiles between data sets. It also includes the comparison of NO_2 time series and their RDs at different altitudes for different latitudinal bands.

9.1 Comparison without photochemical correction

9.1.1 SCIAMACHY IUP V3.1

The comparison of SCIAMACHY IUP V4.0 with older V3.1 NO_2 profiles is shown in Fig. 9.1. It is based on the spatio-temporal co-location criteria of 60 km and 3.6 seconds during the period of 2002-2012. From left to right, the plot shows panels with averaged profiles of SCIAMACHY IUP V4.0 (green) and V3.1 (blue) NO_2 and their STDs (shaded areas), RD profiles (magenta) and STDs of RD profiles (shaded areas). From top to bottom, the plot shows panels at different latitude bands, defined in Sect. 6.2. The number of co-located profiles at the corresponding latitude band is shown in the first plot of each row of Fig. 9.1.

The number of co-located profiles between SCIAMACHY IUP V4.0 and V3.1 varies from 287888 between 60-80° SH (panel f) to 657106 in the tropical region between 20°S-20°N (panel a). The agreement of both SCIAMACHY IUP data sets V4.0 and V3.1 is good and at the altitude region between 25 and 35 km the RD does not exceed ± 2-3% at all latitude bands (shown in the middle column of Fig. 9.1). Between around 35 and 40 km SCIAMACHY IUP V4.0 shows around 10-20% lower NO_2 content in comparison with older V3.1 at all analysed latitude bands, except for high latitudes SH (60-80°, panel f). Below 23 km SCIAMACHY IUP V4.0 shows around 10% higher NO_2 content in the tropical region (20°S-20°N, panel a), at the middle latitudes I SH (20-40°, panel b), and at the middle latitudes II NH (40-60°, panel e).

The correlation profiles (see Sect. 6.4) of analysed data sets are shown in the right column of Fig. 9.1. The vertical dashed lines indicate an arbitrary threshold of high correlation, which is represented by the value of 0.8. The correlation between SCIAMACHY IUP V4.0 and V3.1 is high at all analysed latitude bands at the altitude range of 18-40 km (close to 1, in the tropical region at the altitude range of 25-35 km). However, above 40 km the correlation becomes moderate ($\leq$ 0.8) in the tropical region (panel a), at the middle latitudes I and II NH (panels c and e), and at the high latitudes NH (panel g).

To further analyse the differences in the seasonal NO_2 distribution between the two data sets, Fig. 9.2 shows the time series of SCIAMACHY IUP V4.0 (green) and V3.1 (blue) NO_2 measurements at four altitudes: 22, 28, 34, and 38 km. The altitudes are the same as in Sect. 8.3. Time series at 38 km were added to extend the comparison to higher stratospheric altitudes.

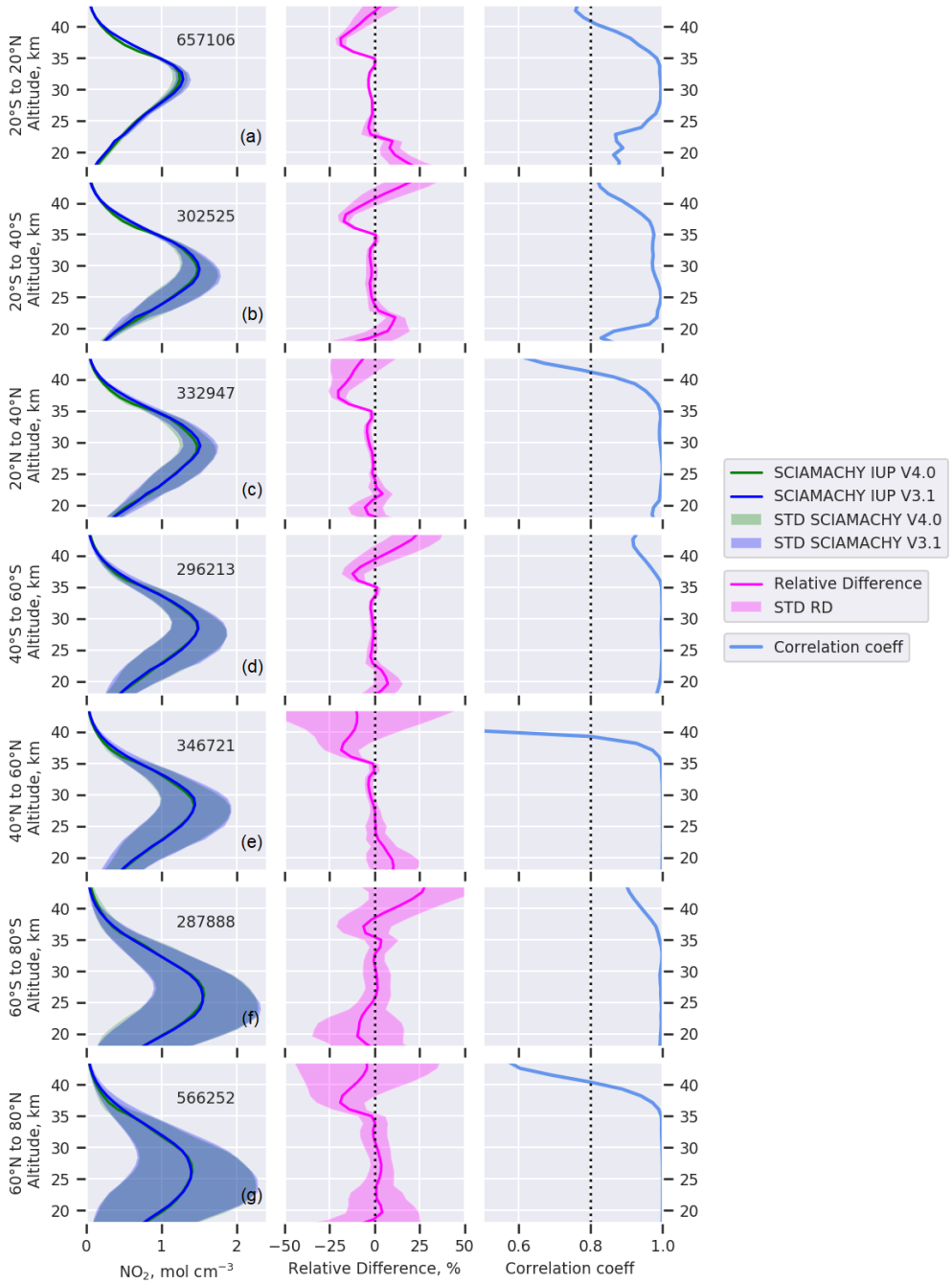

Figure 9.1: Averaged profiles of SCIAMACHY IUP V4.0 (green) and V3.1 (blue) NO_2 and their STDs (shaded areas, left column), RDs of profiles (magenta) and STDs of RD profiles (shaded areas, middle column), and the correlation profiles between data sets (light blue, right column). From top to bottom, the plot shows panels at different latitude bands. The amount of co-located profiles for the corresponding latitude band is shown in the first panel of each row.

Figure 9.2 shows a good agreement of NO_2 seasonal distribution between SCIAMACHY IUP V4.0 and V3.1 at the middle and high latitudes within the altitude range of 22-34 km (panels c-g). In the tropical region (panel a) and at the middle latitudes I SH (panel b) SCIAMACHY IUP V4.0 shows higher NO_2 content at the altitude of 22 km and lower at 38 km (also seen in Fig. 9.1a). Overall, at 38 km altitude SCIAMACHY IUP V4.0 shows lower concentrations of NO_2 at all latitude bands.

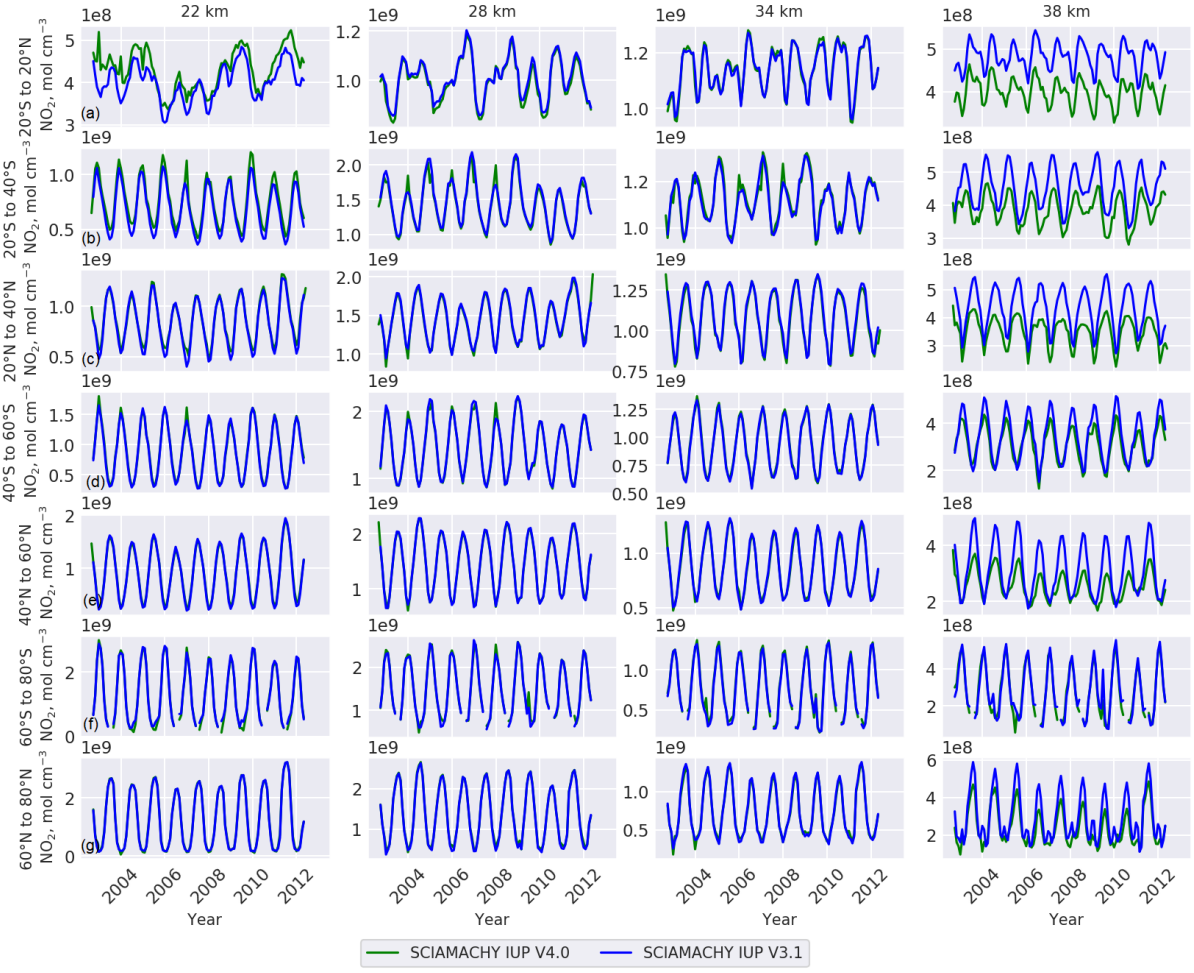

Figure 9.2: Time series of SCIAMACHY IUP V4.0 (green) and V3.1 (blue) NO_2 measurements. From left to right, the plot shows time series at different altitudes (22, 28, 34, and 38 km). From top to bottom, the plot shows panels at different latitude bands, similar to Fig. 9.1.

For a better interpretation of the seasonal differences of NO_2 between SCIAMACHY IUP V4.0 and V3.1, the time series of RD were calculated and are shown in Fig. 9.3. In the tropical region (panel a) and at the middle latitudes I and II of both hemispheres (panels b and c) at the

Figure 9.3: Time series of the RD of retrieved NO_2 from SCIAMACHY IUP V4.0 and V3.1 for four different altitudes, from left to right: 22, 28, 34, and 38 km. Colour coding indicates the RD at particular latitude band: tropics - magenta, middle latitudes I SH - dark green, NH - yellow, middle latitudes II SH - orange, NH - blue, high latitudes SH - dark pink, NH - light green.

altitudes of 28 and 34 km the RD varies mostly within ± 5%. In this region the RD increases with altitude and at 38 km it is around -20%. At the high latitudes of the NH and SH (panel d) at 28 and 34 km the RD varies mostly within ± 20%, although at 38 km it is around -40 ≤ RD ≤ 20%. In the lower stratosphere at 22 km altitude, in the tropical region (panel a) the RD varies within 0 ≤ RD ≤ 20%. At the middle latitudes I of both hemispheres (panel b) it is ± 20%, and at the middle latitudes II of both hemispheres (panel c) it is 0 ≤ RD ≤ 40%. At the high latitudes of both hemispheres (panel d) at the altitude of 22 km the variability of RD is much higher in comparison with that at lower latitudes, i.e. ± 40%.

9.1.2 SCIAMACHY ESA V7.00

The comparison of SCIAMACHY IUP V4.0 and SCIAMACHY ESA V7.00 NO_2 profiles during the period of 2002-2012 is shown in Fig. 9.4. The spatio-temporal criteria (60 km and 3.6 seconds) did not change (see Sect. 9.1.1), as the comparison is done for the same instrument, but for different retrieved data. Figure 9.4 is similar to Fig. 9.1, but here blue stands for the SCIAMACHY ESA V7.00 NO_2 data set.

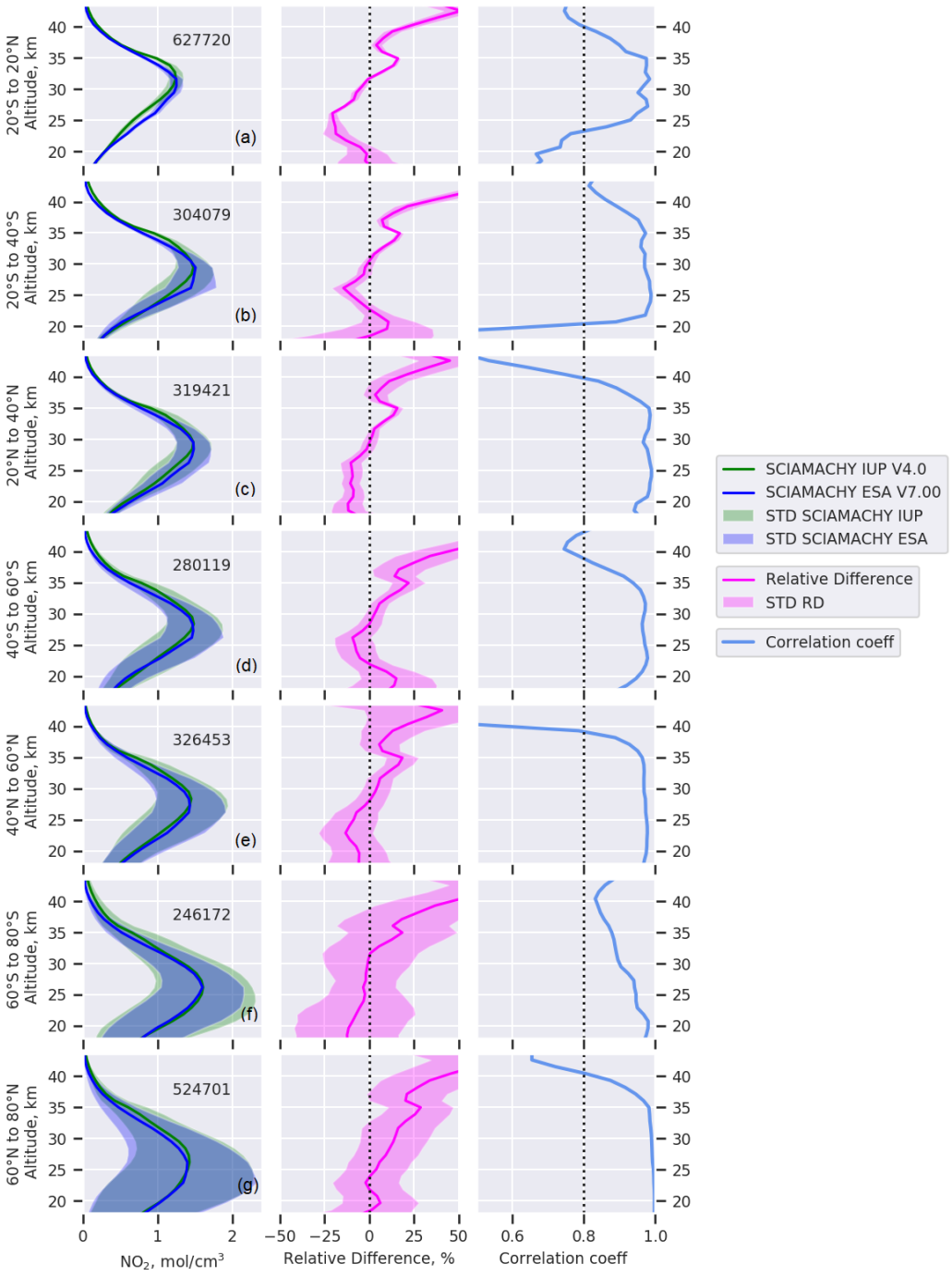

Figure 9.4: Same as Fig. 9.1, but for SCIAMACHY IUP V4.0 NO_2 (green) and SCIAMACHY ESA V7.00 NO_2 (blue) measurements.

The number of co-locations (see the left column of Fig. 9.4) varies from 246172 between 60-80° SH (panel f) to 627720 in the tropical region between 20°S-20°N (panel a). As seen in Fig. 9.4, both data sets agree well on the stratospheric NO_2 content; however, SCIAMACHY IUP shows lower NO_2 concentrations at around 20-25 km altitude at almost all latitude bands (except at the high latitudes NH, panel g). In the tropical region (Fig. 9.4a) SCIAMACHY IUP shows less NO_2 up to 30 km, i.e. between 20-25 km the RD is increasing up to around -23%, and from 25 to 31 km the RD becomes smaller and reaches 0 at around 32 km altitude. In the tropical region between 32-40 km altitude the RD is within 15%. At the middle latitudes I NH and SH (panels b and c) and at the middle latitudes II NH and SH (panels d and e) the RD is within ± 15% at the altitude range of 19-39 km. At the high SH latitudes (panel f) the RD varies within ± 10% up to 33-34 km (at 25-32 km altitudes the RD does not exceed -5%) and at the high latitudes NH (panel g) the RD is close to 0 in the lower stratosphere (within 19-25 km altitude), and increases with altitude above. The agreement between the two data sets has improved significantly at high latitudes (panels f and g) in comparison with the validation of older SCIAMACHY ESA and IUP NO_2 data sets (see Galytska et al., 2017, Fig.6).

The correlation of SCIAMACHY IUP V4.0 and SCIAMACHY ESA V7.00 NO_2 data sets is high at most of the altitudes and latitude bands. However, in the tropical region (panel a) the correlation becomes moderate below 24 km and above 40 km. The decrease of the correlation from high to moderate above 40 km is also observed at the middle latitudes I and II NH (panels c and e) and at the high latitudes NH (panel g).

To further analyse the seasonal changes of the compared data sets, Fig. 9.5 shows the time series of SCIAMACHY IUP (green) and SCIAMACHY ESA (blue) NO_2 measurements at four altitudes: 22, 28, 34, and 38 km. The time series at the altitude of 38 km was analysed to address the reason for decreasing correlation between the data sets at higher altitudes in the particular latitude regions, shown in Fig. 9.4.

The moderate correlation values (lower than 0.8) between the analysed data sets at lower tropical altitudes (discussed above and shown in panel a of Fig. 9.4) are likely a result of larger interannual variations in comparison with the seasonal changes in NO_2 data from SCIAMACHY IUP (Fig. 9.5a at 22 km). There is stable bias between the data sets in the tropical region (panel a) at 28 and 34 km altitude, but the correlation still persists at the higher values, as the seasonality is relatively similar in both data sets. At 38 km in the tropical region, SCIAMACHY IUP data set suggests an NO_2 decrease with time, which is in contrast to SCIAMACHY ESA data set. Therefore, in the tropical region at higher altitudes the correlation decreases from high

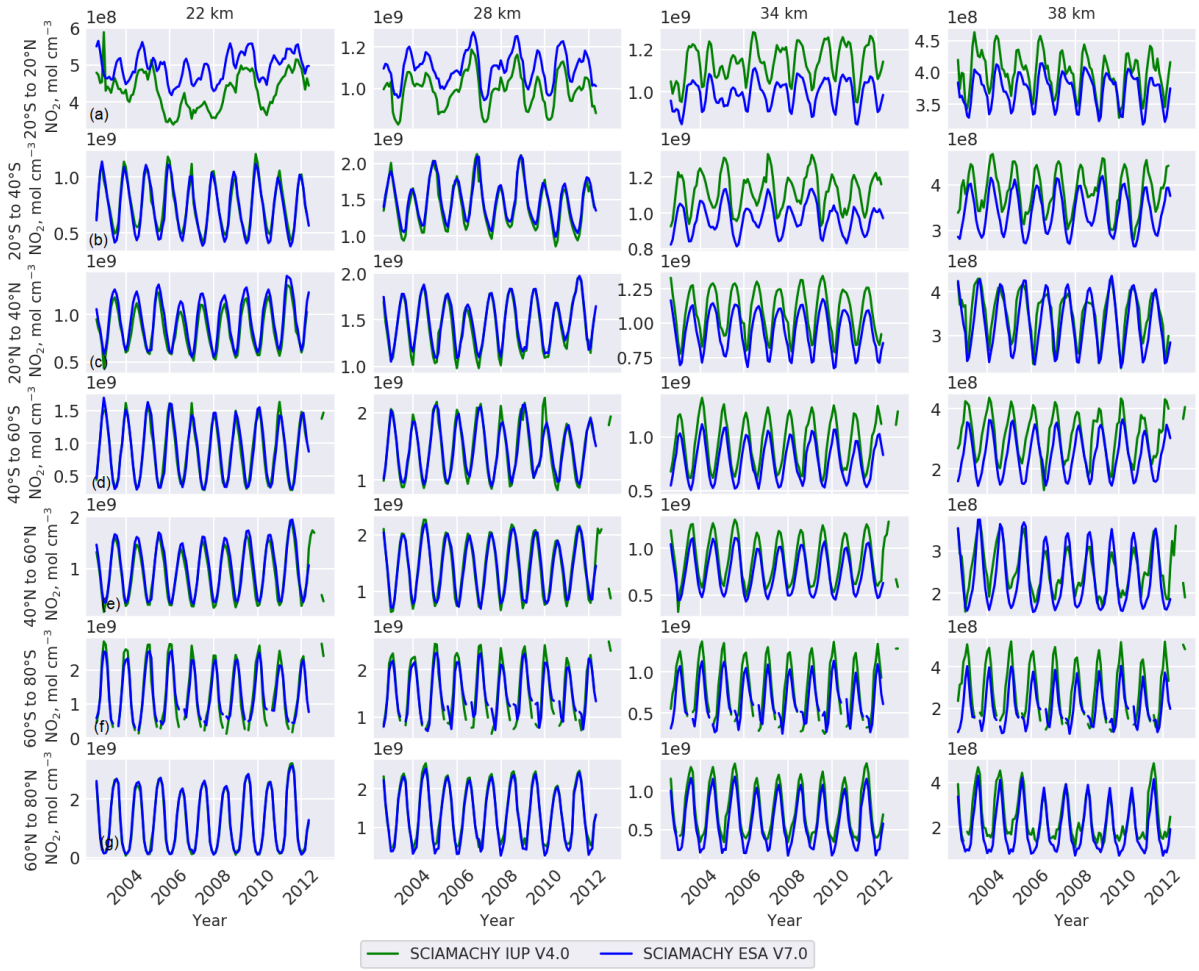

Figure 9.5: Same as Fig. 9.2, but for SCIAMACHY IUP V4.0 NO_2 (green) and SCIAMACHY ESA V7.00 NO_2 (blue) measurements.

to moderate values (as shown in Fig. 9.4a). From Fig. 9.5 it is apparent that the agreement of time series between the analysed data sets is good, in particular at 22 and 28 km at the middle and high latitudes of both hemispheres (see panels b-e). At tropical and SH latitude bands at the altitude of 34 km and at 38 km SCIAMACHY IUP data set shows higher NO_2 concentrations. However, to better interpret seasonal differences between the analysed data sets, the RDs were calculated and are further shown in Fig. 9.6.

From Fig. 9.6 it is apparent that the RD is the lowest (within ± 20% and lower) at higher altitudes, i.e. between 28 and 38 km in the tropical region and at the middle latitudes I of both hemispheres (see panels a and b). At higher latitudes the RD increases up to ± 40% at all analysed altitudes with an increase with latitude. One of the possible reasons for such a high relative difference at the middle and high latitudes (panels c and d) can be an overly strong regularization in SCIAMACHY ESA retrievals. At 28 km altitude in the tropics and at the middle latitudes I (panels a and b) SCIAMACHY IUP shows around 20% less NO_2 in comparison with SCIAMACHY ESA during the analysed time period. At the middle latitudes II of both hemispheres (panel c) the RD sometimes reaches -40%. In general, the variations of RD at high latitudes have higher amplitude and vary within ± 40%. At 34 and 38 km, the RD mostly does not exceed 6% in the tropical region (panel a), which is a good agreement; at the middle latitudes I of both hemispheres (panel b) SCIAMACHY IUP shows around 20% more NO_2 in comparison with SCIAMACHY ESA.

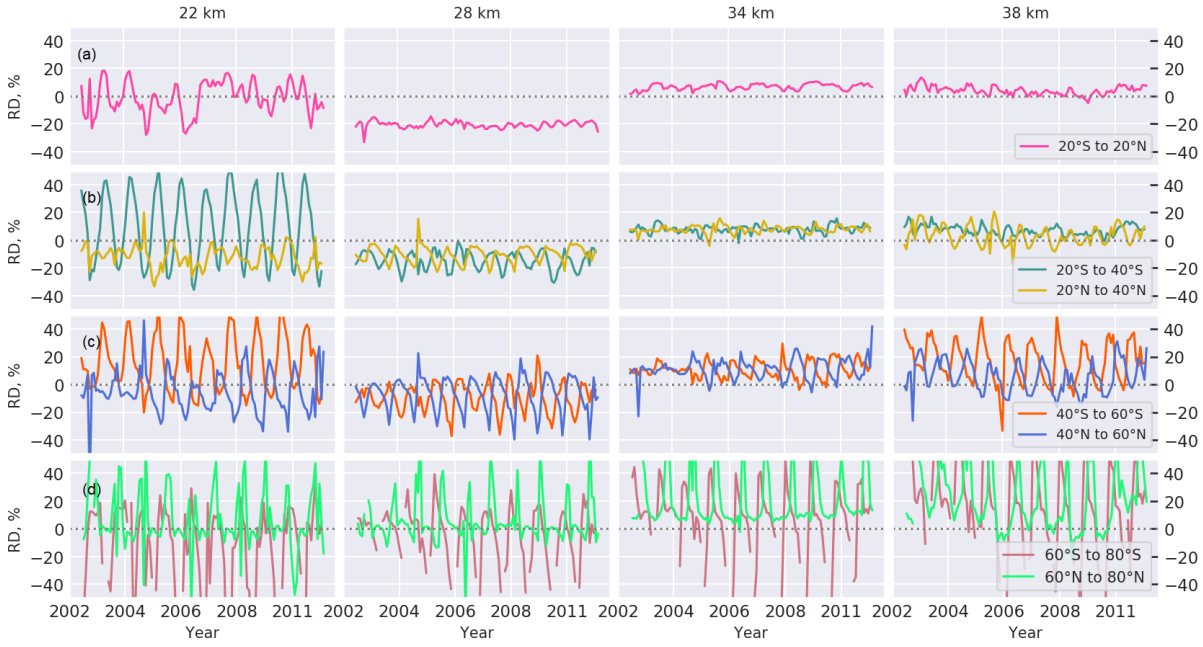

Figure 9.6: Same as Fig. 9.3, but for SCIAMACHY IUP V4.0 NO_2 and SCIAMACHY ESA V7.00 NO_2 measurements.

9.1.3 MIPAS ESA V7.03

The comparison of SCIAMACHY IUP V4.0 and MIPAS ESA V7.03 NO_2 profiles is shown in Fig. 9.7 and is similar to the comparison of SCIAMACHY IUP and ESA data sets, shown in Sect. 9.1.2. The analysis of NO_2 profiles is based on the spatio-temporal co-location criteria of 300 km and 3 hours. As mentioned in Sect. 4.3.2, only the period of 2005-2012 was considered in the comparison, due to changes in the spectral resolution of the MIPAS instrument. Figure 9.7 is similar to Fig. 9.4, but here blue stands for MIPAS ESA data set. The number of co-located profiles between SCIAMACHY IUP and MIPAS ESA NO_2 data varies from 15239 in 40-60° SH (panel d) to 209943 in the tropical region between 20°S-20°N (panel a).

The RD between SCIAMACHY IUP and MIPAS ESA data sets (see Fig. 9.7) varies mostly within ± 10% at all latitude bands over the analysed altitudes, with the exception of altitudes below 20-22 km and in the tropical region and at the middle latitudes of both hemispheres (panels a-e), where the RD reaches -25%, and also below 24-25 km at high latitudes (panels f and g), where the RD between MIPAS ESA and SCIAMACHY IUP exceeds 30%. Moreover, the STD of the RD (magenta shaded area) at all latitude bands is larger, than in the comparison between SCIAMACHY IUP and SCIAMACHY ESA data sets (see Fig. 9.4), which indicates that the spread of RD is much higher.

The correlation between SCIAMACHY IUP and MIPAS ESA NO_2 data sets is high at high latitudes (Fig. 9.7, f and g) and at the middle latitudes I and II in the NH (panels c and e) at the altitude range between around 20 and 40 km. At the middle latitudes I SH (panel d) the correlation is high only at altitudes between 20 and 30 km. In the other regions and altitudes the correlation is moderate.

The time series comparison of SCIAMACHY IUP and MIPAS ESA NO_2 data sets is shown in Fig. 9.8. The seasonal variations of NO_2 from the two instruments have the largest differences in the tropics (panel a), where NO_2 from MIPAS ESA has larger amplitude at all analysed altitudes. Also, at the middle latitudes I of both hemispheres (panels b and c) at the altitudes 34 and 38 km and at the middle and high latitudes II NH (panels e and g) at 38 km altitude the amplitude of seasonal changes in MIPAS ESA data set is larger than in SCIAMACHY IUP. In contrast, at the middle latitudes II SH (panel d) SCIAMACHY IUP data show more pronounced seasonal variations at 34 km altitude in comparison with MIPAS ESA.

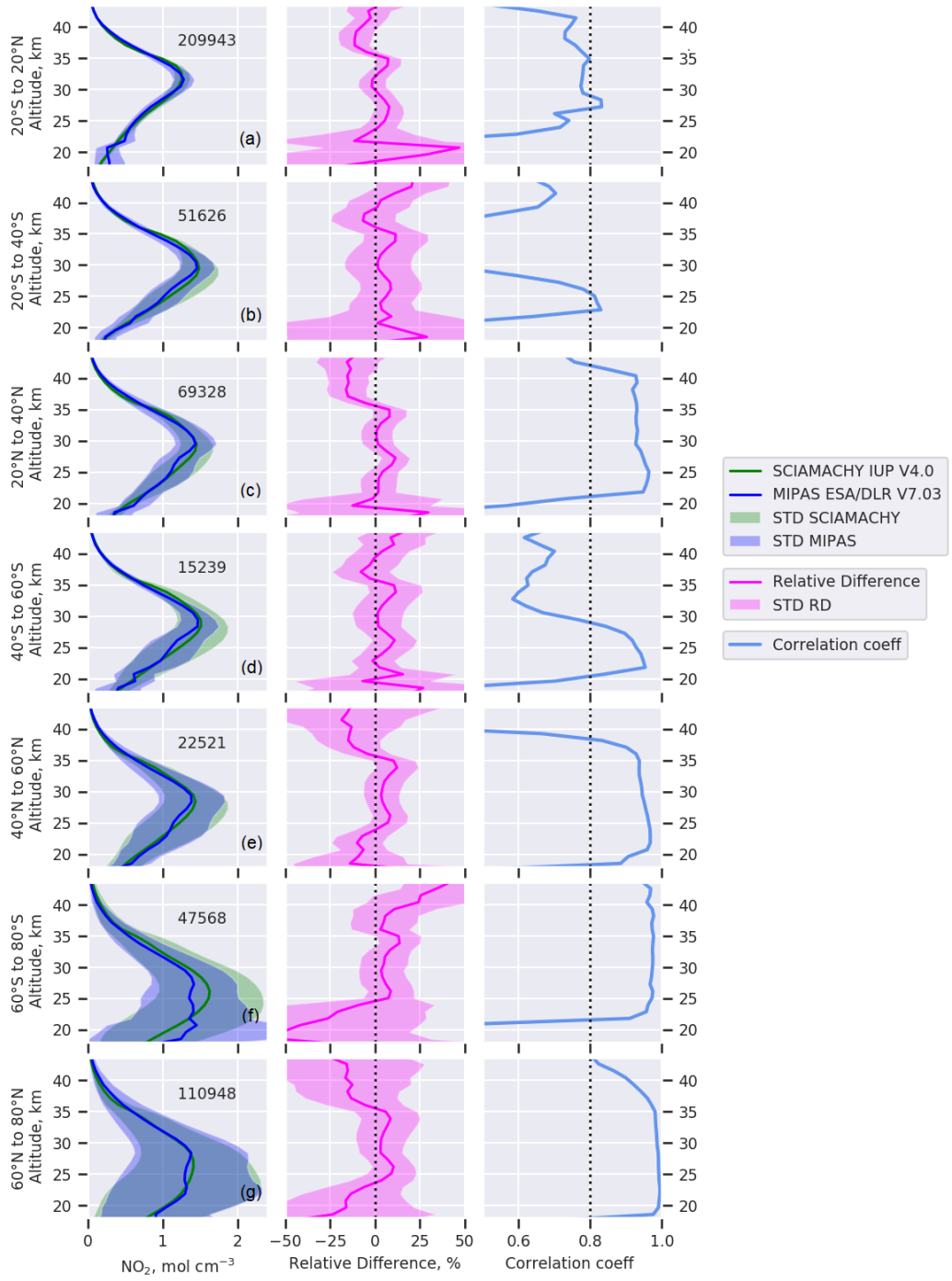

Figure 9.7: Same as Fig. 9.1, but for SCIAMACHY IUP V4.0 NO_2 (green) and MIPAS ESA V7.03 NO_2 (blue) measurements for the period of 2005-2012.

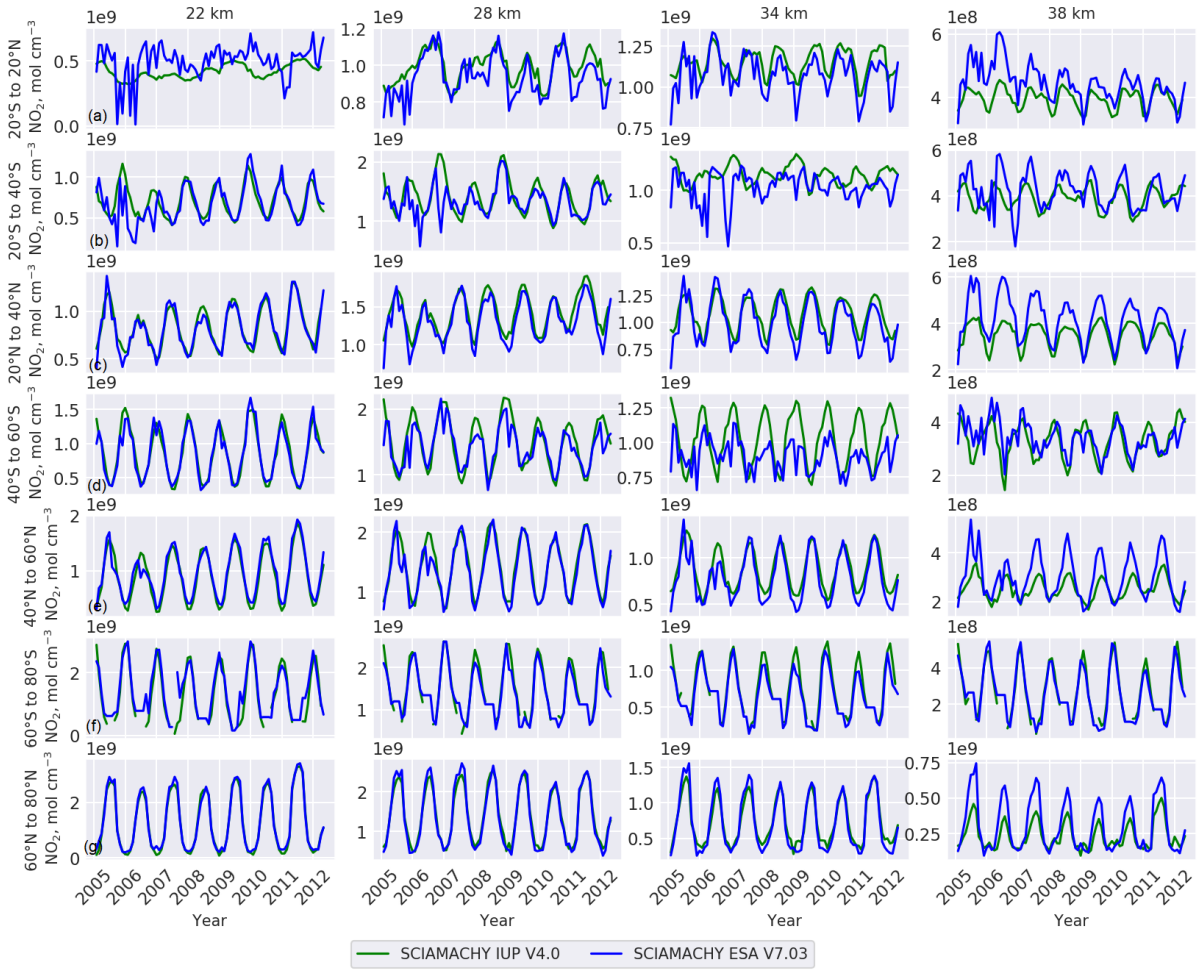

Figure 9.8: Same as Fig. 9.2, but for SCIAMACHY IUP V4.0 NO_2 (green) and MIPAS ESA V7.03 NO_2 (blue) measurements for the period of 2005-2012.

The RD time series are shown in Fig. 9.9, similar to Fig. 9.6. From the analysis above it is apparent that the RDs are largest at 22 km altitude at all latitude bands, and vary within ± 40%. At the altitude of 28 km the RD is mostly positive at the analysed latitudes over the period of 2005-2012. At 28 and 34 km altitude the RD changes mostly within 0-20% in the tropics (panel a) and at the middle latitudes I NH (panel b, yellow). At the high and middle latitudes II (panels c and d) the RD is within ± 40%, but its variability is much smaller in comparison with 22 km altitude.

Figure 9.9: Same as Fig. 9.3, but for SCIAMACHY IUP V4.0 and MIPAS ESA V7.03 NO_2 measurements for the period of 2005-2012.

9.1.4 MIPAS IMK-IAA V5R

Similar to Fig. 9.7 in the previous section, SCIAMACHY IUP data are compared to MIPAS IMK-IAA (Fig. 9.10). The spatio-temporal criteria did not change, as the comparison is done for the same MIPAS instrument, but for different retrieved data. The number of co-located NO_2 profiles between SCIAMACHY IUP and MIPAS IMK-IAA is lower in comparison with MIPAS ESA and varies from 11191 in 40-60° SH (panel d) to 164598 in the tropics (panel a). Generally, SCIAMACHY shows higher NO_2 content in comparison with MIPAS IMK-IAA retrieval at altitudes between 20 and 29 km in the tropical region (panel a) and at the middle latitudes I NH (panel c), where the RD reaches 20%. At other altitudes SCIAMACHY shows higher NO_2 content only between around 25-29 km, and the RD does not exceed 10%. Another interesting pattern is seen in the STD of RD, which for the comparison of SCIAMACHY IUP with MIPAS IMK-IAA NO_2 has much lower spread, than for its previous comparison with MIPAS ESA data set (shown in Fig. 9.7).

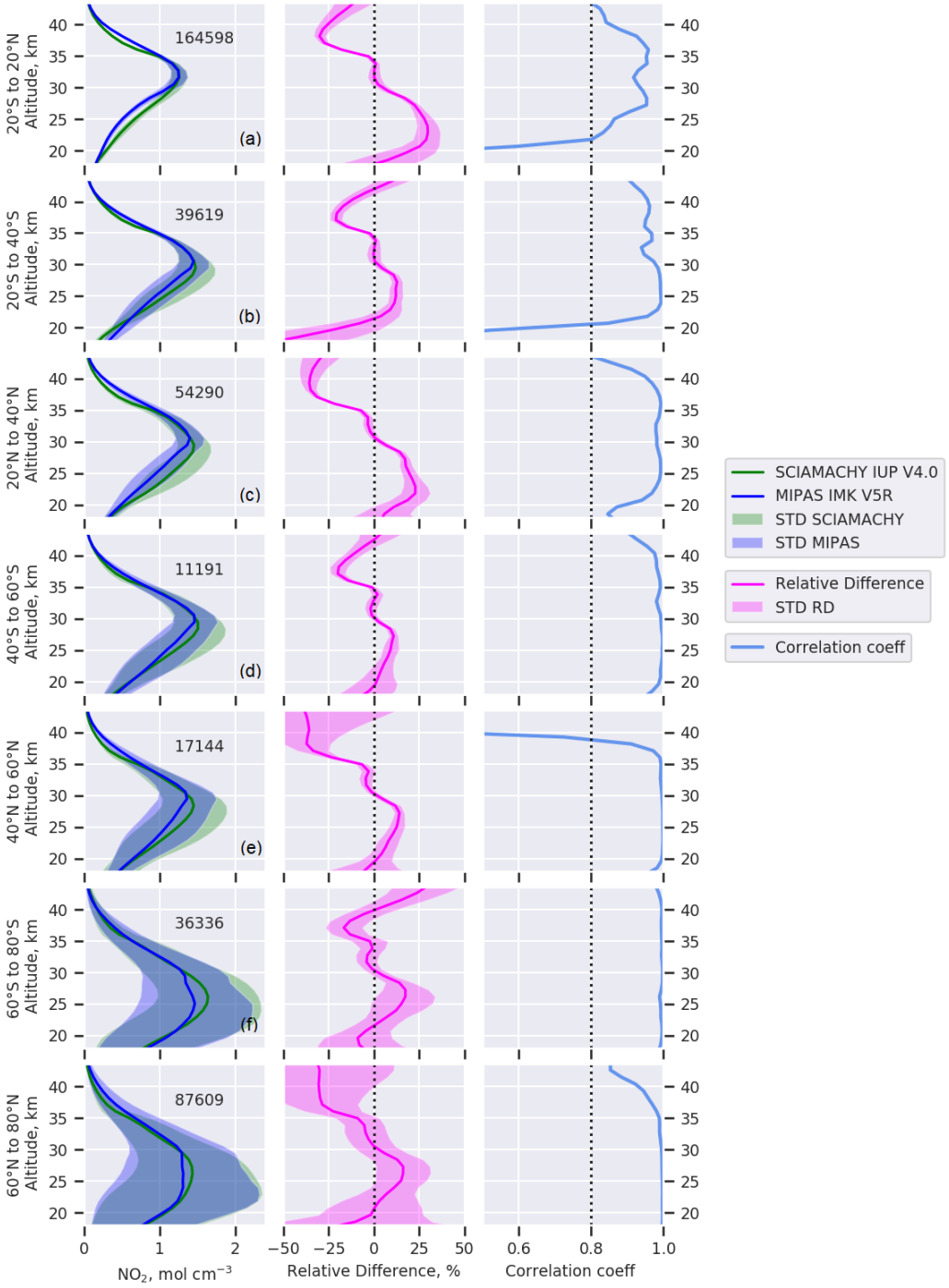

Figure 9.10: Same as Fig. 9.1, but for SCIAMACHY IUP V4.0 NO_2 (green) and MIPAS IMK-IAA V5R NO_2 (blue) measurements for the period of 2005-2012.

The correlation between the SCIAMACHY IUP and MIPAS IMK-IAA NO_2 data sets is high at all analysed latitudes, especially in the tropics and at the middle latitudes in comparison with the previous analysis, shown in Fig. 9.7. However, the correlation declines from high to moderate in the tropical region and at the middle latitudes I SH (panels a and b) below 21 km and at the middle latitudes II NH (panel e) above 39 km. Overall, the correlation between the SCIAMACHY IUP and MIPAS IMK-IAA data sets is higher than between SCIAMACHY IUP and MIPAS ESA, analysed in the previous section.

Figure 9.11 shows the time series of NO_2, similar to Fig. 9.8, but here blue stands for the MIPAS IMK-IAA data set.

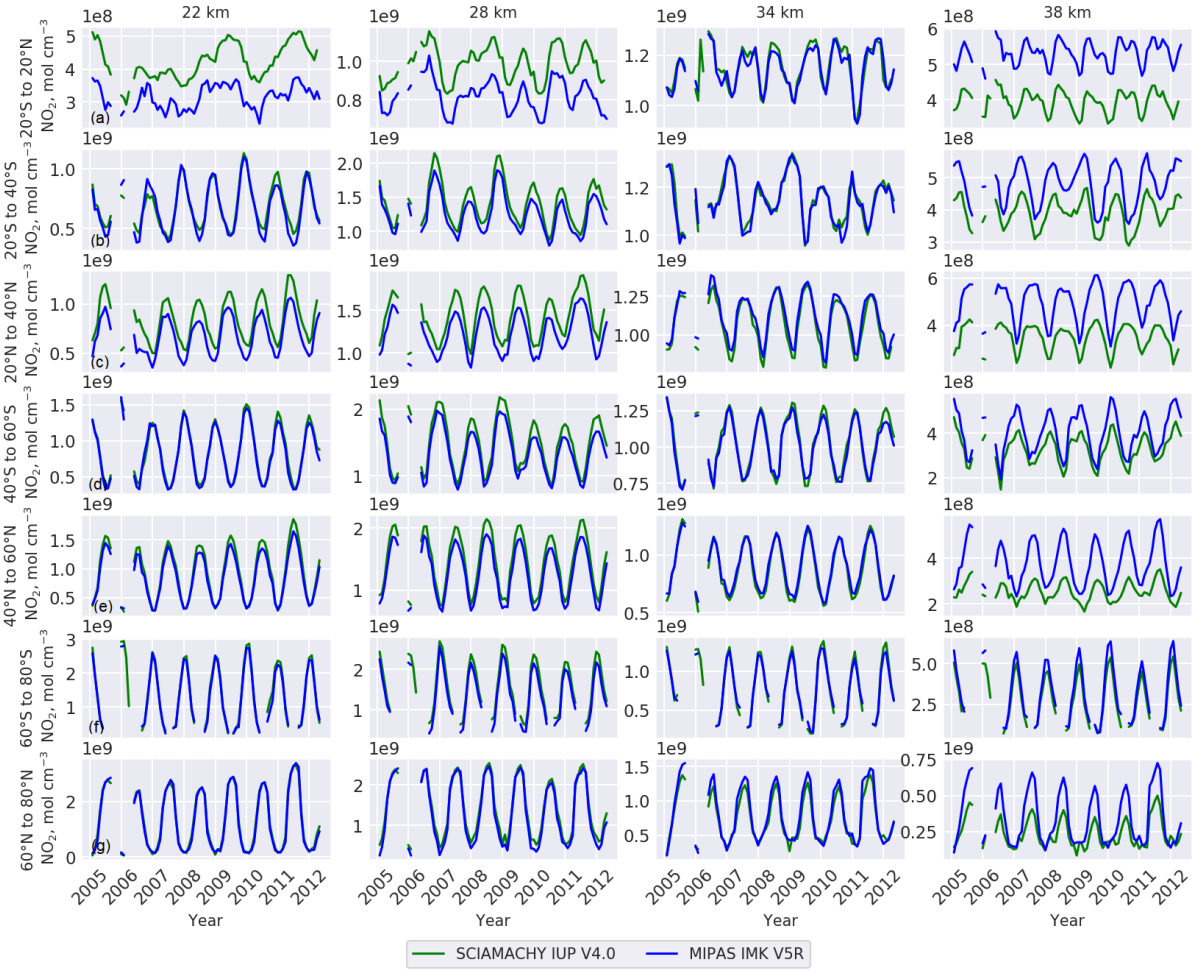

Figure 9.11: Same as Fig. 9.2, but for SCIAMACHY IUP V4.0 NO_2 (green) and MIPAS IMK V5R NO_2 (blue) measurements for the period of 2005-2012.

In the tropical region at 22 and 28 km (panel a) SCIAMACHY IUP shows higher NO_2 content, which was also shown in Fig. 9.10a; however, the seasonal cycle is similar in both data sets. Similar variations are observed at the middle latitudes I and II of both hemispheres at 28 km altitude (panels b-e). At 34 km altitude both data sets agree well; however, at 38 km SCIAMACHY IUP shows lower NO_2 content and lower seasonal variability in comparison with MIPAS IMK-IAA data set. Similar patterns were also observed while comparing SCIAMACHY IUP and MIPAS ESA (see Fig. 9.8). At the high latitudes (panels f and g) SCIAMACHY IUP agrees well with the MIPAS data set at 22 km altitude; at 28 km SCIAMACHY IUP suggest somewhat higher NO_2 content; at 34 and 38 km SCIAMACHY shows lower NO_2 content. Moreover, at 38 km SCIAMACHY IUP shows less NO_2 in comparison with the MIPAS IMK-IAA data set at all latitude bands.

Figure 9.12 shows the RDs between the SCIAMACHY IUP and MIPAS IMK-IAA data sets. Overall, the RDs between them are much smaller than between SCIAMACHY IUP and MIPAS ESA (compare Fig. 9.9), suggesting a better agreement.

Figure 9.12: Same as Fig. 9.3, but for SCIAMACHY IUP V4.0 and MIPAS IMK V5R NO_2 measurements for the period of 2005-2012.

For example, Fig. 9.12 shows that in the topical region (panel a) and at the middle latitudes I (panel b) at 34 km altitude the RD between SCIAMACHY IUP and MIPAS IMK-IAA varies

mostly within ± 1-3%. At the middle latitudes I at the altitude of 28 km the RD varies within around 2-22%; at 22 km altitude the RD changes within higher amplitude of ± 40%; at 38 km the RD changes from around -20 to -40%. At the middle latitudes II (panel c) the agreement between the data sets is similar to the middle latitudes I (panel b), or even better, e.g. at the altitude of 22 km the RD changes within ± 20%. At the high latitudes (panel d) at 22 and 38 km altitude the RD changes within ± 40%, at 28 km from 0 to 40%, and at 34 km is mostly within ± 20%. Interestingly, at lower altitudes at 22 km the RDs are much smaller than those shown for MIPAS ESA retrieval at all latitudes (see Fig. 9.9). However, in the tropical region at 38 km altitude the RD from the comparison of SCIAMACHY IUP with MIPAS IMK-IAA is higher, than with MIPAS ESA.

9.2 Photochemical correction of occultation data

As discussed in Sect. 4.3.4, the SAGE II satellite instrument operated in the occultation geometry, i.e. took measurements at the local sunrise and sunset. Therefore, in order to compare its NO_2 profiles with those measured by SCIAMACHY, they were photochemically corrected to match the illumination conditions of SCIAMACHY measurements with the application of the TOMCAT 3-D and 1-D models (see also Fig. 6.5).

9.2.1 SAGE II V7.0

Here only the sunset SAGE II NO_2 profiles were considered for comparison, as the sunrise measurements were reported to be of lower quality and less reliable (Damadeo et al., 2013), thus, scientifically less robust. The comparison of SCIAMACHY IUP V4.0 and SAGE II V7.0 NO_2 profiles (Fig. 9.13) is similar to the previous profiles comparisons, shown in Fig. 9.1, 9.4, 9.7, and 9.10. The spatio-temporal criteria of co-located profiles was set to 500 km and 8 hours during the period of 2002-2005. Similar to Gebhardt et al. (2014), no co-located sunset profiles were found at high latitudes SH.

As seen in Fig. 9.13, SCIAMACHY IUP retrieval shows lower NO_2 content in comparison with photochemically corrected SAGE II profiles at almost all altitude and latitude bands. In the tropical region and at the middle latitudes (see panels a-d) the agreement between the data sets is the best at around 30-35 km altitude, where the RD is around ± 2%, except at the middle latitudes II NH (panel e), where the RD exceeds 15% at all altitudes. At the high NH latitudes (panel f) the agreement between SCIAMACHY IUP and SAGE II is also good, i.e. the RD does

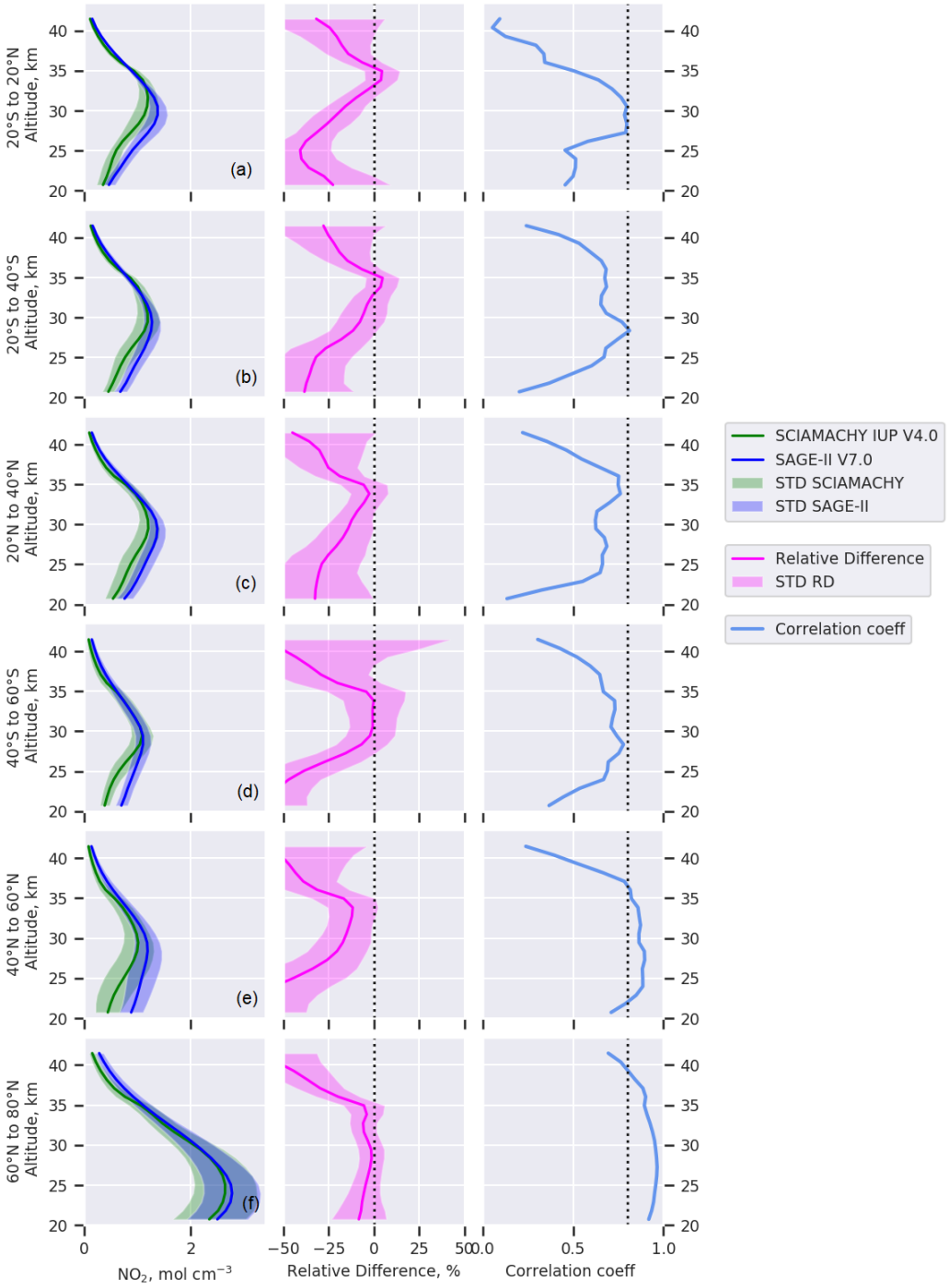

Figure 9.13: Same as Fig. 9.1, but for SCIAMACHY IUP V4.0 NO_2 (green) and SAGE II V7.0 sunset NO_2 (blue) measurements for the period of 2002-2005.

not exceed 5% in the altitude range of 25-35 km; above 35 km the RD increases with altitude. The correlation between the two data sets is high at the middle latitudes II NH (panel e) at the altitude range of 23-37 km and at the high NH latitudes (panel f) in the altitude range 20-40 km. At all other latitudes the correlation is moderate at the altitude range of around 23-40 km. The agreement of NO_2 data sets between SCIAMACHY IUP retrieval V4.0 and SAGE II V7.0 is much better at all latitude bands, than e.g. the agreement between SCIAMACHY ESA retrieval V6.01 and SAGE II V7.0, shown in (Galytska et al., 2017, Fig.12).

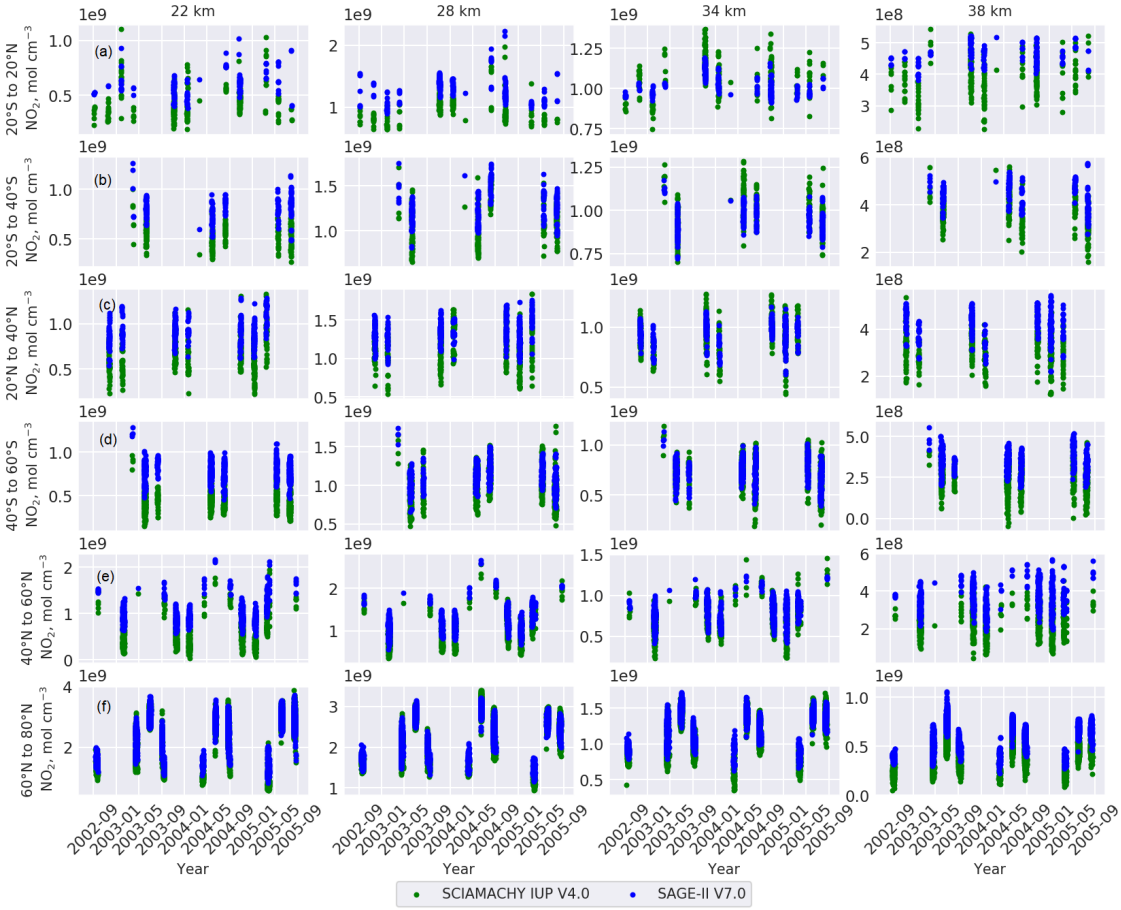

Figure 9.14: Same as Fig. 9.2, but for SCIAMACHY IUP V4.0 NO_2 (green) and SAGE II V7.0 sunset NO_2 (blue) measurements for the period of 2002-2005.

The analysis of seasonal changes for the SCIAMACHY IUP and SAGE II measurements is a challenging task due to a limited number of co-locations between the two data sets during the period of August 2002-August 2005. Therefore, Fig. 9.14 shows plots of NO_2 from SCIAMACHY IUP (green) and SAGE II (blue).

The underestimation of stratospheric NO_2 content by SCIAMACHY in comparison with photochemically corrected SAGE II measurements is seen at all latitude bands at the altitudes of 22, 28, and 38 km. However, both data sets agree well on seasonal variations of NO_2 in the stratosphere. The agreement of SCIAMACHY IUP and SAGE II data is best at 34 km altitude, where the spread of the data points is very similar between the two instruments.

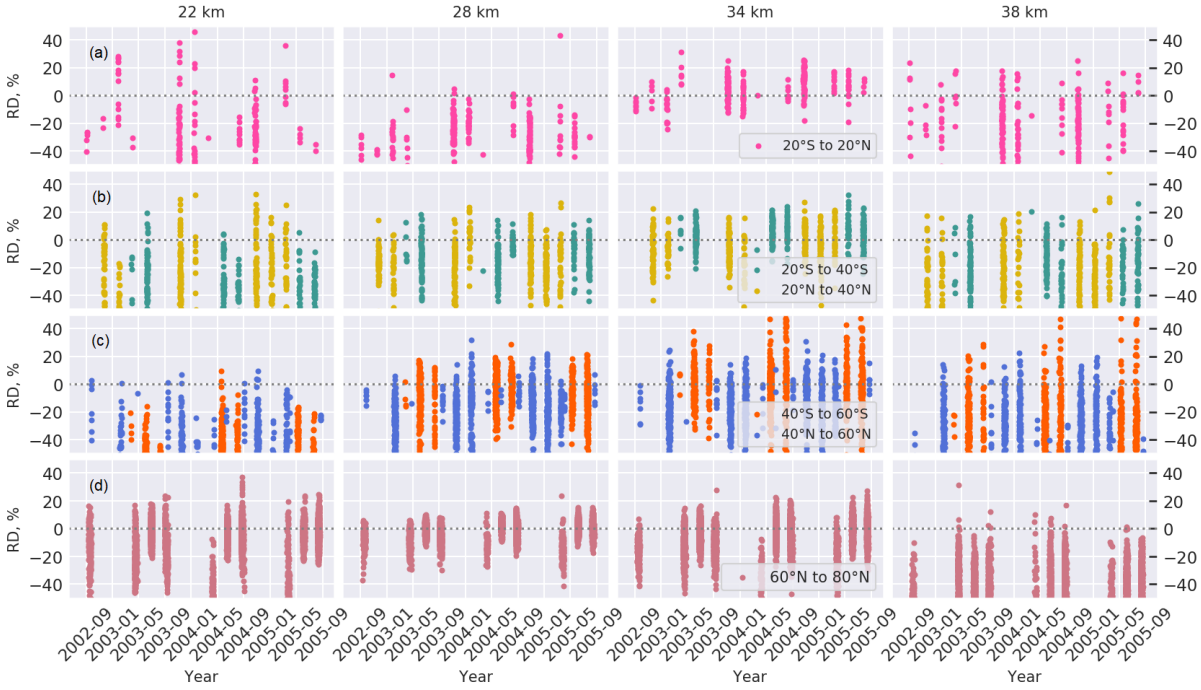

Figure 9.15: Same as Fig. 9.3, but for SCIAMACHY IUP V4.0 and SAGE II V7.0 sunset NO_2 measurements for the period of 2002-2005.

Figure 9.15 shows scatter plots of the RD between the two data sets at different altitudes and latitudes. The lowest RDs (within ± 20%) are observed in the tropical region (panel a) at 34 km altitude and at the high latitudes NH (panel d) at 28 km. There is a persistent underestimation of NO_2 by SCIAMACHY IUP in comparison with SAGE II data with an RD from 0 to -40% at the middle latitudes II (panel c) at 22 km, in the tropical region (panel a) at 28 km, and at the high latitudes NH (panel d) at 38 km altitude. In other regions the RD mostly varies within ± 40%.

10

Long-term changes in stratospheric constituents

10.1 Observed and simulated changes in atmospheric constituents

As discussed in Sect. 2.1, O_3 plays a significant role in the chemistry of the atmosphere, although in terms of abundance it belongs to minor atmospheric constituents. Several publications have documented a significant O_3 decrease during the first decade of the 2000s in the tropical middle stratosphere (e.g. Kyrölä et al., 2013; Eckert et al., 2014; Gebhardt et al., 2014; Nedoluha et al., 2015b), where it is chemically formed via the Chapman mechanism (described in Sect. 2.1.1). The pioneering studies of Kyrölä et al. (2013) and Gebhardt et al. (2014) analysed O_3 changes using different data sets during similar time periods. Kyrölä et al. (2013, Fig.15) showed a statistically significant O_3 decline of around 2-4% per decade in the tropical region (10°S-10°N) at 30-35 km altitude for the period 1997-2011 from the combined SAGE II and GOMOS dataset. In turn, Gebhardt et al. (2014, Fig.8) identified a much stronger O_3 decline of up to 18% per decade at the same altitudes and latitudes for the period August 2002-April 2012 from SCIAMACHY observations. In addition, Gebhardt et al. (2014) suggested a possible connection of O_3 decline with the increase in NO_x (first presented at the Quadrennial Ozone Symposium 2012). Eckert et al. (2014) reported decline of O_3 in the tropics in the form of a double-peak structure at around 25 and 35 km from MIPAS measurements during the period 2002-2012. However, the reasons for the observed O_3 decline remained unclear, and Eckert et al. (2014) stated that the changes in upwelling explain neither the observed negative O_3 trends nor their double-peak structure.

The findings of Nedoluha et al. (2015b) were the most relevant to describe observed changes in the tropical middle stratosphere. They showed a significant decline in O_3 at 30-35 km altitude in the tropics by using the HALOE (1991-2005) and NASA Aura MLS (2004-2013) data. They linked the decline of O_3 with a long-term increase in NO_y species, and related their increase to changes in N_2O transport from the troposphere. In particular, Nedoluha et al. (2015b) showed that the decrease in N_2O is "likely linked to long-term variations in dynamics". By applying a 2D chemical-dynamical model they showed that changes in the tropical upwelling could lead to changes in the N_2O oxidation via Reaction (R20a) and therefore could affect the production of NO_y. Based on this, Nedoluha et al. (2015b) concluded that weaker tropical upwelling could explain the O_3 decline in the tropical middle stratosphere. However, the authors did not show that such dynamical perturbations indeed exist in the BDC. The changes in the strength of different branches of BDC were analysed by Aschmann et al. (2014). They used diabatic heating calculations from the ECMWF Era-Interim data set. They concluded that "there are strong indications that the observed trend-change in O_3 is primarily a consequence of a simultaneous trend-change in tropical upwelling". The conclusions of both Aschmann et al. (2014) and Nedoluha et al. (2015b) agree with the finding of Shepherd (2007), who showed that stratospheric O_3 is affected by changes in transport patterns, which in turn are associated with changes in Rossby-wave forcing.

The most recent publications with extended data records suggest that there are signs of O_3 recovery in the tropical middle stratosphere. For example, Sofieva et al. (2017) showed only a small decline of O_3 (2% per decade) by analysing merged SAGE II, ESA Ozone Climate Change Initiative (Ozone_cci), and Ozone Mapping Profiler Suite (OMPS) data sets for the period 1997-2016. Steinbrecht et al. (2017) analysed seven merged data sets and concluded that there are no clear indications for O_3 changes in the tropics during 2000-2016. Ball et al. (2018) highlighted that the observed decrease in O_3 at 32-36 km is primarily due to high O_3 during the 2000-2003 period and they did not report negative O_3 changes during 1986-2016. Positive O_3 changes in the tropical stratosphere above around 30 km altitude were shown in the research of Chipperfield et al. (2018, Fig. 3) for the period 2004-2017 from MLS measurements and simulations of the TOMCAT CTM. While there are clear signs of recent recovery of the stratospheric ozone layer (Chipperfield et al., 2017), full explanations of observed O_3 decline in the tropical middle stratosphere within the first decade of the 21st century have not been provided.

In the current research, the analysis of changes in the tropical middle stratosphere based on the updated SCIAMACHY O_3 and NO_2 data sets during 2004-2012 was done, similar to the period analysed by Kyrölä et al. (2013); Eckert et al. (2014); Gebhardt et al. (2014); Nedoluha et al. (2015b). However, in contrast to those studies, here SCIAMACHY measurements are combined and compared with simulations of TOMCAT CTM with different chemical and dynamical forcings (see Sect. 5.3.1) to diagnose the primary causes of O_3 and NO_2 changes. Based on the modelled AoA, seasonal changes in the deep branch of BDC are revealed. This study provides the explanation of how month-to-month transport changes affect N_2O chemistry, which consequently leads to observed O_3 decline. The temporal evolution of chemical compounds was analysed by application of MLR technique, described in Sect. 7. In addition to constant and linear terms, annual and semi-annual variations, the MLR also takes into account ENSO and QBO. In addition to the above-mentioned proxies, the linear changes were calculated for both cases, with and without a solar cycle term ($SC(t)$ in Eq. 7.1, see Sect. 7). The results with and without the solar cycle term are very similar. Therefore, only results from MLR without a solar cycle term are shown below. The use of noise autocorrelation does not add any information when calculating the value of linear changes for selected monthly time series. Consequently, to maintain consistency, it was also ignored when determining the linear changes from the complete time series. Below, the term "changes" instead of "trends" is applied to the observed variations in chemical compounds in the middle stratosphere, as the analysed time span is not long enough. Some of the results on observed and simulated changes from SCIAMACHY and TOMCAT were published in Galytska et al. (2019a).

Linear changes in O_3 and NO_2 zonal monthly mean values from SCIAMACHY measurements (see Sect. 4.3.1) as a function of latitude and altitude over the period January 2004-April 2012 are shown in Fig. 10.1. Hatched areas show regions where changes are statistically significant at the 2σ level. The dashed rectangles indicate the region of the tropical middle stratosphere, on which the current study is focused. Statistically significant positive O_3 changes of around 6% per decade are observed at southern mid-latitudes (20-50°S) at altitudes around 27-31 km (Fig. 10.1a), which are in agreement with O_3 trends from MLS for the period 2004-2013 shown by Nedoluha et al. (2015b). Significant positive O_3 changes are seen in the tropical lower stratosphere below 22 km altitude, which agree well with findings of Gebhardt et al. (2014) and Eckert et al. (2014). In the tropical middle stratosphere a statistically significant O_3 decline of 12% per decade is observed, which is consistent with findings of Gebhardt et al. (2014), who used SCIAMACHY version 2.9 O_3 data. Applied in this study, SCIAMACHY version 3.5 O_3

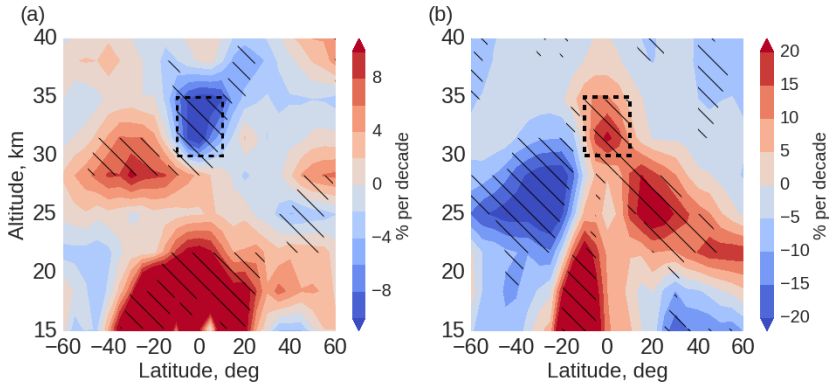

Figure 10.1: Latitude-altitude distribution of (a) O_3 and (b) NO_2 changes (% per decade) from SCIAMACHY measurements for January 2004-April 2012. Hatched areas show changes significant at the 2σ level. The dashed rectangle indicates the region of the tropical middle stratosphere, which is in the focus of this study.

data employ an updated retrieval approach in the visible spectral range (Jia et al., 2015), which shows much less drift in comparison to older data versions. The observed negative O_3 changes are also in agreement with Kyrölä et al. (2013), Eckert et al. (2014), Nedoluha et al. (2015b), Sofieva et al. (2017). Figure 10.1b shows a strong positive change in NO_2 of around 20% per decade in the region of the tropical middle stratosphere.

To identify possible reasons for the observed O_3 decline in the tropical middle stratosphere, and to assess the role of N_2O and NO_x chemistry in these changes following suggestions by Nedoluha et al. (2015b), the data from three TOMCAT simulations (see Sect. 5.3.1) were analysed. Figure 10.2 shows linear changes as the function of latitude and altitude for O_3 (panels a-c), NO_2 (panels d-f), NO_x (panels g-i), and NO_y (panels j-l) for the period January 2004-April 2012 from TOMCAT for (1) control run (CNTL) in the left column, (2) run with constant tropospheric mixing ratios of source gases (fSG) in the middle column, and (3) run with annually repeating meteorology (fDYN) in the right column. Results are presented on the native TOMCAT vertical grid. The CNTL simulation shows negative O_3 changes in the tropical middle stratosphere (Fig. 10.2a) of up to 9% per decade and positive NO_2 changes (Fig. 10.2d) of around 12-14% per decade, which are similar by shape, but smaller by value than changes observed by SCIAMACHY (Fig. 10.1a,b). Both NO_x and NO_y changes are also very similar to observed NO_2 positive changes. This indicates that the observed positive NO_2 changes are mostly due to positive NO_y and therefore NO_x changes.

To separate the influence of the stratospheric dynamics on O_3, NO_2, NO_x, and NO_y changes

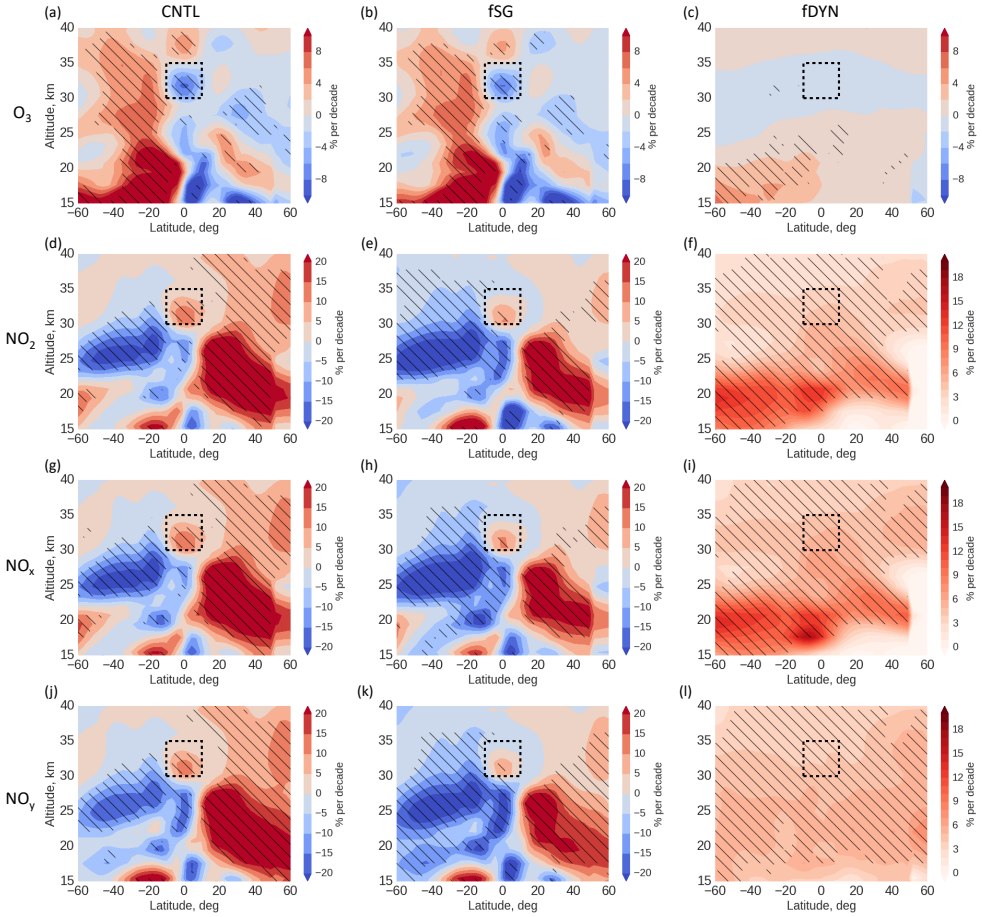

Figure 10.2: Latitude-altitude distribution of (a-c) O_3, (d-f) NO_2, (g-i) NO_x, and (j-l) NO_y changes (% per decade) from TOMCAT runs for January 2004-April 2012 period: CNTL (left column), fSG (middle column), and fDYN (right column). Hatched areas show changes significant at the 2σ level. The dashed rectangles indicate the region of the tropical middle stratosphere.

in the tropical middle stratosphere, the middle column of Fig. 10.2 shows the TOMCAT fSG simulation with fixed tropospheric mixing ratios of all tropospheric source gases. The modelled changes from both runs CNTL and fSG are very similar for O_3 (Fig. 10.2a,b), NO_2 (Fig. 10.2d,e), NO_x (Fig. 10.2g,h), and NO_y (Fig. 10.2j,k). This shows that the observed changes in the tropical middle stratosphere are mostly driven by dynamics. The TOMCAT fDYN simulation, with annually repeating meteorology, shows insignificant negative changes in O_3 (Fig. 10.2c). There is a statistically significant but very weak positive change in NO_2 (Fig. 10.2f) similar to NO_x(Fig. 10.2i) and NO_y (Fig. 10.2l) species in the tropical middle stratosphere of around 3% per decade. The TOMCAT fDYN simulation shows that the direct

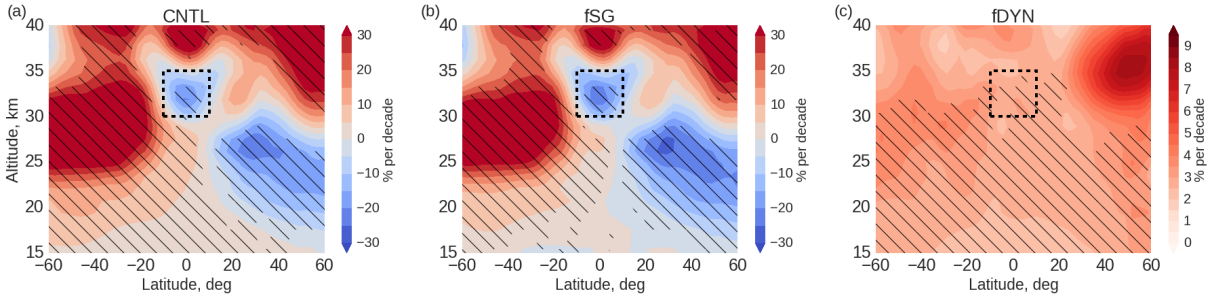

Figure 10.3: Latitude-altitude distribution of (a-c) N_2O changes (% per decade) from TOMCAT runs for January 2004-April 2012 period: CNTL (a), fSG (b), and fDYN (c), similar to Fig. 10.2.

impact of the chemistry on the observed variations in O_3, NO_y, NO_x, and NO_2 is small.

Similar to Fig. 10.2, Fig. 10.3 shows linear changes in N_2O as the function of latitude and altitude from TOMCAT runs. The CNTL simulation (Fig. 10.3a) shows statistically significant N_2O decrease of around 20% per decade in the tropical middle stratosphere and pronounced hemispheric asymmetry with positive changes at southern and negative changes at northern mid-latitudes. These changes agree well with the negative N_2O trends in the equatorial region from MLS during 2004-2013, reported by Nedoluha et al. (2015a, Fig. 10). Such variations in N_2O, a long-lived tracer with a global lifetime of around 115-120 years (Portmann et al., 2012), might indicate possible changes in the deep branch of the BDC. This is confirmed by Fig. 10.3b, where N_2O changes (24% per decade) in conditions of variable dynamics but fixed source gases conform changes shown in the full chemistry simulation (Fig. 10.3a). However, relatively small but statistically significant positive N_2O change of around 3% per decade in the fDYN run (Fig. 10.3c) represent the existing tropospheric trend in conditions of unchanged dynamics.

Additionally, the analysis of BrO variations in the stratosphere was also performed. Figure 10.4 shows linear changes in BrO as the function of latitude and altitude for the same period as in Fig. 10.3. Panels in Fig. 10.4 show results from the MLR model applied to different data sources: (a) SCIAMACHY measurements, (b-d) TOMCAT runs CNTL, fSG, and fDYN accordingly. SCIAMACHY measurements show a pronounced increase in BrO of 15% per decade in the tropics and middle latitudes up to 22 km altitude; above 26 km in the tropical region there is a decline of BrO of around 5% per decade (not statistically significant. In contrast to SCIAMACHY measurements, TOMCAT CNTL run (panel b) shows statistically significant negative BrO changes in the stratosphere, with the maximum decline in the tropical region between 18 and 26 km (10-15% per decade). In the fSG TOMCAT simulation (panel

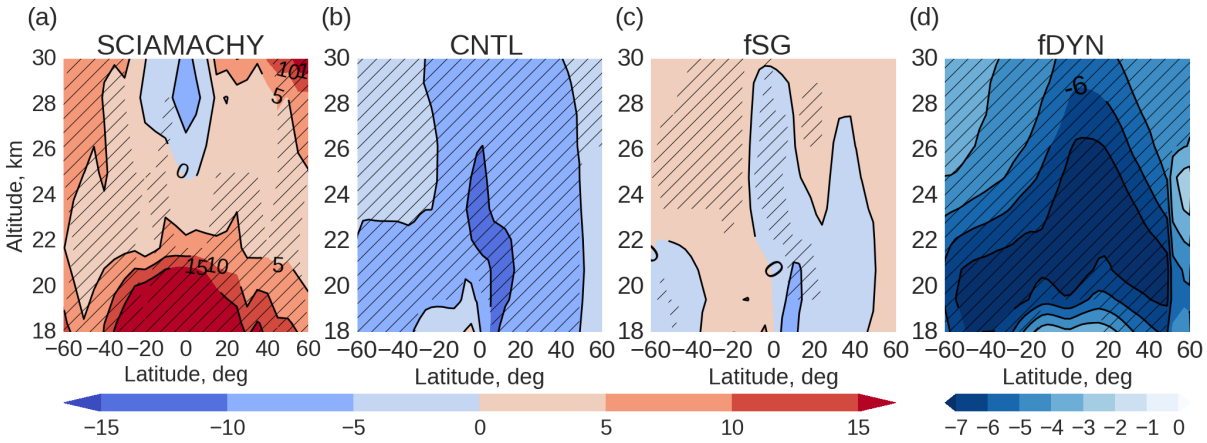

Figure 10.4: Latitude-altitude distribution of BrO changes (% per decade) from SCIAMACHY measurements (a) and TOMCAT runs: CNTL (b), fSG (c), and fDYN (d) for the period January 2004-April 2012.

c) negative BrO changes persist in the tropical region, but with somewhat lower values of around 0-5% per decade. TOMCAT simulation fDYN (panel d) shows pronounced negative BrO changes in the stratosphere in conditions of unchanged stratospheric dynamics. Because the BrO changes in the stratosphere between SCIAMACHY (panel a) and CNTL simulation of TOMCAT (panel b) do not agree, further investigations of the reasons for the disagreement are needed. Therefore, BrO data are not considered in the further analysis.

10.2 Tropical middle stratospheric correlations

A powerful diagnostic for identifying the impact of chemical and dynamical processes on specific stratospheric constituents is provided by tracer-tracer correlation plots (e.g. Sankey and Shepherd, 2003; Hegglin and Shepherd, 2007; Galytska et al., 2019a). Figure 10.5 shows correlation plots of monthly mean N_2O versus NO_2 (panel a) and N_2O versus O_3 (panel b) data over the period January 2004-April 2012 in the tropical middle stratosphere from the TOMCAT run CNTL. The colour coding stands for altitude: 31 km (orange), 32 km (blue), 33.5 km (magenta), and 35 km (green). Due to the long lifetime of N_2O, its values reflect transport patterns: low N_2O values indicate older air and high N_2O values younger air. The N_2O-NO_2 anti-correlation (Fig. 10.5) results from N_2O chemical loss to produce NO_2 via Reactions (R20a) and (R21). In particular, when the tropical upwelling accelerates, more N_2O is transported from the troposphere, but less NO_2 (and therefore NO_y) is formed as the residence time of N_2O decreases,

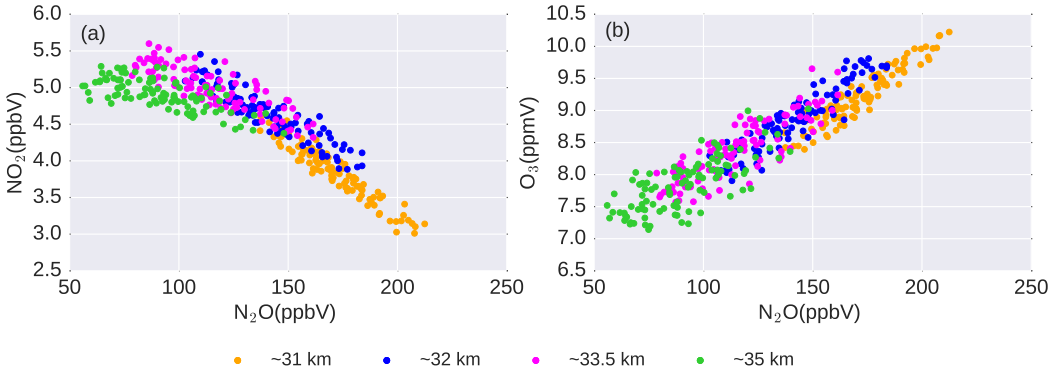

Figure 10.5: Scatter plots of monthly mean (a) N_2O versus NO_2 and (b) N_2O versus O_3 in the tropical middle stratosphere during January 2004-April 2012 from TOMCAT simulation CNTL. The colour coding indicates the altitude of: 31 km (orange), 32 km (blue), 33.5 km (magenta), and 35 km (green).

i.e. there is less time to produce NO_2 from Reactions (R20a) and (R21). In contrast, when the tropical upwelling is slower, less N_2O is transported to the middle stratosphere, however its residence time becomes longer, which results in an increased NO_2 production. Figure 10.5a shows a larger abundance of N_2O observed at 31 km (160-200 ppbV) than at 35 km (50-140 ppbV). This is related to the time needed to transport air masses between the two altitudes. This in turn favours higher NO_2 amounts at 35 km of around 4.5-5.5 ppbV in comparison with 3-4.5 ppbV at 31 km. Figure 10.5a also shows that the anti-correlation between N_2O and NO_2 reduces with higher altitude, i.e. at 35 km (green) it is almost flat. This is because at altitudes above 34-35 km, the produced NO via Reaction (R20a) reacts rapidly with N (e.g. NO + N $\rightarrow$ N_2 +O) which converts NO back to N_2. The NO_2 produced from the oxidation of N_2O via Reaction (R20a) impacts O_3. Figure 10.5b shows the correlation between N_2O and O_3. There is a linear relation, as the lifetime of both tracers in this region is greater than their vertical transport timescales (Bönisch et al., 2011). Both panels of Fig. 10.5 show quite compact correlations between the tracers, which indicate well mixed air masses (Hegglin et al., 2006).

To obtain more detailed information about tracer distributions, in particular on the NO_2 impact on the observed negative O_3 change, Fig.10.6 shows NO_2-O_3 scatter plots at 31.5 km (upper panels) and at 34.8 km (lower panels) in the tropical region from SCIAMACHY measurements (blue) and TOMCAT simulations: CNTL (green), fSG (yellow) and fDYN (pink). Data points represent zonal monthly mean values during January 2004-April 2012. TOMCAT data are interpolated to the SCIAMACHY vertical grid. Solid lines in each panel depict linear

fits to the data points and show O_3-NO_2 chemical link. All panels of Fig. 10.6 show expected anti-correlation of O_3 and NO_2. The SCIAMACHY NO_2-O_3 distributions at 31.5 km (Fig. 10.6a) and 34.8 km (Fig. 10.6e) agree well with corresponding TOMCAT CNTL simulation (Fig. 10.6b,f), although modelled NO_2 and O_3 are lower in comparison with measurements.

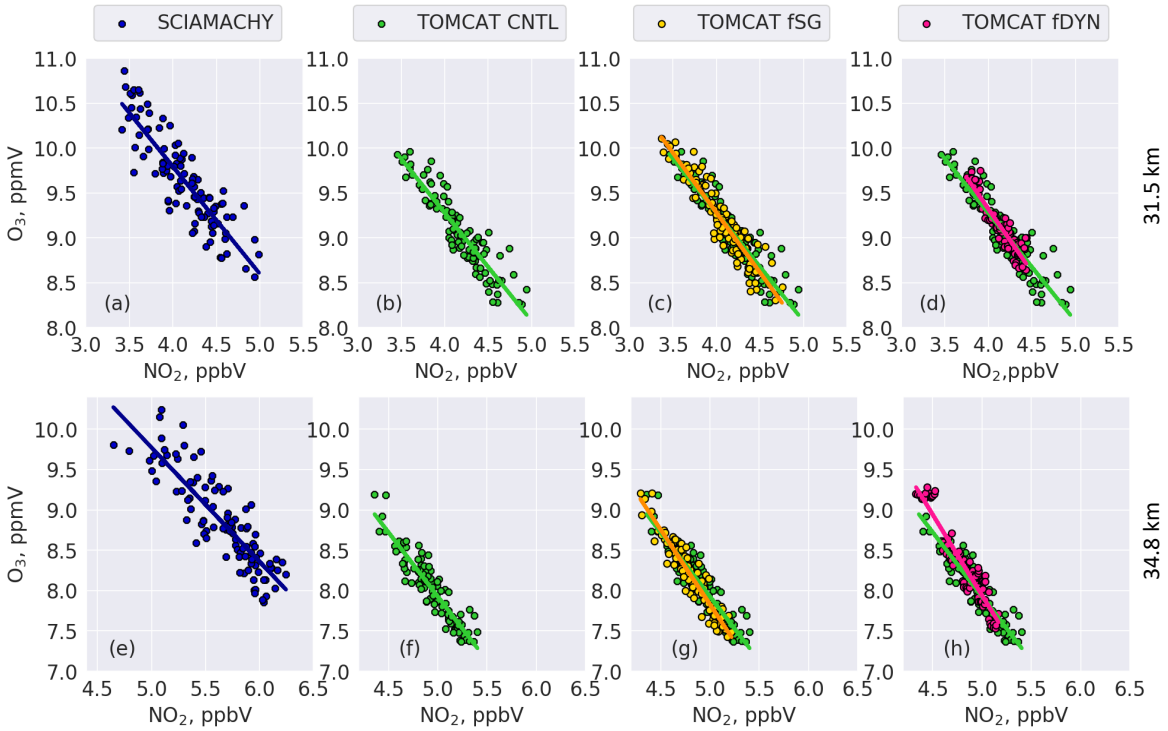

Figure 10.6: NO_2-O_3 scatter plots in the tropical middle stratosphere from (a,e) SCIAMACHY and TOMCAT simulations (b,f) CNTL, (c,g) CNTL and fSG, and (d,h) CNTL and fDYN at the altitudes of 31.5 km (upper panels) and 34.8 km (lower panels). Colour coding denotes data source: SCIAMACHY (blue), TOMCAT: CNTL (green), fSG (yellow), fDYN (pink). Solid lines depict linear fits to the data points.

Figure 10.6c shows a combined scatter plot from both simulations CNTL and fSG and further represents the impact of dynamics on NO_2-O_3 changes. In conditions of unchanged tropospheric mixing ratios of source gases (fSG), the data scatter and slopes do not change significantly in comparison with the control simulation (CNTL). Similar results are seen at altitude of 34.8 km (Fig. 10.6g). Both simulations CNTL and fSG are performed with the same dynamical forcing. In contrast, the NO_2-O_3 scatter from CNTL and fDYN TOMCAT simulations (Fig. 10.6d,h) differ substantially. In the absence of dynamical changes (fDYN) the NO_2 and O_3 scatter do not show such pronounced variability as in the CNTL simulation, which shows the

impact of transport and indicates different distributions of tracers with and without dynamical changes. Nevertheless, the slopes are very similar in both simulations, which illustrates the chemical impact of NO_x changes on O_3. Therefore, the NO_2-O_3 scatter plots from the model calculations confirm that observed O_3 changes are linked to NO_x chemistry in the tropical middle stratosphere.

Recognizing the tight relationships within the tropical middle stratosphere N_2O-NO_x-O_3 chemistry, seen in Figs. 10.5 and 10.6, we calculated correlation coefficients, including the dynamical AoA tracer. Figure 10.7 shows the correlation heat map for AoA, N_2O, NO_y, NO_x, NO, NO_2, and O_3 for the period January 2004-April 2012 in this region.

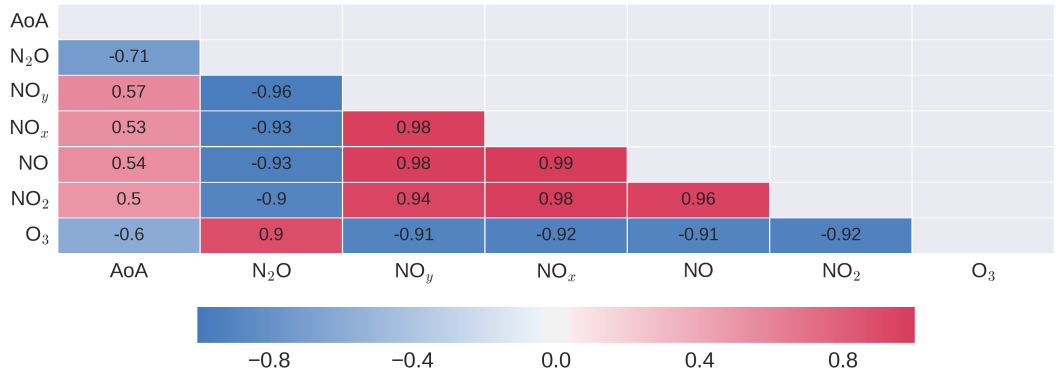

Figure 10.7: Correlation heat map for AoA, N_2O, NO_y, NO_x, NO, NO_2, and O_3 from TOMCAT CNTL run for the period January 2004-April 2012 in the tropical middle stratosphere. Repeated information is excluded from the heat map.

The (anti-)correlations between the chemical species N_2O, NO_y, NO_x, NO, NO_2, and O_3 are very high and exceed an absolute value of 0.9. This is consistent with tracer-tracer correlations shown in Figs. 10.5a,b and 10.6a-h. The value of anti-correlation for N_2O-O_3 is lower in comparison with that for NO_2-O_3. Such differences in (anti-)correlations are explained by the overall regulation of O_3 abundance in the tropical middle stratosphere. Ozone is mainly destroyed by NO_x in this altitude region and the strong chemical link between O_3 and $NO_y/NO_x/NO_2/NO$ is confirmed by the high anti-correlation (0.91-0.92). A strong anti-correlation is expected between N_2O and NO_y (0.96) as they are long-lived tracers in the middle stratosphere, and N_2O is the source of NO_y and NO_x species. As the amount of NO_x also scales with the amount of NO_y, a strong correlation (0.9) exists between N_2O and O_3, even in the middle stratosphere where the

photochemical lifetime of O_3 becomes short. The (anti-)correlation of AoA with all tracers is rather moderate (with absolute values within the range of 0.5-0.71), as stratospheric transport (or AoA) does not directly control NO_2, NO, NO_x, NO_y, and O_3. The unexpected finding is that the anti-correlation between N_2O and AoA is also only moderate (0.71). As the major source of the tropical middle stratospheric N_2O is the upwelling from lower altitudes (see Sect. 2.2.1), a higher anti-correlation between AoA and N_2O would be expected.

10.3 Relationship between N_2O and Age of Air

To investigate changes in AoA and further link them with those of N_2O, Fig. 10.8 shows (a) zonally averaged climatological mean AoA (years) and (b) AoA linear changes (years per decade) as a function of latitude in the stratosphere from TOMCAT CNTL simulation during January 2004-April 2012. AoA is shown on the native TOMCAT vertical grid. The dashed rectangles indicate the region of interest in the tropical middle stratosphere.

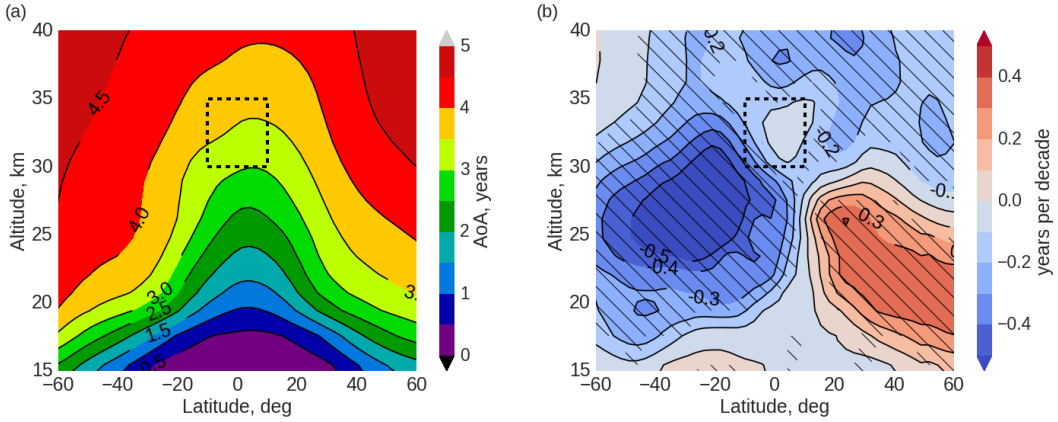

Figure 10.8: Latitude-altitude AoA (a) zonally averaged distribution (years), (b) linear changes (years per decade) from TOMCAT CNTL simulation during January 2004-April 2012, similar to Fig. 10.3. Taken from Galytska et al. (2019a, Fig. 8b).

According to Fig. 10.8a the AoA increases with altitude and is largest in the high latitudes at high altitudes. This AoA distribution results from the mechanism of BDC. The average AoA in the tropical middle stratosphere is between 3 and 3.6 years. Figure 10.8b shows that there is a statistically significant (hatched areas) decrease in AoA in SH between around 20-35 km and a statistically significant increase in NH at altitudes 15-30 km. This hemispheric asymmetry is in agreement with results presented in Sect. 10.1 for changes of N_2O as the long-lived tracer (Fig. 10.3a), and is in agreement with Mahieu et al. (2014, Fig. 4b) and Haenel et al. (2015). As was

shown by Galytska et al. (2019a, Fig.9), the hemispheric asymmetry remains unchanged within all seasons. In the tropical middle stratosphere no statistically significant changes in AoA are identified (Fig. 10.8b). The absence of statistically significant AoA changes in the considered region is on the one hand in agreement with Aschmann et al. (2014), who showed that the deep branch of BDC does not show significant changes. On the other hand, it is inconsistent: 1) with the identified negative changes in N_2O (see Fig. 10.3a) and 2) with conclusions of Nedoluha et al. (2015b), who suggested that a slowdown in the tropical upwelling can be a reason for O_3 decline at 30-35 km altitude.

To improve our understanding, Fig. 10.9 shows seasonal analysis of AoA linear changes (years per decade) during January 2004-April 2012 based on TOMCAT CNTL simulation for (a) DJF, (b) March-April-May (MAM), (c) June-July-August (JJA), and (d) September-October-November (SON). In comparison to the previous plots, Fig. 10.9 shows narrower latitude and altitude range, the dashed rectangles indicate the region of interest in the tropical middle stratosphere.

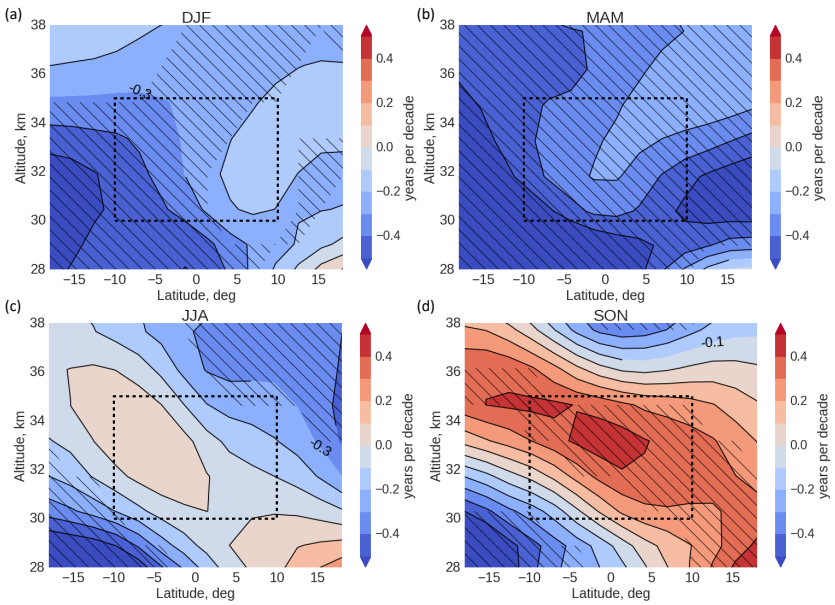

Figure 10.9: Latitude-altitude distribution of AoA changes (years per decade) from TOMCAT CNTL simulation during January 2004-April 2012 for (a) DJF, (b) MAM, (c) JJA, (d) SON. Hatched areas show changes significant at the 2σ level. The dashed rectangle indicates the region of the interest in the tropical middle stratosphere.

According to Fig. 10.9, AoA changes show strong seasonal variations in the tropical middle stratosphere. During DJFs and MAMs there is a statistically significant decrease in AoA (Fig. 10.9a,b). During JJAs the change is slightly positive, although insignificant, and during SONs there is a statistically significant increase (Fig. 10.9d). The observed seasonality in AoA changes in the tropical middle stratosphere averages to insignificant changes if the whole year is considered (seen in Fig. 10.8b).

From the above, the major resulting question is the following. How are transport (via AoA) and N_2O connected? To answer this question, Fig. 10.10 represents N_2O-AoA correlation coefficients as a function of month at altitudes 32 (yellow), 33 (pink), and 35 (green) km. To account for the hemispheric dependencies, the tropical region was split into southern (10°S-1°S, Fig. 10.10b) and northern (1°N-10°N, Fig. 10.10c) regions. Correlations were calculated on the native TOMCAT grid. Horizontal dashed lines indicate the lower edge of moderate correlation, which is represented by the absolute value of 0.6.

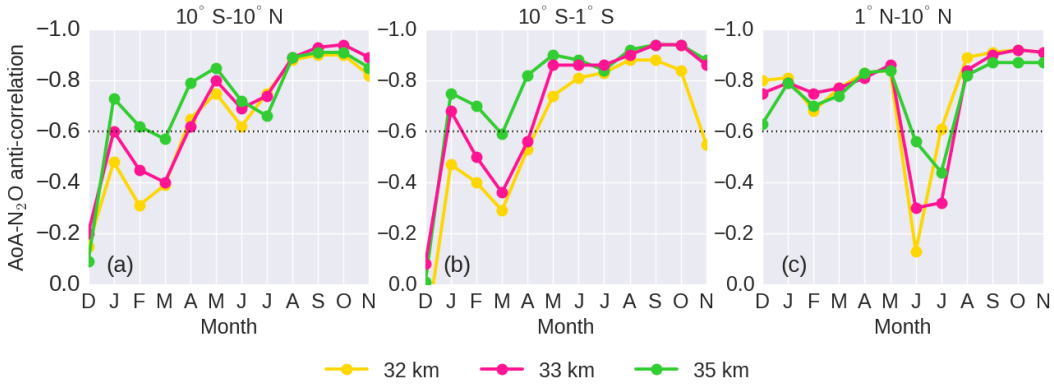

Figure 10.10: Anti-correlation between N_2O and AoA as a function of month averaged for the period January 2004-April 2012 for (a) 10°S-10°N, (b) 10°S-1°S, and (c) 1°N-10°N. Colour coding stands for altitude: 32 km (yellow), 33 km (pink), and 35 km (green). The dashed horizontal lines indicate the lower edge of moderate correlation, which was selected to be 0.6.

Figure 10.10a reveals that in the tropics (10°S-10°N) the anti-correlation between AoA and N_2O is low during December at the altitude of 35 km, and during December-March at 32 and 33 km altitude. During the other months of the year, it is moderate and reaches maximum (around 0.9) during late NH summer (August) and autumn (September, October) months. Very similar seasonal behaviour is also observed in the tropical region of the SH (Fig. 10.10b) with the minimum correlation during SH summer (December-March) and maximum during SH winter (May-October). In contrast, in the tropical region of the NH (Fig. 10.10c) a significant decrease

in AoA-N_2O correlation is observed during NH summer (June-July). Galytska et al. (2019a, Supplements, Fig. S3) showed that similar seasonal variations in N_2O-AoA anti-correlation are observed in narrower latitude bands of 4°S-4°N. The common characteristic of seasonal changes in AoA-N_2O correlation is that a significant decrease in the anti-correlation is observed during local summer in each hemisphere. This is the period when the strength of the BDC is the lowest (Kodama et al., 2007, and references therein) and no significant changes in AoA are observed (see also Fig. 10.9c). The overall correlation for inner tropics from 10°S to 10°N, as shown in Fig. 10.10a, combines the behaviour of both, northern and southern hemispheres.

Taking into account the existence of strong seasonal dependencies in AoA-N_2O correlations, Fig. 10.11 represents the AoA-N_2O relation as a function of month, averaged over the period January 2004-April 2012 at (a) 15-40 km, (b) 30-35 km, and (c) 15-20 km. The colour scale stands for AoA (years) and black contours depict N_2O (VMR, ppbV).

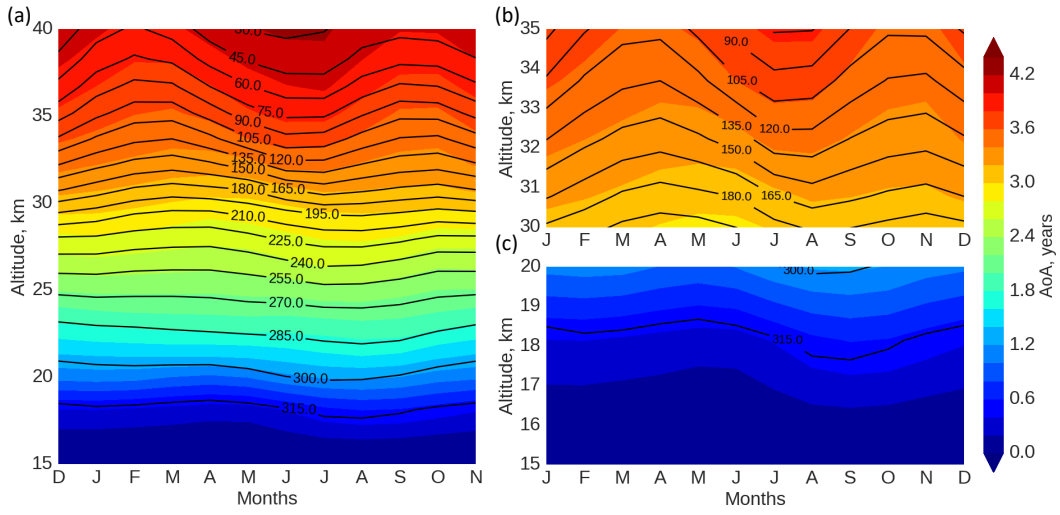

Figure 10.11: Annual cycle of monthly mean tropical N_2O (ppbV, contours, 15 ppbV interval) and AoA (years, colours, 0.2 year interval) from TOMCAT run CNTL, averaged over the period January 2004-April 2012 as a function of altitude (a) between 15-40 km, (b) 30-35 km, (c) 15-20 km.

The matching of the colour and contour isolines is pronounced and confirms a direct link between AoA and N_2O. Furthermore, as N_2O is transported from the troposphere, its concentration decreases with altitude (see also Sect. 2.2.1). In the lower stratosphere (Fig. 10.11c) N_2O and AoA show seasonal variations, but these are not as pronounced as in the middle

stratosphere (Fig. 10.11b). There are two distinct seasonal features seen in the N_2O-AoA distribution in the middle stratosphere: during January-March and September-November. During these periods AoA becomes lower in comparison with the rest of the year. Lower AoA indicates faster transport and therefore younger air, which results in high values of N_2O during these months.

10.4 Observed changes in the tropical middle stratosphere

After focusing on the seasonal variations in AoA and N_2O in the tropical middle stratosphere, this section presents further investigation of the possible chemical impact on other species. Namely, the linear changes in AoA, N_2O, NO_2, and O_3 from TOMCAT run CNTL and from SCIAMACHY and MLS measurements for each calendar month are analysed in Fig. 10.12 and Fig. 10.13 and Galytska et al. (2019a, Supplements Fig. S4-S7). TOMCAT CNTL simulation shows lower O_3 and NO_2 concentrations compared to SCIAMACHY and MLS measurements. The underestimation of modelled NO_2 and O_3 in comparison with SCIAMACHY measurements is also evident from Figs. 10.6a,b and 10.6e,f, but the slope of the modelled anti-correlation regression line agrees well with that of the SCIAMACHY observations. The possible reasons for the biases between model and observations have been already discussed in Sect. 8.3.

Figure 10.12 shows linear changes in AoA, N_2O, NO_2, and O_3 from TOMCAT CNTL simulation (green), SCIAMACHY (dark blue), and MLS (magenta) measurements. Solid lines indicate statistically significant linear changes at 2σ level, dashed lines indicate statistically insignificant linear changes. The upper panels of Fig. 10.12a-d show January linear changes, lower panels of Fig. 10.12e-h show February linear changes. The TOMCAT results for January and February show a decrease in AoA with time and a small O_3 recovery. The faster upwelling as indicated by negative changes in AoA (Fig. 10.12a,e) causes more intense N_2O transport from the troposphere. As a consequence, N_2O increases with time (Fig. 10.12b,f) and NO_2 decreases (Fig. 10.12c,g) due to the shorter residence time of N_2O: there is less time for N_2O to produce NO_x species via the $O(^1D)$ reaction (R20a). Finally, a small O_3 recovery is observed in the tropical middle stratosphere (Fig. 10.12d,h). SCIAMACHY measurements show statistically insignificant changes in NO_2 and O_3 for January and February (Fig. 10.12c-d,g-h and Galytska et al. (2019a). Both MLS and SCIAMACHY measurements show statistically insignificant changes in O_3; however MLS shows slight O_3 recovery, similar to TOMCAT. SCIAMACHY

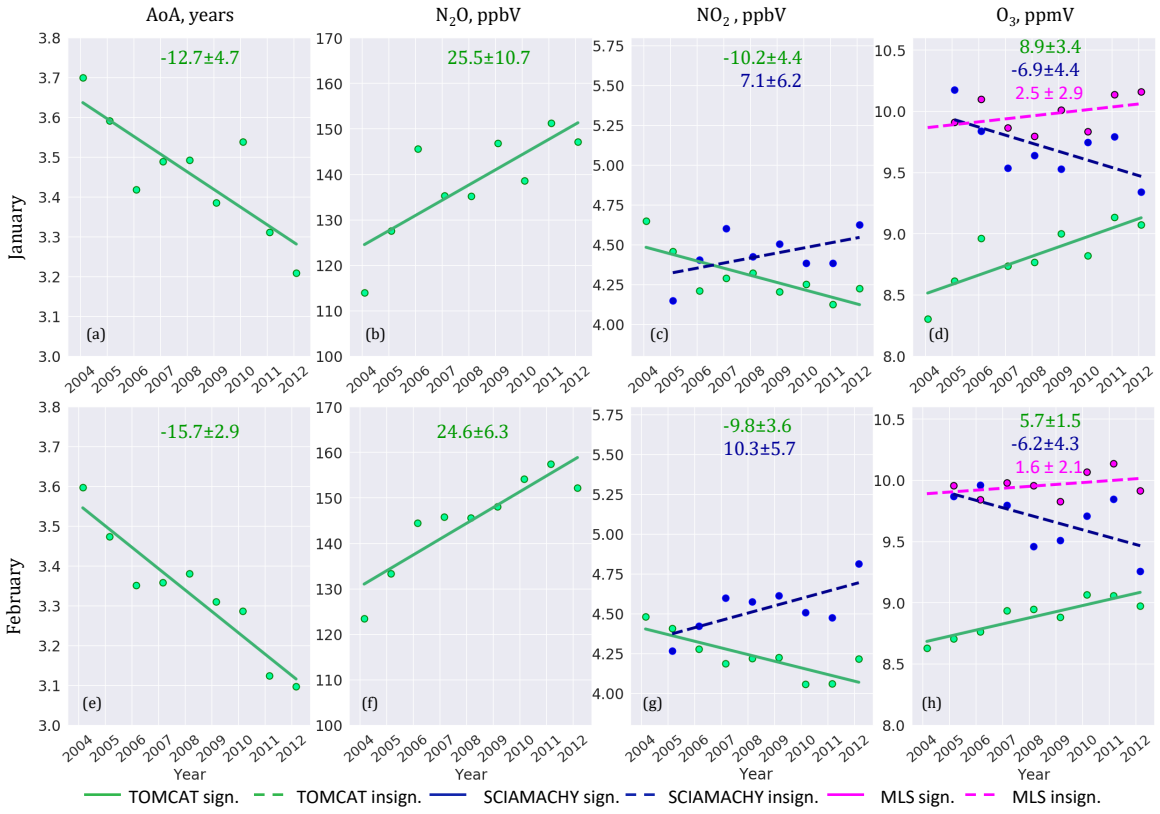

Figure 10.12: Linear changes in AoA, N_2O, NO_2, and O_3 with extracted QBO effect averaged over (a-d) Januaries 2004-2012 and (e-h) Februaries 2004-2011 in the tropical middle stratosphere. Colour coding indicates the data source: TOMCAT CNTL simulation (green), SCIAMACHY (dark blue), and MLS (magenta) measurements. Solid lines indicate statistically significant linear changes, dashed lines indicate statistically insignificant changes. Colour-coded trend values and their errors (in % per decade) are shown in each panel.

measurements in turn show statistically insignificant NO_2 increase and O_3 decrease for all calendar months, in contrast to the TOMCAT simulations.

Figure 10.13 shows the changes in AoA, N_2O, NO_2, and O_3 for September (a-d) and October (e-h). The linear change/gradients are opposite of those for the winter months shown in Fig. 10.12. The increase in AoA gradient (Fig. 10.13a,e) indicates a significant slowdown of transport or additional air mixing. Therefore, there is less N_2O transported from the troposphere (Fig. 10.13b,f) and consequently more N_2O is photolytically destroyed. The residence time in the tropical middle stratosphere becomes longer, producing more NO_2 (Fig. 10.13c,g) which destroys O_3 (Fig. 10.13d,h). SCIAMACHY NO_2 and O_3 changes and MLS O_3 change agree well with TOMCAT results for September and October.

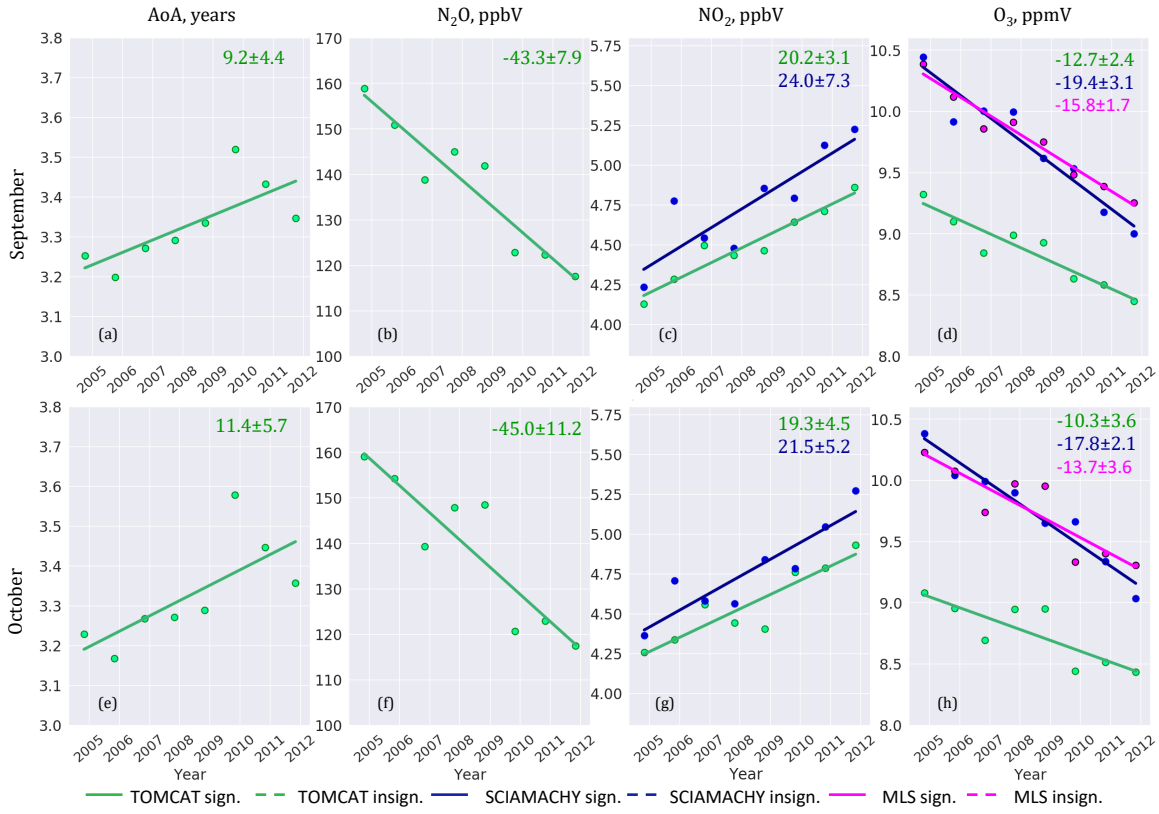

Figure 10.13: Same as Fig. 10.12, but for September and October.

From September and October to January and February, the gradient of the O_3 time series increases, becoming more positive for TOMCAT, SCIAMACHY, and MLS data, resulting for January and February in small, statistically insignificant negative gradients for SCIAMACHY, small statistically insignificant positive gradients for MLS observations, and small but statistically significant positive gradients for TOMCAT. For NO_2 from September and October to January and February the gradients decrease, i.e. they become more positive for both SCIAMACHY measurements and TOMCAT simulations. The SCIAMACHY data show larger errors on gradients of the time series for individual months, than those of the TOMCAT model and MLS measurements. This comes from the stronger oscillating structure in the SCIAMACHY time series, the reasons of which are not yet identified and are under ongoing investigation.

The negative AoA gradients for the 2004-2012 period during the boreal winter months (January and February) and positive AoA gradients during the boreal autumn months (September and October) cancel, i.e. there is no statistically significant linear change/gradient in the an-

nual mean AoA (Fig. 10.8b). In contrast, the monthly gradients over the same periods for the chemical species N_2O, NO_2 and O_3 (as a result of the NO_x ozone catalytic destruction cycle) do not cancel in the annual means. This effect is primarily attributed to the non-linear relationship between AoA and N_2O, which is explained as follows, as in (Galytska et al., 2019a): 1) AoA inversely linearly depends on the speed of the BDC, with lower AoA values indicating an acceleration, and higher AoA indicating a deceleration of the vertical transport. In the absence of significant photolytic loss of N_2O via Reaction (R19), the changes in stratospheric N_2O would be controlled only by changes in the rate of the tropical upwelling of the BDC, namely AoA. The faster upwelling would enhance transport of N_2O from the troposphere, the slower upwelling would lead to lower N_2O stratospheric concentrations. Without photolytic loss, the rate of change of N_2O concentration would be inversely proportional to the AoA change; 2) the dominant loss of N_2O is through its photolysis. The amount of photolysed N_2O depends on the residence time of N_2O, which in turn depends on the transport speed, i.e. AoA. Longer residence times of N_2O result from a transport slowdown. Consequently, there is more time for photolytic destruction of N_2O; 3) The changes in N_2O do not cancel in the annual average as the amount of N_2O is controlled by both transport and photochemistry; 4) NO_2 and O_3 are chemically linked with N_2O, therefore the overall changes in NO_2 and O_3 are dependent on both the amount of N_2O transported to the stratosphere and on its residence time.

11

Conclusions

11.1 Summary

This thesis focuses on the research of the spatio-temporal evolution of trace gases in the stratosphere. The main focus was placed on the tropical middle stratosphere, where SCIAMACHY measurements showed significant decline of O_3. One of the hypotheses of possible drivers of observed variations was associated with variability in the stratospheric dynamics. However, in order to test this hypothesis the application of reliable atmospheric model and satellite measurements were necessary.

Therefore, within the first part of the research, both atmospheric offline model: B3DCTM and TOMCAT were tested. While B3DCTM is of the same origin as the TOMCAT model, it was further developed at the IUP, University of Bremen, independently from the TOMCAT CTM. The impact of the introduced changes and improvements into B3DCTM's performance needed to be assessed. Therefore, the dynamical tracer AoA was compared between the two models, in order to evaluate the stratospheric transport. It was found that B3DCTM results in stratospheric transport that is twice as slow as the TOMCAT model, while the latter agrees well with the in situ observations and the CLaMS model (see Ploeger et al., 2015, and Chapter 9 of this thesis). As discussed in Chapter 1, stratospheric transport determines the global distribution and inter-annual variability of stratospheric O_3. Consequently, the intercomparison of O_3, NO_2, and BrO in the two models showed that TOMCAT agrees better with the observed spatio-temporal distribution and changes derived from the SCIAMACHY measurements. Therefore, the TOMCAT model was later applied for the validation of the SCIAMACHY NO_2 data set.

The accurate knowledge of trace gases distribution is achieved by application of reliable

data sets, which should be validated. As NO_2 plays an important role in the production and loss of O_3, the quality of applied data set should be evaluated. For the validation of the new SCIAMACHY NO_2 data set, several modelling approaches were tested, and a new photochemical correction scheme was developed. A number of different validation data sources were used. Namely, the SCIAMACHY limb scientific NO_2 V4.0 data set was compared with limb and occultation satellite measurements, i.e. with SCIAMACHY ESA, MIPAS (both ESA and IMK-IAA retrievals), and SAGE II. All available co-located profiles for the overlapping period of measurements were taken into account and analysed in seven different latitude regions. The mean relative difference between SCIAMACHY IUP and SCIAMACHY ESA retrievals was mostly $\pm$ 10% within the altitude range 19-42 km, between SCIAMACHY IUP and both retrievals of MIPAS within $\pm$ 10% at altitudes around 25-40 km. The mean relative difference between SCIAMACHY IUP and photochemically corrected SAGE II was found to be less than 20-25% at the altitude range between 25 and 35 km. It should be noted that only sunset SAGE II NO_2 profiles were considered in the analysis, as sunrise amounts were reported to be of lower quality and less reliable (Damadeo et al., 2013).

Based on reliable model results and validated satellite measurements, the analysis of O_3 changes in the tropical middle stratosphere was performed. O_3 variability was analysed during the period January 2004-April 2012 as observed by SCIAMACHY and simulated by the TOMCAT CTM forced by ECMWF reanalysis. It was found that the model captured the observed linear O_3 changes well within the analysed period. Using a set of TOMCAT simulations with different dynamical and chemical forcings, it was shown that the decline in O_3 is ultimately dynamically controlled and occurs due to an increase of NO_2, which then chemically removes O_3. The increase of NO_2 is due to a longer residence time of N_2O, its primary source. Changes in the abundance of this long-lived species indicate variations in the tropical upwelling. These results are in agreement with the findings of Nedoluha et al. (2015b). To confirm whether a decrease in tropical upwelling indeed took place or not, the analysis of AoA from the TOMCAT model was performed. The AoA simulations did not show any significant annual mean changes in the tropical middle stratosphere, which is in apparent contradiction with the conclusions from Nedoluha et al. (2015b).

With the knowledge of dynamically driven N_2O-NO_2-O_3 changes, but no significant changes of mean AoA, a detailed analysis of linear changes for each month separately within the period 2004-2012 was performed. It was found that during boreal autumn months, i.e. in September and October, there is a significant transport slowdown or additional air mixing in the northern

hemisphere that corresponds to positive changes of AoA. These positive changes in AoA indicate a longer residence time of N_2O, leading to increased NO_x production and enhanced O_3 loss. In this regard, changes of both SCIAMACHY and TOMCAT NO_2 and O_3 (also from MLS) are consistent. In contrast, it was found that during boreal winter months, i.e. in January and February, the AoA simulations show a transport speed-up. This indicates a decreased residence time of N_2O, so that less NO_x is produced and consequently O_3 increases. While the TOMCAT model shows a significant NO_x decrease and an O_3 increase, the SCIAMACHY changes show a small, insignificant increase of NO_2 and a decrease of O_3 during these winter months. This is partially explained by the larger uncertainties in the multiple linear regression applied to the satellite data. While MLS measurements of O_3, similar to SCIAMACHY, do not show a significance at 2σ changes, they are consistent with the TOMCAT model in terms of the O_3 increase.

Overall, the non-linear relation of AoA and N_2O and their month-to-month changes presented in this thesis explain the observed O_3 decline well in the tropical middle stratosphere. With the application of a detailed CTM it is possible to not only confirm the O_3 decline, but also to describe chemical impacts and define the role of dynamics in the observed changes.

11.2 Outlook

While the performance of the B3DCTM and TOMCAT models was clarified and the new SCIAMACHY limb NO_2 product was validated, there are still open issues that require better understanding. Starting from the seasonal variation of AoA changes and its impact on annual mean trends in the tropical middle stratosphere, as presented in this thesis, some questions still remain and should be the subject of further studies. Is the shift of subtropical transport barriers, as suggested by Eckert et al. (2014) and Stiller et al. (2017), linked to the seasonal AoA changes observed in the tropical middle stratosphere? Or, is it a result of the different behaviour of the shallow and deep branches of the BDC, e.g. the hiatus in the acceleration of the shallow branch, the strengthening of the transition branch and no significant changes in the deep branch (Aschmann et al., 2014)? The cooling in the Eastern Pacific (Meehl et al., 2011) could also affect O_3 changes via upwelling, although an analysis of sea surface temperatures (not shown here) did not show significant monthly variations. Another possible explanation for the changes in the transport regime could be planetary wave forcing (Chen and Sun, 2011), as it was found that a significant decrease in the N_2O-AoA correlation occurs during local summers,

when the wave activity and therefore the strength of the upwelling is the lowest. In particular, the impact of variations in wave activity on the seasonal build-up of O_3 was also described by Shepherd (2007). However, all of these possible explanations require additional investigation to determine which processes dominate. The CTMs with their specified meteorology cannot be used to determine the main drivers of the dynamical changes. Consequently, the application of interactive dynamical models is needed. The interpretation of the observed changes will give us an understanding of whether in the tropical middle stratospheric O_3 decline is part of its natural variability, human impact, or a complex interaction of both factors.

List of Figures

List of Tables

List of Acronyms

AoA Age of Air

ACE Atmospheric Chemistry Experiment

B3DCTM Bremen 3-D Chemistry-Transport Model

BDC Brewer-Dobson Circulation

BUV Backscattered Ultraviolet

CALIPSO Cloud-Aerosol Lidar and Infrared Pathfinder Satellite Observations

CSA Canadian Space Agency

CTM Chemistry-Transport Model

CCMs Chemistry-Climate Models

CFCs chlorofluorocarbons

CNES Centre national d'études spatiales

CNRM Centre National de Recherches Météorologiques

CLaMS Chemical Lagrangian Model of the Stratosphere

DJF December-January-February

ENSO El Niño Southern Oscillation

ENIAC Electronic Numerical Integrator and Computer

ESA European Space Agency

Envisat Environmental Satellite

ERBS Earth Radiation Budget Satellite

ECMWF European Centre for Medium-Range Weather Forecasts

EOS Earth Observing System

FTS Fourier Transform Spectrometer

GCMs General Circulation Models

GOME Global Ozone Monitoring Experiment

GOMOS Global Ozone Monitoring by Occultation of Stars

GOSAT Greenhouse Gases Observing Satellite

HALOE Halogen Occultation Experiment

HYSPLIT Hybrid Single Particle Lagrangian Integrated Trajectory Model

IUP Institut für Umweltphysik

IMK Institute of Meteorology and Climate Research at the Karlsruhe Institute of Technology

IAA Instituto de Astrofísica de Andalucía

JJA June-July-August

LOS line of sight

MIPAS Michelson Interferometer for Passive Atmospheric Sounding

MAM March-April-May

MLR multiple linear regression

MLS Microwave Limb Sounder

MPV modified potential vorticity

ND number density

NH Northern Hemisphere

NOAA National Oceanic and Atmospheric Administration

NASA National Aeronautics and Space Administration

NRL Naval Research Laboratory

OMPS Ozone Mapping Profiler Suite

OLS ordinary least squares

PSC Polar Stratospheric Clouds

PV potential vorticity

PVU potential vorticity units

ppmV parts per million by volume

ppbV parts per billion by volume

pptV parts per trillion by volume

QBO Quasibiennial oscillation

RTM radiative transfer model

RD relative difference

SAGE Stratospheric Aerosol and Gas Experiment

SCIAMACHY SCanning Imaging Absorption spectroMeter for Atmospheric CHartographY

SON September-October-November

SO Southern Oscillation

SST Sea Surface Temperature

SZA solar zenith angle

SH Southern Hemisphere

STD standard deviation

SBUV Solar Backscatter Ultraviolet

SME Solar Mesospheric Explorer

Sentinel-5P Sentinel-5 Precursor

TOMS Total Ozone Mapping Spectrometer

UV ultraviolet

UNFCCC United Nations Framework Convention on Climate Change

UTLS upper troposphere and lower stratosphere

VMR volume mixing ratio

Acknowledgements

I would like to thank Prof. John P. Burrows for the opportunity to become a member of his research team at the IUP, University of Bremen. I also thank Dr. Alexey Rozanov, who was a great immediate advisor for the last almost three years. I am also thankful to Dr. René Hommel, who supervised my research within the first year of my stay at the IUP. In this scope, I would like to thank Dr. Björn-Martin Sinnhuber and Dr. Annika Günther, who introduced me the AoA concept in the CTM, which in the end became an important part of my research topic. I would like to thank Dr. Landon Rieger and Dr. Andreas Hilboll, who were very supportive and helpful with all the Python challenges; Dr. Jan Aschmann and Dr. Holger Winkler, who helped with B3DCTM.

I would also like to express the special gratitude to Prof. Martyn P. Chipperfield and all members of his research team, in particular (in alphabetical order) Dr. Sandip S. Dhomse, Dr. Wuhu Feng, Dr. Richard Pope. In these terms I would also like to thank the Postgraduate International Physics Programme (PIP) for providing funding for the collaboration with Prof. Chipperfield, University of Leeds, UK. The data presented in the thesis were partially obtained using the German High Performance Computer Center North (HLRN) service and HPC cluster Aether at the University of Bremen, financed by DFG in the scope of the Excellence Initiative, whose support I gratefully acknowledge.

I am also thankful to (in alphabetical order) Ilias Bougoudis, Muhammad Abdul Haseeb (Institute of Automation, IAT), Maria Kyrarini (IAT), with whom I learned more about new techniques, i.e. machine learning that could be applied in the atmospheric science. I believe we were a great team in those PIP Summer Schools. Many thanks to Stephanie Drath for her kind administrative support.

Special thanks goes to my IUP family (in alphabetical order) Carlo Arosio, Rafaella Chiarella, Tina Hilbig, Tobias Küchler, Elizaveta Malinina, Nora Mettig, Andrea Orfanoz-Cheuquelaf. I believe together with you I managed to get the most of fun from the research.

15. ACKNOWLEDGEMENTS

And the most important, I am grateful to my family. I thank my parents and brother for everything what I achieved by now. Адже чого варті наші успіхи без рідних? And of course, I am thankful to my husband Tamás Kovács, who was supporting me through all this uneven path. Köszönöm türelmét, szeretetét és támogatását! Megígérem, hogy visszaadom, amikor itt az idő.

References

Andrews, D. G., Leovy, C. B., and Holton, J. R.: Middle atmosphere dynamics, vol. 40, Academic press, 1987.

Arfeuille, F., Luo, B. P., Heckendorn, P., Weisenstein, D., Sheng, J. X., Rozanov, E., Schraner, M., Brönnimann, S., Thomason, L. W., and Peter, T.: Modeling the stratospheric warming following the Mt. Pinatubo eruption: uncertainties in aerosol extinctions, Atmospheric Chemistry and Physics, 13, 11 221–11 234, https://doi.org/10.5194/acp-13-11221-2013, URL `https://www.atmos-chem-phys.net/13/11221/2013/`, 2013.

Arosio, C., Rozanov, A., Malinina, E., Weber, M., and Burrows, J. P.: Merging of ozone profiles from SCIAMACHY, OMPS and SAGE II observations to study stratospheric ozone changes, Atmospheric Measurement Techniques, 2018.

Aschmann, J.: B3DCTM Manual, URL `http://iupdoc.iup.uni-bremen.de/2217/`, 2014.

Aschmann, J. and Sinnhuber, B.-M.: Contribution of very short-lived substances to stratospheric bromine loading: uncertainties and constraints, Atmospheric Chemistry and Physics, 13, 1203–1219, 2013.

Aschmann, J., Sinnhuber, B.-M., Atlas, E. L., and Schauffler, S. M.: Modeling the transport of very short-lived substances into the tropical upper troposphere and lower stratosphere, Atmospheric Chemistry and Physics, 9, 9237–9247, https://doi.org/10.5194/acp-9-9237-2009, URL `https://www.atmos-chem-phys.net/9/9237/2009/`, 2009.

Aschmann, J., Sinnhuber, B.-M., Chipperfield, M. P., and Hossaini, R.: Impact of deep convection and dehydration on bromine loading in the upper troposphere and lower stratosphere, Atmospheric Chemistry and Physics, 11, 2671–2687, https://doi.org/10.5194/acp-11-2671-2011, URL `https://www.atmos-chem-phys.net/11/2671/2011/`, 2011.

REFERENCES

Aschmann, J., Burrows, J. P., Gebhardt, C., Rozanov, A., Hommel, R., Weber, M., and Thompson, A. M.: On the hiatus in the acceleration of tropical upwelling since the beginning of the 21st century, Atmospheric Chemistry and Physics, 14, 12 803–12 814, https://doi.org/10.5194/acp-14-12803-2014, URL `https://www.atmos-chem-phys.net/14/12803/2014/`, 2014.

Athanasopoulou, E., Vogel, H., Vogel, B., Tsimpidi, A., Pandis, S. N., Knote, C., and Fountoukis, C.: Modeling the meteorological and chemical effects of secondary organic aerosols during an EUCAARI campaign, Atmospheric Chemistry and Physics, 13, 625, 2013.

Baldwin, M., Gray, L., Dunkerton, T., Hamilton, K., Haynes, P., Randel, W., Holton, J., Alexander, M., Hirota, I., Horinouchi, T., et al.: The quasi-biennial oscillation, Reviews of Geophysics, 39, 179–229, 2001.

Ball, W. T., Alsing, J., Mortlock, D. J., Staehelin, J., Haigh, J. D., Peter, T., Tummon, F., Stübi, R., Stenke, A., Anderson, J., Bourassa, A., Davis, S. M., Degenstein, D., Frith, S., Froidevaux, L., Roth, C., Sofieva, V., Wang, R., Wild, J., Yu, P., Ziemke, J. R., and Rozanov, E. V.: Evidence for a continuous decline in lower stratospheric ozone offsetting ozone layer recovery, Atmospheric Chemistry and Physics, 18, 1379–1394, https://doi.org/10.5194/acp-18-1379-2018, URL `https://www.atmos-chem-phys.net/18/1379/2018/`, 2018.

Bauer, R.: NO2 Limb Retrieval in the Upper Troposphere/Lower Stratosphere Region, Ph.D. thesis, PhD Thesis, University of Bremen, Bremen, 2012.

Bauer, R., Rozanov, A., McLinden, C., Gordley, L., Lotz, W., Russell III, J., Walker, K., Zawodny, J., Ladstätter-Weißenmayer, A., Bovensmann, H., and Burrows, J.: Validation of SCIAMACHY limb NO2 profiles using solar occultation measurements, 5, 1059 –1084, 2012.

Birner, T. and Bönisch, H.: Residual circulation trajectories and transit times into the extratropical lowermost stratosphere, Atmospheric Chemistry and Physics, 11, 817–827, 2011.

Bjerknes, J.: Atmospheric teleconnections from the equatorial Pacific, Monthly weather review, 97, 163–172, 1969.

Blunden, J. and Arndt, D. S.: State of the climate in 2015, Bulletin of the American Meteorological Society, 97, Si–S275, 2016.

Bönisch, H., Engel, A., Birner, T., Hoor, P., Tarasick, D. W., and Ray, E. A.: On the structural changes in the Brewer-Dobson circulation after 2000, Atmospheric Chemistry and Physics, 11, 3937–3948, https://doi.org/10.5194/acp-11-3937-2011, URL https://www.atmos-chem-phys.net/11/3937/2011/, 2011.

Bracher, A., Sinnhuber, M., Rozanov, A., and Burrows, J. P.: Using a photochemical model for the validation of NO_2 satellite measurements at different solar zenith angles, ACP, 5, 393–408, 2005.

Brasseur, G., Orlando, J. J., Tyndall, G. S., et al.: Atmospheric chemistry and global change, Oxford University Press, 1999.

Brasseur, G. P. and Solomon, S.: Aeronomy of the middle atmosphere: chemistry and physics of the stratosphere and mesosphere, vol. 32, Springer Science, 2005.

Bregmann, A., Lelieveld, J., van den Broek, M. M. P., Siegmund, P. C., Fischer, H., and Bujok, O.: N2O and O3 relationship in the lowermost stratosphere: A diagnostic for mixing processes as represented by a three-dimensional chemistry-transport model, Journal of Geophysical Research: Atmospheres, 105, 17 279–17 290, https://doi.org/10.1029/2000JD900035, URL https://agupubs.onlinelibrary.wiley.com/doi/abs/10.1029/2000JD900035, 2000.

Brewer, A.: Evidence for a world circulation provided by the measurements of helium and water vapour distribution in the stratosphere, Quarterly Journal of the Royal Meteorological Society, 75, 351–363, 1949.

Brohede, S. M., Haley, C. S., McLinden, C. A., Sioris, C. E., Murtagh, D. P., Petelina, S. V., Llewellyn, E. J., Bazureau, A., Goutail, F., Randall, C. E., Lumpe, J. D., Taha, G., Thomasson, L. W., and Gordley, L. L.: Validation of Odin/OSIRIS stratospheric NO2 profiles, Journal of Geophysical Research: Atmospheres, 112, n/a–n/a, 2007.

Burrows, J. P., Hölzle, E., Goede, A. P. H., Visser, H., and Fricke, W.: SCIAMACHY—Scanning imaging absorption spectrometer for atmospheric chartography, Astron. & Astrophys., 35, 445–451, 1995.

Butchart, N., Cionni, I., Eyring, V., Shepherd, T., Waugh, D., Akiyoshi, H., Austin, J., Brühl, C., Chipperfield, M., Cordero, E., et al.: Chemistry–climate model simulations of twenty-first century stratospheric climate and circulation changes, Journal of Climate, 23, 5349–5374, 2010.

Carlotti, M. and Magnani, L.: Two-dimensional sensitivity analysis of MIPAS observations, Optics express, 17, 5340–5357, 2009.

Chance, K., Burrows, J., Perner, D., and Schneider, W.: Satellite measurements of atmospheric ozone profiles, including tropospheric ozone, from ultraviolet/visible measurements in the nadir geometry: a potential method to retrieve tropospheric ozone, Journal of Quantitative Spectroscopy and Radiative Transfer, 57, 467–476, 1997.

Chapman, S. F.: On ozone and atomic oxygen in the upper atmosphere, The London, Edinburgh, and Dublin Philosophical Magazine and Journal of Science, 10, 369–383, https://doi.org/10.1080/14786443009461588, URL https://doi.org/10.1080/14786443009461588, 1930.

Chen, G. and Sun, L.: Mechanisms of the Tropical Upwelling Branch of the Brewer–Dobson Circulation: The Role of Extratropical Waves, Journal of the Atmospheric Sciences, 68, 2878–2892, https://doi.org/10.1175/JAS-D-11-044.1, URL https://doi.org/10.1175/JAS-D-11-044.1, 2011.

Chipperfield, M. P.: New version of the TOMCAT/SLIMCAT off-line chemical transport model: Intercomparison of stratospheric tracer experiments, Quarterly Journal of the Royal Meteorological Society, 132, 1179–1203, https://doi.org/10.1256/qj.05.51, URL https://rmets.onlinelibrary.wiley.com/doi/abs/10.1256/qj.05.51, 2006.

Chipperfield, M. P., Cariolle, D., Simon, P., Ramaroson, R., and Lary, D. J.: A three-dimensional modeling study of trace species in the Arctic lower stratosphere during winter 1989–1990, Journal of Geophysical Research: Atmospheres, 98, 7199–7218, https://doi.org/10.1029/92JD02977, URL http://dx.doi.org/10.1029/92JD02977, 1993.

Chipperfield, M. P., Santee, M. L., Froidevaux, L., Manney, G. L., Read, W. G., Waters, J. W., Roche, A. E., and Russell, J. M.: Analysis of UARS data in the southern polar vortex in September 1992 using a chemical transport model, Journal of Geophysical Research: Atmospheres, 101, 18 861–18 881, 1996.

Chipperfield, M. P., Bekki, Slimane, D. S., Harris, N. R. P., Hassler, B., Hossaini, R., Steinbrecht, W., Thiéblemont, R., and Weber, M.: Detecting recovery of the stratospheric ozone layer, Nature, p. 211–218, https://doi.org/10.1038/nature23681, 2017.

Chipperfield, M. P., Dhomse, S., Hossaini, R., Feng, W., Santee, M. L., Weber, M., Burrows, J. P., Wild, J. D., Loyola, D., and Coldewey-Egbers, M.: On the Cause of Recent Variations in Lower Stratospheric Ozone, Geophysical Research Letters, 0, https://doi.org/10.1029/2018GL078071, URL https://agupubs.onlinelibrary.wiley.com/doi/abs/10.1029/2018GL078071, 2018.

Chu, W., McCormick, M., Lenoble, J., Brogniez, C., and Pruvost, P.: SAGE II Inversion Algorithm, J. Geophys. Res., 94, 8339–8351, 1989.

Coddington, O., Lean, J. L., Pilewskie, P., Snow, M., and Lindholm, D.: A Solar Irradiance Climate Data Record, Bulletin of the American Meteorological Society, 97, 1265–1282, https://doi.org/10.1175/BAMS-D-14-00265.1, URL https://doi.org/10.1175/BAMS-D-14-00265.1, 2016.

Damadeo, R., Zawodny, J., Thomason, L., and Iyer, N.: SAGE version 7.0 algorithm: application to SAGE II, Atmospheric Measurement Techniques, 6, 3539–3561, 2013.

Dee, D. P., Uppala, S. M., Simmons, A. J., Berrisford, P., Poli, P., Kobayashi, S., Andrae, U., Balmaseda, M. A., Balsamo, G., Bauer, P., Bechtold, P., Beljaars, A. C. M., van de Berg, L., Bidlot, J., Bormann, N., Delsol, C., Dragani, R., Fuentes, M., Geer, A. J., Haimberger, L., Healy, S. B., Hersbach, H., Hólm, E. V., Isaksen, L., Kållberg, P., Köhler, M., Matricardi, M., McNally, A. P., Monge-Sanz, B. M., Morcrette, J., Park, B., Peubey, C., de Rosnay, P., Tavolato, C., Thépaut, J., and Vitart, F.: The ERA-Interim reanalysis: configuration and performance of the data assimilation system, Quarterly Journal of the Royal Meteorological Society, 137, 553–597, https://doi.org/10.1002/qj.828, URL https://rmets.onlinelibrary.wiley.com/doi/abs/10.1002/qj.828, 2011.

Dhomse, S., Weber, M., Wohltmann, I., Rex, M., and Burrows, J. P.: On the possible causes of recent increases in northern hemispheric total ozone from a statistical analysis of satellite data from 1979 to 2003, Atmospheric Chemistry and Physics, 6, 1165–1180, https://doi.org/10.5194/acp-6-1165-2006, URL https://www.atmos-chem-phys.net/6/1165/2006/, 2006.

Dhomse, S., Chipperfield, M., Damadeo, R., Zawodny, J., Ball, W., Feng, W., Hossaini, R., Mann, G., and Haigh, J.: On the ambiguous nature of the 11 year solar cycle signal in upper stratospheric ozone, Geophysical Research Letters, 43, 7241–7249, 2016.

Dhomse, S. S., Chipperfield, M. P., Feng, W., Hossaini, R., Mann, G. W., and Santee, M. L.: Revisiting the hemispheric asymmetry in midlatitude ozone changes following the Mount Pinatubo eruption: A 3-D model study, Geophysical Research Letters, 42, 3038–3047, https://doi.org/10.1002/2015GL063052, URL https://agupubs.onlinelibrary.wiley.com/doi/abs/10.1002/2015GL063052, 2015.

Diallo, M., Legras, B., and Chédin, A.: Age of stratospheric air in the ERA-Interim, Atmospheric Chemistry and Physics, 12, 12 133–12 154, 2012.

Diallo, M., Konopka, P., Santee, M. L., Müller, R., Tao, M., Walker, K. A., Legras, B., Riese, M., Ern, M., and Ploeger, F.: Structural changes in the shallow and transition branch of the Brewer–Dobson circulation induced by El Niño, Atmospheric Chemistry and Physics, 19, 425–446, 2019.

Dobson, G. M. B.: Origin and distribution of the polyatomic molecules in the atmosphere, Proc. R. Soc. Lond. A, 236, 187–193, 1956.

Dobson, G. M. B., Harrison, D., and Lawrence, J.: Measurements of the amount of ozone in the Earth's atmosphere and its relation to other geophysical conditions.—Part III, Proceedings of the Royal Society of London. Series A, Containing Papers of a Mathematical and Physical Character, 122, 456–486, 1929.

Dupuy, E., Walker, K., Kar, J., Boone, C., McElroy, C., Bernath, P., Drummond, J., Skelton, R., McLeod, S., Hughes, R., et al.: Validation of ozone measurements from the Atmospheric Chemistry Experiment (ACE), Atmospheric Chemistry and Physics, 9, 287–343, 2009.

Eckert, E., von Clarmann, T., Kiefer, M., Stiller, G. P., Lossow, S., Glatthor, N., Degenstein, D. A., Froidevaux, L., Godin-Beekmann, S., Leblanc, T., McDermid, S., Pastel, M., Steinbrecht, W., Swart, D. P. J., Walker, K. A., and Bernath, P. F.: Drift-corrected trends and periodic variations in MIPAS IMK/IAA ozone measurements, Atmospheric Chemistry and Physics, 14, 2571–2589, https://doi.org/10.5194/acp-14-2571-2014, URL https://www.atmos-chem-phys.net/14/2571/2014/, 2014.

Engel, A., Möbius, T., Bönisch, H., Schmidt, U., Heinz, R., Levin, I., Atlas, E., Aoki, S., Nakazawa, T., Sugawara, S., et al.: Age of stratospheric air unchanged within uncertainties over the past 30 years, Nature Geoscience, 2, 28, 2009.

Eyring, V., Butchart, N., Waugh, D., Akiyoshi, H., Austin, J., Bekki, S., Bodeker, G., Boville, B., Brühl, C., Chipperfield, M., et al.: Assessment of temperature, trace species, and ozone in chemistry-climate model simulations of the recent past, Journal of Geophysical Research: Atmospheres, 111, 2006.

Farman, J. C., Gardiner, B. G., and Shanklin, J. D.: Large losses of total ozone in Antarctica reveal seasonal ClOx/NOx interaction, Nature, 315, 207, 1985.

Feng, W., Chipperfield, M., Davies, S., Sen, B., Toon, G., Blavier, J., Webster, C., Volk, C., Ulanovsky, A., Ravegnani, F., et al.: Three-dimensional model study of the Arctic ozone loss in 2002/2003 and comparison with 1999/2000 and 2003/2004, Atmospheric chemistry and physics, 5, 139–152, 2005.

Fischer, H., Birk, M., Blom, C., Carli, B., Carlotti, M., von Clarmann, T., Delbouille, L., Dudhia, A., Ehhalt, D., Endemann, M., Flaud, J. M., Gessner, R., Kleinert, A., Koopman, R., Langen, J., López-Puertas, M., Mosner, P., Nett, H., Oelhaf, H., Perron, G., Remedios, J., Ridolfi, M., Stiller, G., and Zander, R.: MIPAS: an instrument for atmospheric and climate research, Atmospheric Chemistry and Physics, 8, 2151–2188, https://doi.org/10.5194/acp-8-2151-2008, URL `https://www.atmos-chem-phys.net/8/2151/2008/`, 2008.

Fish, D., Jones, R., and Strong, E.: Midlatitude observations of the diurnal variation of stratospheric BrO, Journal of Geophysical Research: Atmospheres, 100, 18 863–18 871, 1995.

Funke, B., López-Puertas, M., Holt, L., Randall, C. E., Stiller, G. P., and von Clarmann, T.: Hemispheric distributions and interannual variability of NOy produced by energetic particle precipitation in 2002-2012, JGR, 119, 13,565–13,582, 2014.

Galytska, E., Rozanov, A., Weber, M., Hommel, R., Weigel, K., and Burrows, J. P.: SCIAMACHY V6.01 Nitrogen Dioxide Limb Validation, SCILOV-15 Project Report, pp. 1–24, URL `https://earth.esa.int/web/sppa/mission-performance/esa-missions/envisat/sciamachy/cal/val/validation-activities/`, 2017.

Galytska, E., Rozanov, A., Chipperfield, M. P., Dhomse, S., Weber, M., Arosio, C., Feng, W., Burrows, J. P., et al.: Dynamically controlled ozone decline in the tropical mid-stratosphere observed by SCIAMACHY, Atmospheric Chemistry and Physics, 19, 767–783, 2019a.

Galytska, E., Rozanov, A., Chipperfield, M. P., Hommel, R., and Burrows, J. P.: Validation of SCIAMACHY NO_2 V4.0: accounting for differences in local solar time, in preparation for publication in AMT, Atmospheric Measurement Techniques, 2019b.

Garny, H., Birner, T., Bönisch, H., and Bunzel, F.: The effects of mixing on age of air, Journal of Geophysical Research: Atmospheres, 119, 7015–7034, 2014.

Gebhardt, C.: Linear Changes/trends in Stratospheric O3 and BrO as Seen by SCIAMACHY Limb Measurements During the Decade 2002-2012, Ph.D. thesis, Staats-und Universitätsbibliothek Bremen, 2014.

Gebhardt, C., Rozanov, A., Hommel, R., Weber, M., Bovensmann, H., Burrows, J. P., Degenstein, D., Froidevaux, L., and Thompson, A. M.: Stratospheric ozone trends and variability as seen by SCIAMACHY from 2002 to 2012, Atmospheric Chemistry and Physics, 14, 831–846, https://doi.org/10.5194/acp-14-831-2014, URL `https://www.atmos-chem-phys.net/14/831/2014/`, 2014.

Goosse, H.: Climate System Dynamics and Modeling, Cambridge University Press, 2015.

Gottwald, M. and Bovensmann, H.: SCIAMACHY-Exploring the changing Earth's Atmosphere, Springer Science & Business Media, 2010.

Gray, L. J., Beer, J., Geller, M., Haigh, J. D., Lockwood, M., Matthes, K., Cubasch, U., Fleitmann, D., Harrison, G., Hood, L., et al.: Solar influences on climate, Reviews of Geophysics, 48, 2010.

Hack, J.: Climate system simulation: basic numerical and computational concepts, 1992.

Haenel, F. J., Stiller, G. P., von Clarmann, T., Funke, B., Eckert, E., Glatthor, N., Grabowski, U., Kellmann, S., Kiefer, M., Linden, A., and Reddmann, T.: Reassessment of MIPAS age of air trends and variability, Atmospheric Chemistry and Physics, 15, 13 161–13 176, https://doi.org/10.5194/acp-15-13161-2015, URL `https://www.atmos-chem-phys.net/15/13161/2015/`, 2015.

Heath, D. F., Mateer, C. L., and Krueger, A. J.: The Nimbus-4 Backscatter Ultraviolet (BUV) atmospheric ozone experiment—tow years' operation, Pure and Applied Geophysics, 106, 1238–1253, 1973.

Hegglin, M. I. and Shepherd, T. G.: O3-N2O correlations from the Atmospheric Chemistry Experiment: Revisiting a diagnostic of transport and chemistry in the stratosphere, Journal of Geophysical Research: Atmospheres, 112, https://doi.org/10.1029/2006JD008281, URL https://agupubs.onlinelibrary.wiley.com/doi/abs/10.1029/2006JD008281, 2007.

Hegglin, M. I., Brunner, D., Peter, T., Hoor, P., Fischer, H., Staehelin, J., Krebsbach, M., Schiller, C., Parchatka, U., and Weers, U.: Measurements of NO, NO_y, N_2O, and O_3 during SPURT: implications for transport and chemistry in the lowermost stratosphere, Atmospheric Chemistry and Physics, 6, 1331–1350, https://doi.org/10.5194/acp-6-1331-2006, URL https://www.atmos-chem-phys.net/6/1331/2006/, 2006.

Holloway, A. M. and Wayne, R. P.: Atmospheric chemistry, Royal Society of Chemistry, 2010.

Holton, J. R. and Hakim, G. J.: An introduction to dynamic meteorology, vol. 88, Academic press, 2012.

Hommel, R., Timmreck, C., Giorgetta, M. A., and Graf, H. F.: Quasi-biennial oscillation of the tropical stratospheric aerosol layer, Atmospheric Chemistry and Physics, 15, 5557–5584, 2015.

Jacob, D.: Introduction to Atmospheric Chemistry, Princeton University Press, URL https://books.google.de/books?id=FcqHAQAACAAJ, 1999.

Jacobson, M. Z.: Atmospheric Pollution: History, Science, and Regulation, Cambridge University Press, https://doi.org/10.1017/CBO9780511802287, 2002.

Jia, J., Rozanov, A., Ladstätter-Weißenmayer, A., and Burrows, J. P.: Global validation of SCIAMACHY limb ozone data (versions 2.9 and 3.0, IUP Bremen) using ozonesonde measurements, Atmospheric Measurement Techniques, 8, 3369–3383, https://doi.org/10.5194/amt-8-3369-2015, URL https://www.atmos-meas-tech.net/8/3369/2015/, 2015.

Keller-Rudek, H., Moortgat, G. K., Sander, R., and Sörensen, R.: The MPI-Mainz UV/VIS Spectral Atlas of Gaseous Molecules of Atmospheric Interest, Earth System Science Data, 5, 365–373, https://doi.org/10.5194/essd-5-365-2013, URL https://www.earth-syst-sci-data.net/5/365/2013/, 2013.

Kiesewetter, G., Sinnhuber, B.-M., Vountas, M., Weber, M., and Burrows, J.: A long-term stratospheric ozone data set from assimilation of satellite observations: High-latitude ozone anomalies, Journal of Geophysical Research: Atmospheres, 115, 2010.

Kodama, C., Iwasaki, T., Shibata, K., and Yukimoto, S.: Changes in the stratospheric mean meridional circulation due to increased CO2: Radiation- and sea surface temperature–induced effects, Journal of Geophysical Research: Atmospheres, 112, https://doi.org/10.1029/2006JD008219, URL https://agupubs.onlinelibrary.wiley.com/doi/abs/10.1029/2006JD008219, 2007.

Kovács, T., Feng, W., Totterdill, A., Plane, J. M. C., Dhomse, S., Gómez-Martín, J. C., Stiller, G. P., Haenel, F. J., Smith, C., Forster, P. M., García, R. R., Marsh, D. R., and Chipperfield, M. P.: Determination of the atmospheric lifetime and global warming potential of sulfur hexafluoride using a three-dimensional model, Atmospheric Chemistry and Physics, 17, 883–898, https://doi.org/10.5194/acp-17-883-2017, URL https://www.atmos-chem-phys.net/17/883/2017/, 2017.

Kyrölä, E., Laine, M., Sofieva, V., Tamminen, J., Päivärinta, S.-M., Tukiainen, S., Zawodny, J., and Thomason, L.: Combined SAGE II-GOMOS ozone profile data set for 1984-2011 and trend analysis of the vertical distribution of ozone, Atmospheric Chemistry and Physics, 13, 10 645–10 658, https://doi.org/10.5194/acp-13-10645-2013, URL https://www.atmos-chem-phys.net/13/10645/2013/, 2013.

Lin, P. and Fu, Q.: Changes in various branches of the Brewer–Dobson circulation from an ensemble of chemistry climate models, Journal of Geophysical Research: Atmospheres, 118, 73–84, 2013.

Lynch, P.: The origins of computer weather prediction and climate modeling, Journal of Computational Physics, 227, 3431–3444, 2008.

Mahieu, E., Chipperfield, P., M., Notholt, J., Reddmann, T., Anderson, J., Bernath, F., P., Blumenstock, T., Coffey, T., M., Dhomse, S., S., Feng, W., Franco, B., Froidevaux, L., Griffith, T., D. W., Hannigan, W., J., Hase, F., Hossaini, R., Jones, B., N., Morino, I., Murata, I., Nakajima, H., Palm, M., Paton-Walsh, C., III, Russell, J. M., Schneider, M., Servais, C., Smale, D., Walker, and A., K.: Recent Northern Hemisphere stratospheric HCl

increase due to atmospheric circulation changes, Nature, 515, 104–107, https://doi.org/10.1038/nature13857, URL http://dx.doi.org/10.1038/nature13857, 2014.

McLinden, C. A., Prather, M. J., and Johnson, M. S.: Global modeling of the isotopic analogues of N2O: Stratospheric distributions, budgets, and the 17O–18O mass-independent anomaly, Journal of Geophysical Research: Atmospheres, 108, https://doi.org/10.1029/2002JD002560, URL https://agupubs.onlinelibrary.wiley.com/doi/abs/10.1029/2002JD002560, 2003.

McLinden, C.and Olsen, S. C., Hannegan, B., Wild, O., and Prather, M. J.and Sundet, J.: Stratospheric ozone in 3-D models: A simple chemistry and the cross-tropopause flux, J. Geophys. Res., 105, 14 653, 2000.

Meehl, G., Arblaster, J., Fasullo, J., Hu, A., and Trenberth, K.: Model-based evidence of deep-ocean heat uptake during surface-temperature hiatus periods, Nature Climate Change, 1, 360 – 364, https://doi.org/10.1038/nclimate1229, 2011.

Meier, R., Jr., D. A., and Nicolet, M.: Radiation field in the troposphere and stratosphere from 240–1000 NM-I. General analysis, Planetary and Space Science, 30, 923 – 933, 1982.

Nedoluha, G. E., Boyd, I. S., Parrish, A., Gomez, R. M., Allen, D. R., Froidevaux, L., Connor, B. J., and Querel, R. R.: Unusual stratospheric ozone anomalies observed in 22 years of measurements from Lauder, New Zealand, Atmospheric Chemistry and Physics, 15, 6817–6826, https://doi.org/10.5194/acp-15-6817-2015, URL https://www.atmos-chem-phys.net/15/6817/2015/, 2015a.

Nedoluha, G. E., Siskind, D. E., Lambert, A., and Boone, C.: The decrease in mid-stratospheric tropical ozone since 1991, Atmospheric Chemistry and Physics, 15, 4215–4224, https://doi.org/10.5194/acp-15-4215-2015, URL https://www.atmos-chem-phys.net/15/4215/2015/, 2015b.

Nicolet, M.: The solar spectral irradiance and its action in the atmospheric photodissociation processes, Planetary and Space Science, 29, 951 – 974, https://doi.org/https://doi.org/10.1016/0032-0633(81)90056-8, URL http://www.sciencedirect.com/science/article/pii/0032063381900568, 1981.

Noxon, J.: Nitrogen dioxide in the stratosphere and troposphere measured by ground-based absorption spectroscopy, Science, 189, 547–549, 1975.

Noxon, J.: Stratospheric NO2: 2. Global behavior, Journal of Geophysical Research: Oceans, 84, 5067–5076, 1979.

Ploeger, F., Riese, M., Haenel, F., Konopka, P., Müller, R., and Stiller, G.: Variability of stratospheric mean age of air and of the local effects of residual circulation and eddy mixing, Journal of Geophysical Research: Atmospheres, 120, 716–733, 2015.

Portmann, R. W., Daniel, J. S., and Ravishankara, A. R.: Stratospheric ozone depletion due to nitrous oxide: influences of other gases, Philosophical Transactions of the Royal Society of London B: Biological Sciences, 367, 1256–1264, https://doi.org/10.1098/rstb.2011.0377, URL http://rstb.royalsocietypublishing.org/content/367/1593/1256, 2012.

Prather, M.: Catastrophic loss of stratospheric ozone in dense volcanic clouds, J. Geophys. Res., 97, 10 187–10 191, 1992.

Prather, M. J.: Numerical advection by conservation of second-order moments, Journal of Geophysical Research: Atmospheres, 91, 6671–6681, 1986.

Randel, W. J., Garcia, R. R., Calvo, N., and Marsh, D.: ENSO influence on zonal mean temperature and ozone in the tropical lower stratosphere, Geophysical Research Letters, 36, 2009.

Ravishankara, A. R., Daniel, J. S., and Portmann, R. W.: Nitrous Oxide (N2O): The Dominant Ozone-Depleting Substance Emitted in the 21st Century, Science, 326, 123–125, https://doi.org/10.1126/science.1176985, URL http://science.sciencemag.org/content/326/5949/123, 2009.

Reber, C. A., Trevathan, C. E., McNeal, R. J., and Luther, M. R.: The upper atmosphere research satellite (UARS) mission, Journal of Geophysical Research: Atmospheres, 98, 10 643–10 647, 1993.

Richardson, L. F.: Weather prediction by numerical process, Cambridge University Press, 1922.

Richter, A., Eisinger, M., Ladstätter-Weißenmayer, A., and Burrows, J.: DOAS zenith sky observations: 2. Seasonal variation of BrO over Bremen (53 N) 1994-1995, Journal of Atmospheric Chemistry, 32, 83–99, 1999.

Rinsland, C. P., Luo, M., Logan, J. A., Beer, R., Worden, H., Kulawik, S. S., Rider, D., Osterman, G., Gunson, M., Eldering, A., et al.: Nadir measurements of carbon monoxide distributions by the Tropospheric Emission Spectrometer instrument onboard the Aura Spacecraft: Overview of analysis approach and examples of initial results, Geophysical Research Letters, 33, 2006.

Rozanov, V. V., Rozanov, A. V., Kokhanovsky, A. A., and Burrows, J. P.: Radiative transfer through terrestrial atmosphere and ocean: Software package SCIATRAN, 133, 13 – 71, 2014.

Sakazaki, T., Fujiwara, M., Mitsuda, C., Imai, K., Manago, N., Naito, Y., Nakamura, T., Akiyoshi, H., Kinnison, D., Sano, T., et al.: Diurnal ozone variations in the stratosphere revealed in observations from the Superconducting Submillimeter-Wave Limb-Emission Sounder (SMILES) on board the International Space Station (ISS), Journal of Geophysical Research: Atmospheres, 118, 2991–3006, 2013.

Sankey, D. and Shepherd, T. G.: Correlations of long-lived chemical species in a middle atmosphere general circulation model, Journal of Geophysical Research: Atmospheres, 108, https://doi.org/10.1029/2002JD002799, URL `https://agupubs.onlinelibrary.wiley.com/doi/abs/10.1029/2002JD002799`, 2003.

Santoso, A., Mcphaden, M. J., and Cai, W.: The defining characteristics of ENSO extremes and the strong 2015/2016 El Niño, Reviews of Geophysics, 55, 1079–1129, 2017.

Scorer, R. S.: Dynamics of meteorology and climate, John Wiley & Sons, 1997.

Seinfeld, J. and Pandis, S.: Atmospheric Chemistry and Physics: From Air Pollution to Climate Change, A Wiley-Interscience publication, Wiley, 2006.

Sheese, P. E., Walker, K. A., Boone, C. D., McLinden, C. A., Bernath, P. F., Bourassa, A. E., Burrows, J. P., Degenstein, D. A., Funke, B., Fussen, D., Manney, G. L., McElroy, C. T., Murtagh, D., Randall, C. E., Raspollini, P., Rozanov, A., Russell III, J. M., Suzuki, M., Shiotani, M., Urban, J., von Clarmann, T., and Zawodny, J. M.: Validation of ACE-FTS version 3.5 NO_y species profiles using correlative satellite measurements, Atmospheric Measurement Techniques, 9, 5781–5810, https://doi.org/10.5194/amt-9-5781-2016, URL `https://www.atmos-meas-tech.net/9/5781/2016/`, 2016.

Shepherd, T. G.: Transport in the Middle Atmosphere, Journal of the Meteorological Society of Japan. Ser. II, 85B, 165–191, https://doi.org/10.2151/jmsj.85B.165, 2007.

Singer, S. and Wentworth, R.: A method for the determination of the vertical ozone distribution from a satellite, Journal of Geophysical Research, 62, 299–308, 1957.

Sinnhuber, B.-M., Weber, M., Amankwah, A., and Burrows, J. P.: Total ozone during the unusual Antarctic winter of 2002, Geophysical Research Letters, 30, https://doi.org/10.1029/2002GL016798, URL http://dx.doi.org/10.1029/2002GL016798, 1580, 2003.

Sinnhuber, M., Nieder, H., and Wieters, N.: Energetic particle precipitation and the chemistry of the mesosphere/lower thermosphere, Surveys in Geophysics, 33, 1281–1334, 2012.

Sioris, C., Kovalenko, L., McLinden, C., Salawitch, R., Van Roozendael, M., Goutail, F., Dorf, M., Pfeilsticker, K., Chance, K., Von Savigny, C., et al.: Latitudinal and vertical distribution of bromine monoxide in the lower stratosphere from Scanning Imaging Absorption Spectrometer for Atmospheric Chartography limb scattering measurements, Journal of Geophysical Research: Atmospheres, 111, 2006.

Sofieva, V. F., Kyrölä, E., Laine, M., Tamminen, J., Degenstein, D., Bourassa, A., Roth, C., Zawada, D., Weber, M., Rozanov, A., Rahpoe, N., Stiller, G., Laeng, A., von Clarmann, T., Walker, K. A., Sheese, P., Hubert, D., van Roozendael, M., Zehner, C., Damadeo, R., Zawodny, J., Kramarova, N., and Bhartia, P. K.: Merged SAGE II, Ozone_cci and OMPS ozone profile dataset and evaluation of ozone trends in the stratosphere, Atmospheric Chemistry and Physics, 17, 12 533–12 552, https://doi.org/10.5194/acp-17-12533-2017, URL https://www.atmos-chem-phys.net/17/12533/2017/, 2017.

Solomon, S.: Stratospheric ozone depletion: A review of concepts and history, Reviews of Geophysics, 37, 275–316, 1999.

Steinbrecht, W., Froidevaux, L., Fuller, R., Wang, R., Anderson, J., Roth, C., Bourassa, A., Degenstein, D., Damadeo, R., Zawodny, J., Frith, S., McPeters, R., Bhartia, P., Wild, J., Long, C., Davis, S., Rosenlof, K., Sofieva, V., Walker, K., Rahpoe, N., Rozanov, A., Weber, M., Laeng, A., von Clarmann, T., Stiller, G., Kramarova, N., Godin-Beekmann, S., Leblanc, T., Querel, R., Swart, D., Boyd, I., Hocke, K., Kämpfer, N., Maillard Barras, E., Moreira, L., Nedoluha, G., Vigouroux, C., Blumenstock, T., Schneider, M., García, O., Jones, N., Mahieu, E., Smale, D., Kotkamp, M., Robinson, J., Petropavlovskikh, I., Harris, N., Hassler,

B., Hubert, D., and Tummon, F.: An update on ozone profile trends for the period 2000 to 2016, Atmospheric Chemistry and Physics, 17, 10 675–10 690, https://doi.org/10.5194/acp-17-10675-2017, URL https://www.atmos-chem-phys.net/17/10675/2017/, 2017.

Stiller, G., Clarmann, T. v., Höpfner, M., Glatthor, N., Grabowski, U., Kellmann, S., Kleinert, A., Linden, A., Milz, M., Reddmann, T., et al.: Global distribution of mean age of stratospheric air from MIPAS SF 6 measurements, Atmospheric Chemistry and Physics, 8, 677–695, 2008.

Stiller, G. P., Fierli, F., Ploeger, F., Cagnazzo, C., Funke, B., Haenel, F. J., Reddmann, T., Riese, M., and von Clarmann, T.: Shift of subtropical transport barriers explains observed hemispheric asymmetry of decadal trends of age of air, Atmospheric Chemistry and Physics, 17, 11 177–11 192, https://doi.org/10.5194/acp-17-11177-2017, URL https://www.atmos-chem-phys.net/17/11177/2017/, 2017.

Tiao, G. C., Reinsel, G. C., Xu, D., Pedrick, J. H., Zhu, X., Miller, A. J., DeLuisi, J. J., Mateer, C. L., and Wuebbles, D. J.: Effects of autocorrelation and temporal sampling schemes on estimates of trend and spatial correlation, Journal of Geophysical Research: Atmospheres, 95, 20 507–20 517, https://doi.org/10.1029/JD095iD12p20507, URL https://agupubs.onlinelibrary.wiley.com/doi/abs/10.1029/JD095iD12p20507, 1990.

Trenberth, K. E.: Climate system modeling, Cambridge University Press, 1992.

Vaughan, G.: Diurnal variation of mesospheric ozone, Nature, 296, 133, 1982.

von Clarmann, T., Höpfner, M.and Kellmann, S., Linden, A., Chauhan, S., Funke, B., Grabowski, U.and Glatthor, N., Kiefer, M., Schieferdecker, T., Stiller, G. P., , and Versick, S.: Retrieval of temperature, H2O, O3, HNO3, CH4, N2O, ClONO2 and ClO from MIPAS reduced resolution nominal mode limb emission measurements, 2, 159 –175, 2009.

Wallace, J. M. and Hobbs, P. V.: Atmospheric science: an introductory survey, vol. 92, Elsevier, 2006.

Waters, J. W., Froidevaux, L., Harwood, R. S., Jarnot, R. F., Pickett, H. M., Read, W. G., Siegel, P. H., Cofield, R. E., Filipiak, M. J., Flower, D. A., et al.: The earth observing system microwave limb sounder (EOS MLS) on the Aura satellite, 2006.

Waugh, D. and Hall, T.: Age of stratospheric air: Theory, observations, and models, Reviews of Geophysics, 40, 1–1, 2002.

Wauthy, B.: Physical ocean environment in the South Pacific Commission Area. Prepared in co-operation with SPC, SPEC, ESCAP., UNEP Regional Seas Reports and Studies (UNEP). no. 83., 1986.

Wayne, R. P.: Chemistry of atmospheres, Chemistry of atmospheres, by Wayne, RP. Clarendon Press, Oxford (UK), 2000, 460 p., ISBN 0-19-855571-7,, 2000.

Weatherhead, E. C., Reinsel, G. C., Tiao, G. C., Meng, X.-L., Choi, D., Cheang, W.-K., Keller, T., DeLuisi, J., Wuebbles, D. J., Kerr, J. B., et al.: Factors affecting the detection of trends: Statistical considerations and applications to environmental data, Journal of Geophysical Research: Atmospheres, 103, 17 149–17 161, 1998.

Weber, M., Dikty, S., Burrows, J. P., Garny, H., Dameris, M., Kubin, A., Abalichin, J., and Langematz, U.: The Brewer-Dobson circulation and total ozone from seasonal to decadal time scales, Atmospheric Chemistry and Physics, 11, 11 221–11 235, https://doi.org/10.5194/acp-11-11221-2011, URL https://www.atmos-chem-phys.net/11/11221/2011/, 2011.

Weber, M., Pagaran, J., Dikty, S., von Savigny, C., Burrows, J. P., DeLand, M., Floyd, L. E., Harder, J. W., Mlynczak, M. G., and Schmidt, H.: Investigation of Solar Irradiance Variations and Their Impact on Middle Atmospheric Ozone, pp. 39–54, Springer Netherlands, Dordrecht, https://doi.org/10.1007/978-94-007-4348-9_3, URL https://doi.org/10.1007/978-94-007-4348-9_3, 2013.

Wetzel, G., Bracher, A., Funke, B., Goutail, F., Hendrick, F., Lambert, J.-C., Mikuteit, S., Piccolo, C., Pirre, M., Bazureau, A., Belotti, C., Blumenstock, T., De Mazière, M., Fischer, H., Huret, N., Ionov, D., López-Puertas, M., Maucher, G., Oelhaf, H., Pommereau, J.-P., Ruhnke, R., Sinnhuber, M., Stiller, G., Van Roozendael, M., and Zhang, G.: Validation of MIPAS-ENVISAT NO_2 operational data, 7, 3261–3284, 2007.

Wetzel, G., Oelhaf, H., Höpfner, M., Friedl-Vallon, F., Ebersoldt, A., Gulde, T., Kazarski, S., Kirner, O., Kleinert, A., Maucher, G., et al.: Diurnal variations of BrONO 2 observed by MIPAS-B at midlatitudes and in the Arctic, Atmospheric Chemistry and Physics, 17, 14 631–14 643, 2017.

Wieters, N.: Investigation of the impact of extraterrestrial energetic particles on stratospheric nitrogen compounds and ozone on the basis of three dimensional model studies, 2013.

WMO: Scientific Assessment of Ozone Depletion: 2014, Global Ozone Research and Monitoring Project-Report No. 55, WMO (World Meteorological Organization), Geneva, Switzerland, URL https://www.esrl.noaa.gov/csd/assessments/ozone/, 2014.

Ziemke, J., Chandra, S., Duncan, B., Froidevaux, L., Bhartia, P., Levelt, P., and Waters, J.: Tropospheric ozone determined from Aura OMI and MLS: Evaluation of measurements and comparison with the Global Modeling Initiative's Chemical Transport Model, Journal of Geophysical Research: Atmospheres, 111, 2006.